Search for The Double Beta Decay Modes of ^{134}Xe with the First Year of Phase II Data from EXO-200 and Development of Laser-Driven *In-Situ* Electron Lifetime Monitoring for nEXO

A Dissertation presented

by

Oumarou Mbombo Njoya

to

The Graduate School

in Partial Fulfillment of the

Requirements

for the Degree of

Doctor of Philosophy

in

Physics

Stony Brook University

August 2018

Stony Brook University

The Graduate School

Oumarou Mbombo Njoya

We, the dissertation committee for the above candidate for the

Doctor of Philosophy degree, hereby recommend

acceptance of this dissertation

Krishna S. Kumar - Dissertation Advisor
Professor, Department of Physics and Astronomy, Stony Brook University

George Sterman - Chairperson of Defense
Distinguished Professor, Department of Physics and Astronomy, Stony Brook University

Joanna Kiryluk - Committee Member
Associate Professor, Department of Physics and Astronomy, Stony Brook University

Aleksey Bolotnikov - External Committee Member
Scientist, Nonproliferation and National Security Department, Brookhaven National Laboratory

This dissertation is accepted by the Graduate School

Charles Taber
Dean of the Graduate School

Abstract of the Dissertation

Search for The Double Beta Decay Modes of ^{134}Xe with the First Year of Phase II Data from EXO-200 and Development of Laser-Driven *In-Situ* Electron Lifetime Monitoring for nEXO

by

Oumarou Mbombo Njoya

Doctor of Philosophy

in

Physics

Stony Brook University

2018

This thesis presents a search for double beta $(0\nu\beta\beta)$ decay of ^{134}Xe using the Enriched Xenon Observatory (EXO-200). EXO-200 is a 200-kg single phase liquid xenon (LXe) time projection chamber (TPC) built to search for $0\nu\beta\beta$ process in ^{136}Xe; however 19.1% of its mass is ^{134}Xe. Using the first year of the Phase II dataset we get an exposure 13.4 kg·yr and derive lower limits of $T_{1/2}^{2\nu\beta\beta} > 3.22 \times 10^{21}$ yr and $T_{1/2}^{0\nu\beta\beta} > 4.9 \times 10^{23}$ yr at 90% confidence level. The half-life sensitivity for $2\nu\beta\beta$ is 5.3×10^{21}.

Building on the success of EXO-200, nEXO, a 5-tonne next generation detector, has been proposed and various aspects of R&D are currently underway. Due to its size (1.3 m × 1.3 m) standard external calibration techniques will not be sufficient for nEXO. The second part of this thesis focuses on the development of a laser-driven *in-situ* electron lifetime monitoring system for nEXO. We designed and built a small Xe TPC system. Electrons generated by driving a gold photocathode with a 71-ns, 262-nm UV pulse were released into a 20 mm LXe column and drifted in a uniform electric field. We measured the charge carriers' transport properties including drift speed, diffusion, and lifetime. We were also able to disentangle gold photo-electricity from multi-photon LXe ionization and this allowed us to infer the two-photon absorption cross section of xenon atoms.

To my family.

Contents

List of Figures

List of Tables

List of Abbreviations

EXO-200	Enriched Xenon Observatory
nEXO	Next Enriched Xenon Observatory
TPC	Time Projection Chamber
MPI	Multi Photon Ionization
WIPP	Waste Isolation Pilot Plant
LXe	Liquid Xenon
GXe	Gas Xenon
PDF	Probability Distribution Function
eV	Electron Volt
kg	kilo-gram
keV	kilo-electron volt
MeV	mega-electron volt
kW/cm^2	kilo-Watt per cm^2

List of Symbols

$2\nu\beta\beta$	Two-neutrino double beta decay
$0\nu\beta\beta$	Neutrinoless double beta decay
Q	Q-value
A	Mass number
Z	Atomic number

e	Elementary charge
$\hbar$	Reduced Planck's constant

Publications

Acknowledgements

I want to first acknowledge and thank my parents Angeline and Moussa Njoya for their unwavering support throughout the years. Uprooting your family and moving to a new country and language in your late 40s with five teenage children was no small sacrifice. I may never be able to repay you for the opportunities your sacrifices have afforded me but I hope this accomplishment brings you a little joy and pride. Your love and undying belief fuel me.

My adviser, Krishna Kumar gave me a second chance in graduate school and for this I am eternally grateful. You allowed me to wander intellectually, often going places that made no sense. You made available to me all the resources I needed and you were incredibly patient and understanding when I fell behind on deadlines. I have learned a tremendous amount of physics from you as well as general life skills. Thank you, KK.

Graduate study is a long and arduous process, often lonely, and always challenging. However it is made bearable by one's love for the research topic and the companions one encounters along the way. I thank my dear friends Arthur Zhao and Karen Chen who have stuck with me from the beginning. Your friendships have kept me grounded throughout the good and not so good times. Thank you for all the trips, the late night discussions, the good food, and the bad jokes. I also acknowledge Ahsan Ashraf, Melissa Louie, Harikrishnan Ramani, and Spencer Horton.

To my brothers and sisters (Zenabou, Soule, Mohammed, Bijoux, Ami, Amadou et Jean-Paul), now spread across three continents, I express my love and gratitude for your quiet and resilient support throughout my entire life. As you have all married and started families of you own we have somewhat grown apart but the bonds we forged in childhood remain strong and I have drawn inspiration from every single one of you. I will make more time to visit you all in the future.

No work in the 21st century is possible without Google, Wikipedia, and for us physicists the arxiv. These are tremendous resources I leaned on on a daily basis and I would be remiss if I did not mention them here. I should also mention the Stony Brook Physics machine shop, the Brookhaven National Lab's Instrumentation Division machine shop, the EXO-200 team at WIPP, Michal Tarka, John Walsh, and Bill Smith, all of whom have been tremendous resources.

Last but not least I want to acknowledge and thank my EXO-200 and nEXO collaborators, especially Thomas Tsnag, Bill Fairbank, Dave Moore, Caio Licciardi, Al Odian, and Triveni Rao for always asking the right questions and guiding me toward the answers. The work in this thesis would not have been possible without your help and support.

Chapter 1

Introduction

From the time its existence was first hypothesized by Wolfgang Pauli [1], the neutrino has been one of the more elusive fundamental particles. After its discovery in 1956, the neutrino was introduced into the standard model as a massless spin-1/2 lepton. In the following decades neutrino experiments demonstrated that neutrinos oscillate between their flavor eigenstates thus violating lepton flavor conservation. These flavor oscillations were only possible if each flavor was a superposition of mass eigenstates with unequal masses. From this it followed that neutrinos must be massive. However these oscillation experiments are only sensitive to the difference in squared masses and not to the absolute masses themselves; thus was born the mass hierarchy problem.

There are three approaches to the measurement of the absolute neutrino mass. First is cosmology, which has placed the most stringent limit to date based on measurements of anisotropies in the primordial cosmic microwave background [2, 3]. However these results are strongly model-dependent. The second and more direct approach involves time of flight measurements of neutrinos emitted from supernovae and the study of the kinematics of weak decays [4, 5]. The third approach is to search for neutrinoless double beta decay.

Neutrinoless double beta ($0\nu\beta\beta$) decay exists only if the neutrino is a Majorana particle, that is, its own antiparticle, and has a non-zero mass. Numerous model extensions of the standard model (SM) generate Majorana neutrinos by breaking lepton number (LN) conservation [6, 7].

The search for physics beyond the SM is a rich and vibrant activity in the low energy nuclear and high energy physics communities. In a $0\nu\beta\beta$ decay process, two bound neutrons simultaneously decay into two bound protons and two leptons as described by $(Z, A) \rightarrow (Z + 2, A)$ + $2e^-$. The observation of $0\nu\beta\beta$ decay could also provide some insight on the neutrino mass hierarchy. To observe this process single beta decay must be forbidden or heavily suppressed. Consequently, only 35 potential double beta emitters exist [8]. Lower limits of half-lives greater than $\sim 10^{25}$ years for $0\nu\beta\beta$ decay have been measured for ^{136}Xe and ^{76}Ge isotopes. The two-neutrino accompanied double beta ($2\nu\beta\beta$) decay is an allowed process in the SM and is the rarest decay ever measured in nature [7, 9, 10].

There are many large experiments searching for $0\nu\beta\beta$ decay. *The Enriched Xenon Observatory* or EXO-200 is an ongoing experiment searching for the neutrinoless double beta decay of ^{136}Xe. The two-neutrino double beta decay of ^{136}Xe was first measured in 2012 by EXO-200 and is currently the most precise measured half-life of any $2\nu\beta\beta$ decay [11]; it is also the slowest process ever observed directly. Furthermore EXO-200 pushed the limit for the half-life of $0\nu\beta\beta$ in ^{136}Xe to $\mathrm{T}^{0\nu}_{1/2}$ ¿ 1.8×10^{25} yr at 90% confidence level (CL) [12]. In addition to ^{136}Xe, 19.1% of EXO-200's mass is the isotope ^{134}Xe for which limits of $\mathrm{T}^{2\nu\beta\beta}_{1/2} > 8.7 \times 10^{20}$ yr and $\mathrm{T}^{0\nu\beta\beta}_{1/2} > 1.1 \times 10^{23}$ yr were derived using the first 3 years of data (Phase I, exposure of 29.6 kg·yr) [13]. Both of these limits are the most stringent, exceeding those previously in the literature for ^{134}Xe by factors of nearly 10^5 and 2 for the two-neutrino and neutrinoless modes respectively.

nEXO is a planned 5-tonne isotopically enriched LXeTPC with a target half-life sensitivity of $\approx 10^{27}$ years [14, 15]. It thus aims at probing the inverted hierarchy down to a few tenths of meV. With a better handle on backgrounds and an improved energy resolution nEXO builds on the success of and optimizes lessons learned from EXO-200. To this end an aggressive R&D program is underway.

Calibration is an essential element of a successful nEXO and as such constitutes a significant part of the R&D effort. Among liquid noble elements LXe has the highest stopping power for penetrating radiation, mainly as a result of its high atomic number (54) and density (3g/cm^3).

This makes a large detector like nEXO nearly impenetrable as the attenuation length for 2.5 MeV gammas (^{136}Xe $0\nu\beta\beta$ Q-value = 2.458 MeV) in LXe is only $\sim$8.5 cm. Therefore, conventional external calibration sources are expected to be insufficient and new techniques need to be explored. A distinctive attribute of liquid rare elements is the production of ionization electrons and scintillation photons in response to radiation [16]. This is especially significant in LAr and LXe. nEXO would like to incorporate a laser system in its design, which would be used for calibration purposes. The focus of the SBU/BNL group is on **in-situ** charge calibration, namely we produce charge "clusters" from laser-driven photocathodes in order to measure electron transport properties in LXe. The ultimate goal is to develop a robust technique for charge calibration and monitoring electron lifetime in nEXO. This is paramount since in order to achieve the 1% energy resolution goal the electron lifetime needs to be at least $\sim$10 ms and most importantly its exact value must be continuously monitored.

This thesis has two thrusts: first a search for both double beta decay modes of ^{134}Xe using the Phase II dataset from EXO-200 and second the development of an *in-situ* electron lifetime monitoring system as a calibration tool for nEXO. We will start with a brief introduction of neutrino physics in Chapter 2. Chapter 3 will describe the EXO-200 detector. In Chapter 4 we present the analysis and results of our searches for $0\nu\beta\beta$ and $2\nu\beta\beta$ decay modes of ^{134}Xe. In Chapter 5 we'll describe in more details the nEXO concept. Chapter 6 will outline our design, construction, and operation of a small TPC at SBU and BNL along with measurements we performed. We conclude the thesis and offer an outlook for future work in Chapter 7.

Chapter 2

Neutrino Physics

2.1 A Brief History

In 1896, one year before J.J. Thompson discovered the electron, Henri Becquerel stumbled on 'spontaneous radioactivity,' the process by which some chemical elements, even in the absence of external stimuli such as light or electricity, would emit radiation capable of leaving a mark on a photographic plate [6]. Later analysis of this spontaneous radioactivity revealed that different elements emitted different types of radiation which Ernest Rutherford named α, β, and γ rays. These rays were also found to possess different properties: α-rays were easy to absorb and bent slightly in the presence of a magnetic field. β-rays were harder to absorb than α-rays and bent significantly in the presence of a magnetic field. γ-rays were very hard to absorb and did not bend in the presence of a magnetic field.

The story of the neutrino begins with detailed studies of β radiation in the first third of the 20th century. Early experiments suggested that, like the spectrum of α decay, nuclear β decay spectra were discrete. However Chadwick presented in 1914 irrefutable evidence for a continuous β-ray spectrum. Since the nucleus was thought to be made of both protons and electrons (nucleus = $n_p p + n_e e^-$), this was a problem as it seemed to violate energy-momentum conversation ($N \rightarrow N' + e^-$ – electron energy and momentum well defined) [6]. Furthermore this nuclear model also seemed to violate the spin-statistics theorem in certain cases. For example $^{14}N = 14p + 7e^-$ was expected to be a fermion but it was experimentally known that it was indeed a boson [6].

In 1930 Wolfgang Pauli came to the rescue by postulating the existence of an electrically neutral particle in the nucleus, which in a β decay process, "is emitted along with the electron in such a way that the sum of the energies of the neutron and the electron is constant" [6]. Pauli's neutron was later renamed the neutrino by Fermi to distinguish it from the real nuclear neutron discovered by Chadwick in 1932. In 1934 Enrico Fermni wrote his theory of weak interaction [17] in which he suggested β-decay was mediated by the process $n \rightarrow p\, e^-\, \bar{\nu}_e$ and described by the four-fermion interaction:

$$\frac{G_F}{\sqrt{2}}(\bar{n}\Gamma_N p)(\bar{\nu_e}\Gamma_L e) + H.C. \tag{2.1}$$

where G_F is the Fermi constant (strength of interaction) and $\Gamma_{N,L}$ are linear combinations of gamma matrices. Understanding β-decay in this formalism also led to an improved and correct picture of the nucleus. Furthermore Fermi's theory made it possible to understand other physical processes such as

$$\bar{\nu_e} + p \rightarrow e^+ + n \tag{2.2}$$

which proved instrumental in the discovery/observation of the neutrino 22 years later [18].

Definitive evidence for the existence of the neutrino was obtained in 1956 by Cowan and Reynes at the Savannah nuclear reactor site by looking at scattering events from equation 2.2 [18]. The daughter positron annihilates with a nearby electron and the resulting photon energy is detected in a scintillating environment. Following this the recoil neutron is absorbed in the detector/scintillator (after a well defined mean free time) and emits γs at a well defined energy. Cowan and Reynes measured these two signals in delayed coincidence.

The following 50 years saw slow yet exciting progress in our understanding of neutrinos. In 1958 Goldhaber et al. measured the helicity of the neutrino, confirming neutrinos are purely left-handed and only interact via the weak force, i.e. they violate parity maximally [19]. Using the first neutrino beam, Lederman, Steinberger, and Schwartz confirmed the existence of a second neutrino flavor $\nu_\mu \neq \nu_e$ in 1962 at Brookhaven National Laboratory [20]. In the 1970s the τ-lepton was discovered [21, 22] and in 2001 its corresponding neutrino the ν_τ was directly observed by the DONUT experiment at Fermi National Accelerator Laboratory [23].

A handful of neutrino puzzles also emerged during the last third of the 20th century. Numerous experiments independently observed a discrepancy between the measured solar (mostly electron) neutrino flux and that predicted by the standard solar model, a well tested and accepted theory [24, 25]. A similar discrepancy was observed for the atmospheric (mostly muon) neutrino fluxes. A definitive resolution to these issues came less than 20 years ago when it was shown neutrinos change flavor after propagating a finite distance [26, 27]. The rate of change depends on the neutrino energy E_ν and the baseline L. We discuss this phenomenon in detail in the next section.

The corollary to neutrino oscillations was that neutrinos must have mass [6, 25]. This has tremendous consequences leading to the present moment. The Standard Model neutrinos are left-handed massless neutral fermions that can only be described by 2 degrees of freedom. A massive neutral fermion in the other hand can be described by 4 degrees of freedom (Dirac case) or by 2 degrees of freedom (Majorana case). To date it is unclear which category massive neutrinos fall into. Whatever the case this hints to new physics beyond the standard model (BSM) of electroweak interactions.

2.2 Neutrino Oscillations

Neutrino oscillation is the process in which neutrinos produced in an initial flavor eigenstate α change into flavor eigenstate β after propagating a finite distance L (known as the baseline). This can arise out of several different mechanisms. However the simplest one is to recognize that once neutrinos have mass, leptons can mix [6]. Let ν_1, ν_2, ν_3 be neutrinos with well defined masses m_1, m_2, m_3. The neutrino flavor eigenstates (ν_e, ν_μ, ν_τ) are related to the neutrino mass eigenstates via the relation:

$$|\nu_\alpha\rangle = \sum_{i=1}^{3} U_{\alpha i} |\nu_i\rangle \tag{2.3}$$

Here $U_{\alpha i}$ is the unitary Pontecorvo-Maki-Nakagawa-Sakata (PMNS) matrix which describes the mixing among flavor and mass eigenstates [28]. U is given by:

$$\begin{bmatrix} \nu_e \\ \nu_\mu \\ \nu_\tau \end{bmatrix} = \begin{bmatrix} U_{e1} & U_{e2} & U_{e3} \\ U_{\mu 1} & U_{\mu 2} & U_{\mu 3} \\ U_{\tau 1} & U_{\tau 2} & U_{\tau 3} \end{bmatrix} \begin{bmatrix} \nu_1 \\ \nu_2 \\ \nu_3 \end{bmatrix} \tag{2.4}$$

We can parametrize U and after factoring we get:

$$U = \begin{bmatrix} 1 & 0 & 0 \\ 0 & c_{23} & s_{23} \\ 0 & -s_{23} & c_{23} \end{bmatrix} \begin{bmatrix} c_{13} & 0 & s_{13}e^{-i\delta_{CP}} \\ 0 & 1 & 0 \\ -s_{13}e^{i\delta_{CP}} & 0 & c_{13} \end{bmatrix} \begin{bmatrix} c_{12} & s_{12} & 0 \\ -s_{12} & c_{12} & 0 \\ 0 & 0 & 1 \end{bmatrix} \begin{bmatrix} 1 & 0 & 0 \\ 0 & e^{i\alpha} & 0 \\ 0 & 0 & e^{i\beta} \end{bmatrix} \tag{2.5}$$

where $c_{ij} = \cos\theta_{ij}$, $s_{ij} = \sin\theta_{ij}$, θ_{ij} is the mixing angle between i and j mass eigenstates, δ_{CP} is an unknown charge-parity (CP) violating phase ($0 \leq \delta_{CP} \leq 2\pi$), and α, β are unknown Majorana CP violating phases (included only if neutrinos are Majorana).

Assuming the neutrino propagates as a plane-wave with initial time $t = 0$, position $\vec{x} = \vec{0}$, and momentum $\vec{p}$, the time evolution of the the mass eigenstate $|\nu_i\rangle$ is given by (the time dependent Schrödinger equation)

$$|\nu_i(x,t)\rangle = e^{-i(E_i t - \vec{p}\vec{x})} |\nu_i(0,0)\rangle \tag{2.6}$$

where E_i is the well defined energy of the mass eigenstate. Assuming neutrinos are ultra-relativistic ($p >> m_i$) and travel along the z-direction, the phase factor becomes $E_i t - \vec{p_i}\vec{x} \simeq (E_i t - p_{z,i})L$. (We made use of the fact that $l \simeq |\vec{x}| = ct$, where c is the speed of light). However

$$E_i - p_{z,i} = \frac{E_i^2 - \vec{p}^2}{E_i + p_{z,i}} \simeq \frac{m_i^2}{2E_i} \simeq \frac{m_i^2}{2E} \tag{2.7}$$

where $E_i \simeq E$, and $E_i \simeq |\vec{p}|$. From these we can calculate the probability P that a neutrino with flavor α a $t = 0$ will transition to flavor β after propagating some distance L. P is given by the transition probability [25]

$$P(\nu_\alpha \rightarrow \nu_\beta) = |\, \langle \nu_\beta| \, |\nu_\alpha(L,t)\rangle \,|^2 \tag{2.8}$$

$$\begin{aligned} P(\nu_\alpha \rightarrow \nu_\beta) = \delta_{\alpha\beta} &- 4 \sum_{i>j=1}^{3} Re(U_{\alpha i} U^*_{\beta i} U^*_{\alpha j} U_{\beta j}) \sin^2(\frac{\Delta m^2_{ij} L}{4E}) \\ &+ 2 \sum_{i>j=1}^{3} Im(U_{\alpha i} U^*_{\beta i} U^*_{\alpha j} U_{\beta j}) \sin^2(\frac{\Delta m^2_{ij} L}{4E}) \end{aligned} \tag{2.9}$$

where $\Delta m^2_{ij} = m^2_i - m^2_j$ is the squared mass difference. In 2.9 the explicit time dependence is removed and one can see that the transition/oscillation probability – which is what neutrino oscillation experiments measure – depends only on $\frac{L}{E}$ and on Δm^2_{ij}. At least two masses must be different for oscillations to occur. The imaginary part of the PMNS matrix vanishes (i.e. $Im(U_{\alpha i} U^*_{\beta i} U^*_{\alpha j} U_{\beta j}) = 0$ if there is no CP violation in the neutrino sector. On the other hand if all three masses are different, the phase δ could lead to an observable CP violation [29, 24]. Neutrino oscillation experiments look for the appearance of a new flavor or the disappearance of an expected flavor of neutrinos by placing a detector in the path of a source known to produce a specific flavor of neutrinos.

For three flavors of neutrinos there are only two independent squared mass splittings, Δm^2_{12} and Δm^2_{13}. Global analyses of all oscillation experiment data show that Δm^2_{12} and Δm^2_{13} are both non-zero [30]. By convention Δm^2_{12} is chosen to be the smallest of the mass splittings. Furthermore m_1 and m_2 are arbitrarily defined such that $m_1 < m_2$. Δm^2_{12} is typically labeled Δm^2_{sol} because it is measured from solar neutrino oscillations while Δm^2_{13} is labeled $\Delta \mathrm{m}^2_{atm}$ because it is measured from atmospheric neutrino oscillations. It is not possible to determine the sign of $\Delta \mathrm{m}^2_{atm}$ based on current atmospheric oscillation data; consequently there are two possible orderings of the mass eigenstates (see figure 2.1):

$$m_1 < m_2 < m_3 \qquad ''Normal\ Hierarchy'' \tag{2.10}$$

$$m_3 < m_1 < m_2 \qquad \text{"}Inverted\ Hierarchy\text{"} \tag{2.11}$$

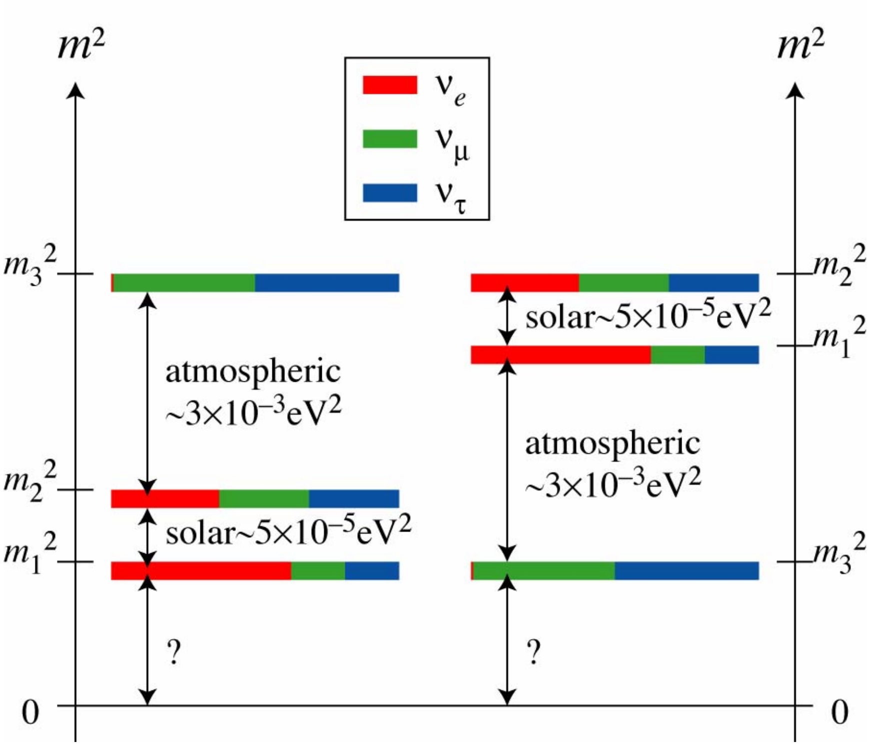

Figure 2.1: Neutrino mass hierarchy.

The normal hierarchy gets its name from the fact that the mass eigenstates are ordered numerically while the inverted hierarchy has m_3 as the lightest mass eigenstate. It should also be emphasized that oscillation experiments cannot measure the absolute neutrino mass scale (i.e. offset from 0) as is illustrated in figure 2.1; this is also evident from the fact that the oscillation probability is independent of the two Majorana phases $\alpha_{1,2}$ and the absolute mass of the neutrino.

2.3 Origin of the Neutrino Mass

In the Standard Model formalism neutrinos are expected to be massless. However the neutrino oscillation experiments have demonstrated neutrinos must have mass. This discovery has opened the field of neutrino physics and many interesting questions have arisen:

1. Are neutrinos Majorana particles? In the SM spin-1/2 fermions are Dirac and neutral fermions are massless. Up until 25 years ago, neutrinos were thought to satisfy both conditions. However if they have mass they may in fact be Majorana.
2. How do neutrinos acquire mass? The existence of Majorana masses hints to BSM physics. One example is lepton number violation (LNV) [31].
3. Why is there more matter than anti-matter? New mass generation mechanism for the neutrino and lepton number violation would seem to support leptogenesis, a theory that attempts to explain the observed baryon asymmetry in the universe.

There are many indications that understanding the mechanism of neutrino mass could help answer many of these questions. In this section I will give a detailed description of the prevailing theory.

2.3.1 Dirac vs Majorana fermions

In quantum field theory the equation of motion (EOM) for a field can be found by solving the Euler-Lagrange equation:

$$\frac{\partial L}{\partial(\partial_\mu \phi)} = \frac{\partial L}{\partial \phi} \tag{2.12}$$

where L is the Lagrangian and ϕ is a field. The Lagrangian for a free spin-1/2 fermion is

$$L = \bar{\phi}(i\gamma^\mu \partial_\mu - m)\psi. \tag{2.13}$$

Equation 2.12 for the field $\bar{\psi}$ gives

$$\frac{\partial L}{\partial(\partial_\mu \bar{\psi})} = 0 \tag{2.14}$$

and

$$\frac{\partial L}{\partial_\mu \bar{\psi}} = (i\gamma^\mu \partial_\mu - m)\psi \tag{2.15}$$

so, the EOM for a spin-1/2 fermion is

$$(i\gamma^{\mu}\partial_{\mu} - m)\psi = 0 \tag{2.16}$$

which is just the Dirac equation. Equation 2.13 shows us that the mass is included in the standard model through the Dirac mass term $m\bar{\psi}\psi$. We can decompose the Dirac spinor into its left- and right-chiral states.

$$m\bar{\psi}\psi = m(\overline{\psi_L + \psi_R})(\psi_L + \psi_R) = m\bar{\psi}_L\psi_R + m\bar{\psi}_R\psi_L \tag{2.17}$$

where we've used the fact that $\bar{\psi}_L\psi_L = \bar{\psi}_R\psi_R = 0$. The important point to note is that a non-zero Dirac mass requires a particle to have both a left- and right-handed chiral state: in fact the Dirac mass can be viewed as being the coupling constant between the two chiral components.

Since we know the neutrino is chirally left-handed (neutrino discovery experiments), there is good reason to suppose that the neutrino must be massless, as there does not seem to be a right-handed state for the mass term to couple to. We also know that the neutrino has a small mass (oscillation experiments), so either there must be a right-handed (sterile) neutrino which only shows up in the standard model to give the neutrino mass, but otherwise cannot be observed as the weak interaction doesn't couple to it, or there is some other sort of mass term out there.

One consequence of Majorana's symmetrical theory of electrons and anti-electrons is that there need not be a right handed sterile neutrino; in other words it is possible to construct a mass term using only the left-handed chiral state [32]. Let us split the Dirac Lagrangian into its chiral components

$$
\begin{aligned}
L &= \bar{\psi}(i\gamma^{\mu}\partial_{\mu} - m)\psi \\
&= (\bar{\psi}_L + \bar{\psi}_R)(i\gamma^{\mu}\partial_{\mu} - m)(\psi_L + \psi_R) \\
&= \bar{\psi}_L i\gamma^{\mu}\partial_{\mu}\psi_L - m\bar{\psi}_L\psi_L + \bar{\psi}_L i\gamma^{\mu}\partial_{\mu}\psi_R - m\bar{\psi}_L\psi_R + \\
&\quad \bar{\psi}_R i\gamma^{\mu}\partial_{\mu}\psi_L - m\bar{\psi}_R\psi_L + \bar{\psi}_R i\gamma^{\mu}\partial_{\mu}\psi_R - m\bar{\psi}_R\psi_R \\
&= \bar{\psi}_R i\gamma^{\mu}\partial_{\mu}\psi_R + \bar{\psi}_L i\gamma^{\mu}\partial_{\mu}\psi_L - m\bar{\psi}_R\psi_L - m\bar{\psi}_L\psi_R \\
&= \bar{\psi}_R(i\gamma^{\mu}\partial_{\mu}\psi_R - m\bar{\psi}_L) + \bar{\psi}_L(i\gamma^{\mu}\partial_{\mu}\psi_L - m\bar{\psi}_R)
\end{aligned}
\tag{2.18}
$$

where we've used a number of identities to kill off a few terms:

$$
\begin{aligned}
\bar{\psi}_R\gamma^{\mu}\partial_{\mu}\psi_L = \bar{\psi}P_L\gamma^{\mu}\partial_{\mu}P_L\psi = \bar{\psi}\gamma^{\mu}\partial_{\mu}P_RP_L\psi &= 0 \\
\bar{\psi}_L\gamma^{\mu}\partial_{\mu}\psi_R &= 0 \\
m\bar{\psi}_R\psi_R &= 0 \\
m\bar{\psi}_L\psi_L &= 0
\end{aligned}
\tag{2.19}
$$

Using the Euler-Lagrange 2.12 we find two independent EOM for ψ_L and ψ_R:

$$i\gamma^{\mu}\partial_{\mu}\psi_L = m\psi_R \tag{2.20a}$$

$$i\gamma^{\mu}\partial_{\mu}\psi_R = m\psi_L \tag{2.20b}$$

They are Dirac equations coupled by the mass term. If the field were massless then we would have the Weyl equation

$$(i\gamma^{\mu}\partial_{\mu})\psi_L = 0 \tag{2.21a}$$

$$(i\gamma^{\mu}\partial_{\mu})\psi_R = 0 \tag{2.21b}$$

The neutrino is now described using only two independent two-component spinors which also turn out to be helicity eigenstates and describe two states with definite and opposite helicity. These correspond to the left-handed neutrino ν_L and the right-handed neutrino ν_R. Since ν_R does not exist in the SM, then we just describe the neutrino with a single massless left-handed field and that is the usual formulation of the Standard Model.

In order to describe a massive neutrino using just a single left-handed field we need to make equation 2.20b look like 2.20a by expressing ψ_R in terms of ψ_L. To start we take the hermitian conjugate of equation 2.20b and get

$$\begin{aligned} (i\gamma^\mu \partial_\mu \psi_R)^\dagger &= m\psi_L^\dagger \\ -i\partial_\mu \psi_R^\dagger \gamma^{\mu\dagger} &= m\psi_L^\dagger \end{aligned} \tag{2.22}$$

Multiplying on the right by γ^0 and remembering that $\gamma^0\gamma^{\mu\dagger}\gamma^0 = \gamma_\mu$ and $(\gamma^0)^2 = 1$, we have

$$-i\partial_\mu \psi_R^\dagger \gamma^0 \gamma^{\mu\dagger} = m\psi_L^\dagger \gamma^0 \tag{2.23}$$

and therefore,

$$-i\partial_\mu \bar{\psi}_R \gamma^\mu = m\bar{\psi}_L \tag{2.24}$$

We can rearrange things by taking the transpose

$$\begin{aligned} [-i\partial_\mu \bar{\psi}_R \gamma^\mu]^T &= m\bar{\psi}_L^T \\ -i\gamma^{\mu T} \partial_\mu \bar{\psi}_R^T &= m\bar{\psi}_L^T \end{aligned} \tag{2.25}$$

and using the identity $C\gamma^{\mu T} = -\gamma^\mu C$ where *C* is the charge conjugation operator we get

$$i\gamma^\mu \partial_\mu C\bar{\psi}_R^T = mC\bar{\psi}_L^T \tag{2.26}$$

Equation 2.26 looks a lot like equation 2.20a if we set

$$\psi_R = C\bar{\psi}_L^T \tag{2.27}$$

To be clear we are essentially requiring that $C\bar{\psi}_L^T$ be right-handed. If this is true then applying the left-handed chiral projection operator $P_L = \frac{1}{2}(1-\gamma^5)$ to equation 2.26 should give 0. Hence

$$P_L\psi_R = P_L(C\bar{\psi}_L^T) = CP_L^T\bar{\psi}_L^T = C(\bar{\psi}_L P_L)^T. \tag{2.28}$$

which is indeed 0 since

$$\begin{aligned}\bar{\psi}_L P_L &= (P_L\psi)^\dagger\gamma_0 P_L \\ &= \psi^\dagger P_L\gamma_0 P_L \\ &= \psi^\dagger\gamma^0 P_R P_L \\ &= 0\end{aligned} \tag{2.29}$$

The Majorana field then becomes

$$\psi = \psi_L + \psi_R = \psi_L + C\bar{\psi}_L^T = \psi_L + \psi_L^C \tag{2.30}$$

where $\psi_L^C \equiv C\bar{\psi}_L^T$ is the charge-conjugate field. Finally if we take the charge conjugate of the Majorana field we get:

$$\psi^C = (\psi_L + \psi_L^C)^C = \psi_L^C + \psi_L = \psi \tag{2.31}$$

That is, the charge conjugate of the field is the same as the field itself, or as more conventionally stated, the Majorana particle is its own anti-particle. Clearly, for a particle to be Majorana it must be neutral as the charge conjugation flips the sign of the electric charge. Therefore, no charged fermion can be identical to its antiparticle. The only candidate is indeed the neutrino.

A Majorana mass term for the Lagrangian will then only contain a left-handed field. A reasonable guess, inspired from $L^D = -m\bar{\nu}_R\nu_L$ is $L^M = -\frac{1}{2}m\bar{\nu}_L^C\nu_L$. The factor of a half accounts for the double counting since the hermitian conjugate is identical. The Majorana term couples the antineutrino to the neutrino component. Dirac neutrinos have lepton number $L = +1$ and antineutrinos have lepton number $L = -1$. Since Majorana neutrinos are the same as their antiparticle it is impossible to give such an object a conserved lepton number; this is why interactions involving Majorana neutrinos generally violate lepton number conservation by $\Delta L = \pm 2$.

When the Majorana neutrino couples to the weak current it can either produce a negatively charged lepton, if the left-handed component of the Majorana field interacts with a W^+, or a positively charged lepton if the right-handed component interacts with a W^-.

2.3.2 The Seesaw mechanism

The most general mass term one can write down is:

$$L_{mass} = \frac{1}{2}(m_D\bar{\nu}_R\nu_L + m_D\bar{\nu}_L^C\nu_R^C + m_L\bar{\nu}_L^C\nu_L + m_R\bar{\nu}_R^C\nu_R + h.c.) \tag{2.32}$$

which in matrix form becomes

$$L_{mass} \sim \begin{bmatrix} \bar{\nu}_L^C & \bar{\nu}_R \end{bmatrix} \begin{bmatrix} m_L & m_D \\ m_D & m_R \end{bmatrix} \begin{bmatrix} \nu_L \\ \nu_R^C \end{bmatrix} + h.c. \tag{2.33}$$

with the mass matrix

$$M = \begin{bmatrix} m_L & m_D \\ m_D & m_R \end{bmatrix} \tag{2.34}$$

We have expressed the mass Lagrangian in terms of the chiral fields ν_L and ν_R. These fields clearly do not have a definite mass because of the existence of the off-diagonal term, m_D in the mass matrix. That means that these fields are not the mass eigenstates and do not correspond to the physical particle – which must have a definite mass.This just means that the flavor eigenstate which couples to the W and Z bosons is a superposition of the massive neutrino states. As already mentioned in an earlier section a similar thing happens in the quark sector.

Let's call the mass eigenstates ν_1 and ν_2. To find the masses we need to rewrite the Lagrangian in terms of ν_1 and ν_2 which means we must diagonalize the mass matrix, i.e find U such that

$$L_{mass} \sim \begin{bmatrix} \nu_L \\ \nu_R^C \end{bmatrix} = U \begin{bmatrix} \nu_{1,L} \\ \nu_{2,L} \end{bmatrix} \tag{2.35}$$

This implies

$$U^\dagger \begin{bmatrix} m_L & m_D \\ m_D & m_R \end{bmatrix} U = \begin{bmatrix} m_1 & 0 \\ 0 & m_2 \end{bmatrix} \tag{2.36}$$

The only 2x2 unitary matrix is the standard rotation matrix. So,

$$\begin{aligned} \nu_L &= \cos(\theta)\nu_{1,L} - \sin(\theta)\nu_{2,L} \\ (\nu_R)^C &= \sin(\theta)\nu_{1,L} + \cos(\theta)\nu_{2,L} \end{aligned} \tag{2.37}$$

After diagonalizing M we find

$$m_{1,2} = \frac{1}{2}[(m_L + m_R) \pm \sqrt{(m_L - m_R)^2 + 4m_D^2}] \tag{2.38}$$

We can choose different values for m_L, m_R, and m_D and this will give us different physical masses, but the interesting behavior occurs if one chooses $m_L = 0$, $m_R >> m_D$ (a choice motivated by the fact that the SM explicitly forbids the left-handed Majorana term). This choice leads to ν_1 having a mass

$$m_1 = \frac{m_D^2}{m_R} \tag{2.39}$$

and ν_2 having mass m_2

$$m_2 = m_R(1 + \frac{m_D^2}{m_R^2}) \approx m_R \tag{2.40}$$

It is easy to see that if we have a neutrino mass m_2 that is very large , then the mass of the other neutrino m_1 is very small because of the suppression provided by the $\frac{1}{m_R}$. Furthermore the mass eigenstates are given by $\nu_1 \sim (\nu_L + \nu_L^C) - \frac{m_D}{m_R}(\nu_R + \nu_R^C)$ and $\nu_2 \sim (\nu_R + \nu_R^C) + \frac{m_D}{m_R^2}(\nu_L + \nu_L^C)$. That is ν_1 is mostly the (familiar) left-handed light Majorana neutrino and ν_2 is mostly the heavy sterile right-handed neutrino partner. This is the famous see-saw mechanism. It provides an explanation for the question of why the neutrino has a mass so much smaller than the other charged leptons. The charged leptons are Dirac particles and therefore have a Dirac mass on the order of 1 MeV (or so). Suppose the Dirac mass of the neutrino is around the same value ($m_D \approx 1$ MeV) like all the other particles. Then if the mass of the heavy partner is around 10^{15} eV, the mass of the light neutrino will be in the meV range, as we now know it is.

The possibility of the existence of these heavy neutrinos also have given rise to another intriguing idea called leptogenesis which is intrinsically linked to the question of the matter-antimatter a symmetry. The idea is that these very heavy neutrinos, which are Majorana particles, decayed as the universe cooled into lighter left-handed neutrinos or right-handed antineutrinos, along with Higgs bosons, which themselves decayed to quarks. If the probability of one of these heavy neutrinos to decay to a left-handed neutrino was slightly different than the probability to decay to a right-handed anti-neutrino, then there would be a greater probability to create quarks than anti-quarks and the universe would be matter dominated. More formally, it is thought that the quantum number $B - L$, where B is the baryon number of the universe and L is the lepton number, must be conserved. If there was some violation of L in the decays of the heavy Majorana neutrinos, this would manifest as a violation in B, and hence the missing anti-matter problem could actually arise from CP violation in the neutrinos []. Although there is no direct connection between CP violation in the heavy neutrinos and CP violation in the light neutrinos, this idea still motivates the current attempt to measure CP violation in the light neutrinos at today's long baseline neutrino experiments. This argument is one of the reasons why it is important to determine whether the neutrino is a Majorana particle or not.

2.3.3 Neutrino mass measurements

Attempts at measuring the mass of the neutrinos generally involve studying well-known decays of particles which decay to a neutrino and some charged particles. If the momentum of these charged particles can be measured, and the mass of the decaying parent, and the decay products is well known, then energy-momentum conservation can, in principle, allow one to determine the mass of the outgoing neutrino. Since the neutrino mass is so small, experiments of this type are usually extremely difficult. Any systematic error on the order of the neutrino mass could be interpreted as a non-zero neutrino mass, so the experiments must be very well understood.

2.4 Double Beta Decay

Double-beta decay is a rare nuclear process first described by Maria Goeppert-Mayer in 1935 [33]. In the *two-neutrino decay mode* $2\nu\beta\beta$ two neutrons inside a nucleus simultaneously decay into two protons with the emission of two electrons and two anti-neutrinos (see figure 2.2).

$$ {}^{A}_{Z}X \;\rightarrow\; {}^{A}_{Z+2}Y \;+\; 2e^{-} \;+\; 2\bar{\nu}_e \tag{2.41}$$

Here A is the number of nucleons and Z is the number of protons in the parent nucleus X. Double-beta decay is a second order weak process with measured half-lives ranging from 6.9×10^{18} yr (^{100}Mo) to 7.2×10^{24} yr (^{128}Te) [34]. It has been observed in many other isotopes and is the rarest decay ever measured. Allowed in the SM, $2\nu\beta\beta$ can be observed in nuclei for which single beta decay is energetically forbidden or (in the cases of ^{48}Ca and ^{96}Zr) strongly spin-suppressed.

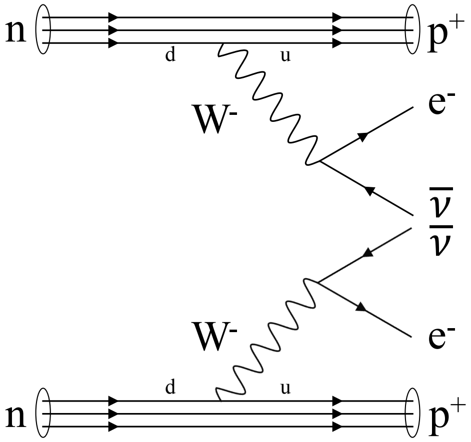

Figure 2.2: Feynman diagram for two neutrino double beta decays.

For even-even nuclei–nuclei with an even number of protons and an even number of neutrons–the nuclear pairing interaction naturally filters these two transitions. The pairing interaction splits the mass parabola in two (see figure 2.3). One parabola for the strongly bound even-even nuclei and one for the less strongly bound odd-odd nuclei. In some cases this leads to the circumstance that a nucleus would be less bound after single beta decay, and so this process is forbidden. This is the case for ^{136}Xe; it is more strongly bound than ^{136}Cs making single beta decay impossible.

On the other hand it is less bound than ^{136}Ba and this makes double-beta decay more energetically favorable.

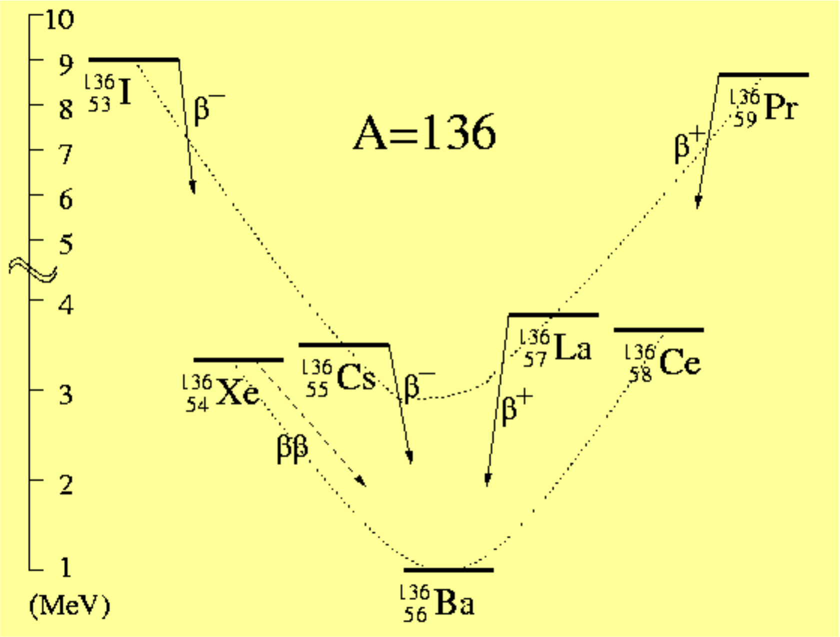

Figure 2.3: Mass parabola. Double beta decay is allowed only if single beta decay is forbidden or heavily suppressed. ^{136}Xe cannot undergo single beta decay into ^{136}Cs. However it can undergo double beta decay to ^{136}Ba.

Another double-beta decay mode is the not-yet-observed *neutrinoless double-beta decay* $0\nu\beta\beta$

$$ {}^{A}_{Z}X \;\rightarrow\; {}^{A}_{Z+2}Y \;+\; 2e^{-} \tag{2.42}$$

In contrast to $2\nu\beta\beta$, $0\nu\beta\beta$ is not allowed in the SM because it violates the total lepton number by $\Delta L = \pm 2$ and can only occur if neutrinos are Majorana particles (see figure 2.4). The decay rate for $0\nu\beta\beta$ is given by

$$\frac{1}{T^{0\nu}_{1/2}} = G^{0\nu} \times |M^{0\nu}|^2 \times \langle m_{\beta\beta}\rangle^2 \tag{2.43}$$

where $T^{0\nu}_{1/2}$ is the half-life, $G^{0\nu}$ the phase space factor, $M^{0\nu}$ the nuclear matrix element, and $\langle m_{\beta\beta}\rangle^2$ the effective Majorana neutrino mass. The phase space factor can be calculated exactly, knowing the energy released in the decay (Q-value).

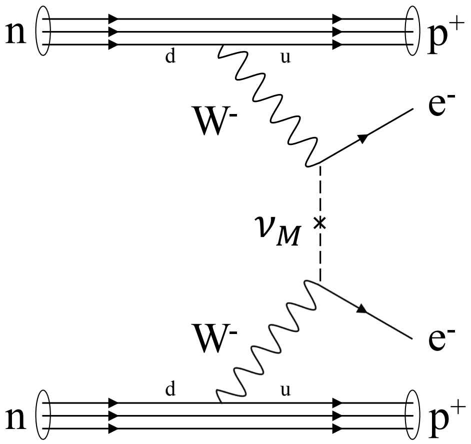

Figure 2.4: Feynman diagram for two neutrino double beta decays

Equation 2.43 assumes that the light neutrino mixing mechanism is the dominant one.Under this assumption the effective Majorana neutrino mass $\langle m_{\beta\beta}\rangle^2$ is

$$m_{\beta\beta} = U_{e1}^2 m_1 + U_{e2}^2 m_2 + U_{e3}^2 m_3 \tag{2.44}$$

where U$_{e}i$ are elements of the PMNS neutrino matrix. From equation 2.43 one can also see that the effective Majorana neutrino mass can be derived from a measurement of $T_{1/2}^{0\nu}$. However one must first calculate the nuclear matrix element (NME) for $0\nu\beta\beta$ decay and this is a complicated many-body problem. Many models (listed in table 2.1 and figure 2.5) have been developed for the NME and while discussing these is beyond the scope of this work, it should be stressed that this is an active area of research in nuclear physics theory. The fact that the nuclear matrix element is model-dependent adds uncertainty to any value of $\langle m_\nu\rangle^2$ derived from experiments.

Method
Quasi particle Random Phase Approximation (QRPA)
Energy Density Functional (EDF)
Projected Hartre-Fock-Bogoliubov approach (PHFB)
Interacting Boson Model-2 (IBM-2)
Large-Scale Shell Model (LSSM)

Table 2.1: Methods of calculation of the NMEs for $0\nu\beta\beta$. Table from [35].

An interesting consequence of the mixing of the mass states in the measurement of $\langle m_\nu\rangle$ is that

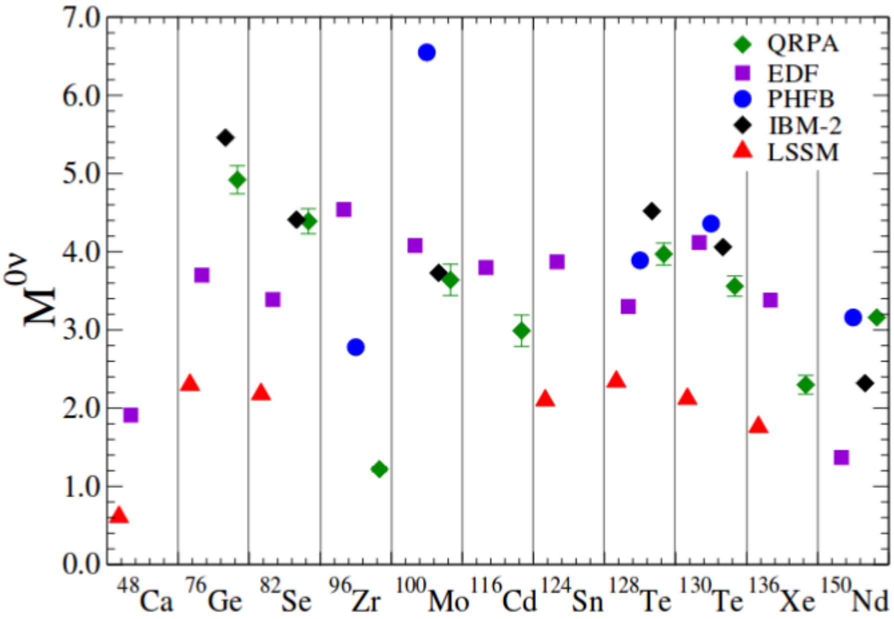

Figure 2.5: Values of NMEs calculated with methods listed in table 2.1. Figure from [35].

neutrinoless double beta decay can also provide information on whether the mass states are in the normal, or inverted hierarchy. Without going into details, one can show that the values of $\langle m_\nu \rangle$ depend on whether there are two heavy and one light, or one light and two heavy states (Schechter-Valle theorem) [36]. Figure 2.6 shows a plot of $\langle m_\nu \rangle$ (labeled $m_{\beta\beta}$ in plot) as a function of the lightest neutrino mass for the two different mass hierarchy hypotheses [37, 38]:

1. The quasi-degenerate region where $m_1 \approx m_2 \approx m_3$. In this case $\langle m_\nu \rangle > \sqrt{\Delta m_{23}^2} > 0.05$ eV.

2. The inverted hierarchy scheme where $m_3 << m_1 < m_2$. In this case the effective mass is bounded above and below: $0.01eV < \langle m_\nu \rangle < 0,05eV$.

3. The normal hierarchy scheme where $m_1 < m_2 << m_3$. In this case $\langle m_\nu \rangle < 0.005$ eV.

If one can measure $\langle m_\nu \rangle$ to be less than 0.01 eV then one has shown that the hierarchy is normal.

Experimentally, $0\nu\beta\beta$ can be distinguished from $2\nu\beta\beta$ only by using the energy spectrum of the emitted electrons (see figure 2.7). In the $2\nu\beta\beta$ decay mode, some energy is given to the two

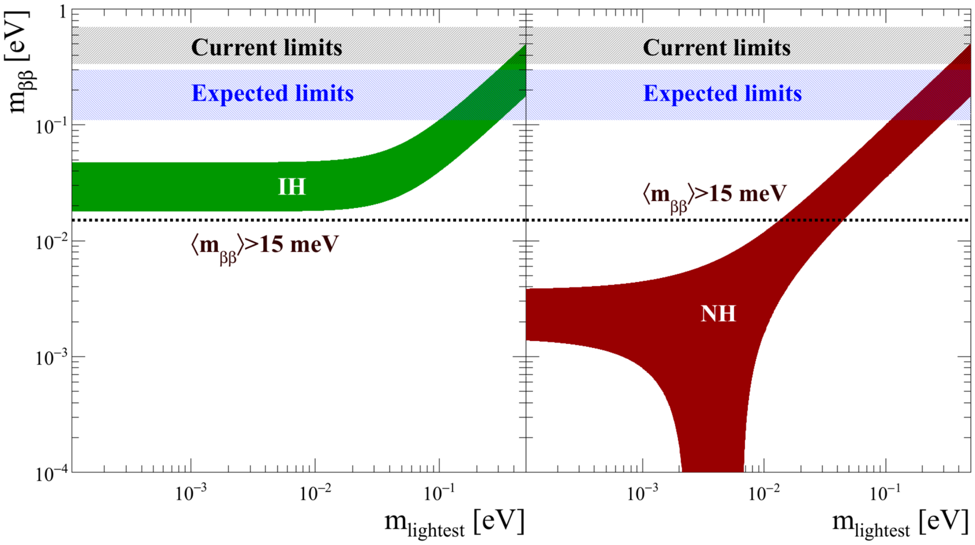

Figure 2.6: A plot of $\langle m_\nu \rangle$ as a function of lightest neutrino mass for the two different mass hierarchy hypotheses.

neutrinos, and hence — like in single beta decay — the electron energy spectrum is continuous. In contrast, in the $0\nu\beta\beta$ decay mode the full energy is given to the two electrons. Hence the sum of the kinetic energy of these electrons corresponds to the Q-value and shows up at a single peak at the endpoint of the $2\nu\beta\beta$ spectrum.

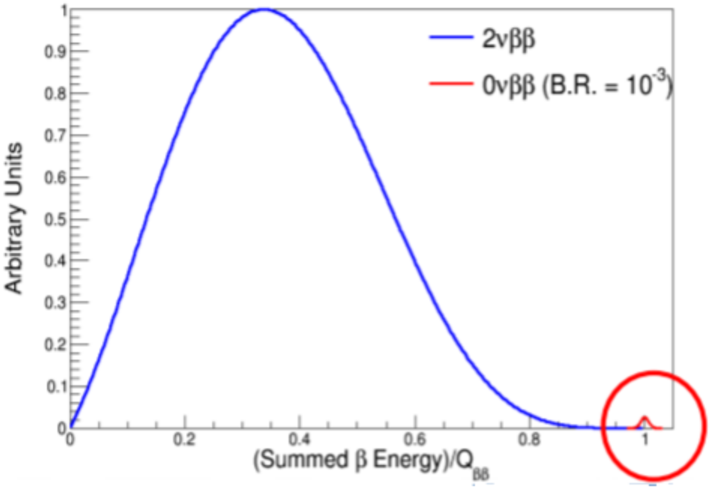

Figure 2.7: Double-beta decay spectrum. The 0ν mode would appear as a peak at the endpoint $Q_{\beta\beta}$.

2.4.1 Double-beta detection techniques

Semiconductor experiments

The source material is typically a semiconductor in crystal form [39, 40]. Electrons from a double beta decay event will ionize the semiconductor, leading to a cascade of electrons/hole pairs that drift to electrodes on the faces of the detector, generating a measurable voltage pulse. These detectors have very good resolution (sub 1% for 2 MeV electrons) owing to the fact that the number of electron/hole pairs is proportional to the energy of the emitted electrons. One disadvantage is that these detectors only measure the sum energy of the two electrons and there is usually a lot of background from other radioactive processes occurring in the source material. One of the leading experiments of this type is GERDA which is made of an array of Ge diodes (enriched to 86% ^{76}Ge) [41, 42]. See figure 2.8.

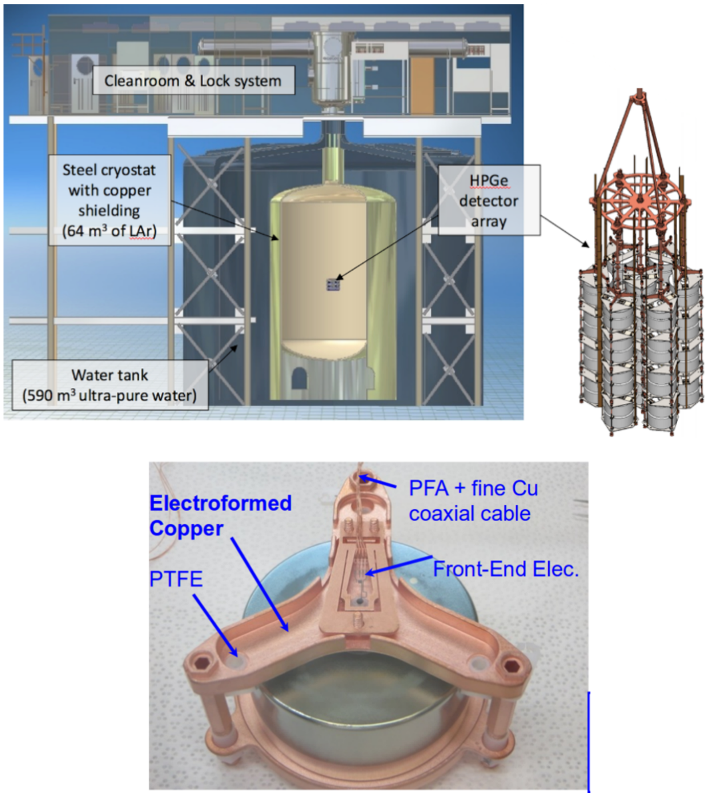

Figure 2.8: GERDA.

Cryogenic experiments

These types of experiments are similar to semiconductor experiments. The detector, typically a semiconductor crystal is kept at very low temperature, on the order of mK. The emission of the electrons from the double beta decay process raises the temperature of the source material by a tiny but measurable amount. These types of apparatus are known as bolometers. The leading experiment of this type is the Cryogenic Underground Observatory for Rare Event (CUORE) [43]. CUORE is composed of 968 $5 \times 5 \times 5$ cm^3 crystals, each weighing 750 g, and cooled to 7 mK. Figure 2.9 shows a diagram of the experiment. It went online in 2017 with a projected half-life sensitivity of ^{130}Te $T_{1/2}^{0\nu\beta\beta} \sim 9 \times 10^{25}$ yr [44].

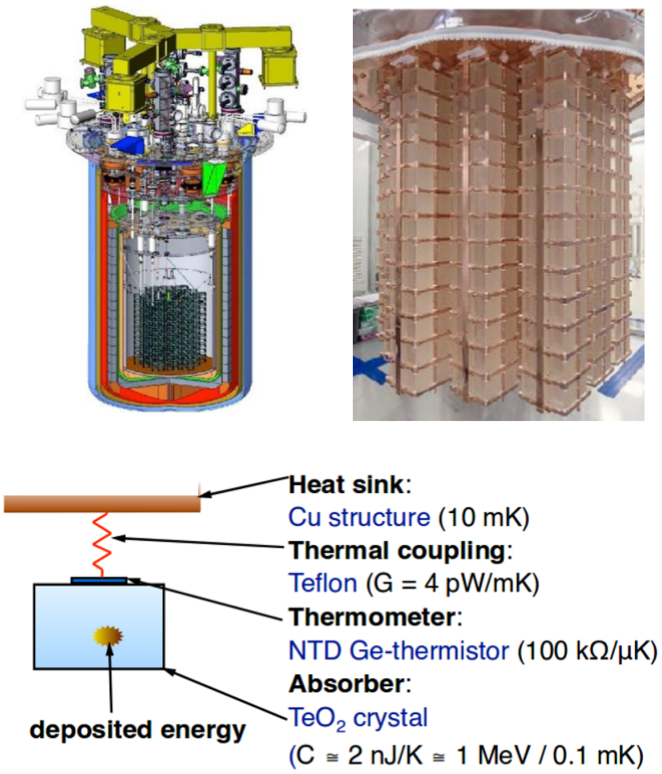

Figure 2.9: CUORE.

Scintillator experiments

These types of experiments use liquid scintillator (LS). Electrons from a double beta decay event will cause prompt scintillation light in the LS and their summed energy is subsequently measured.

The leading experiments of this types are KamLAND-Zen and SNO+. KamLand-Zen uses a mini-balloon (3.08 m diameter) full of Xe-loaded LS (13 tons) deployed in the middle of the existing KamLAND detector [45]. The Xenon is enriched to $\sim 90\%$ ^{136}Xe isotope and the inner ballon is surrounded by 1 kton of LS contained in a 13 m diameter outer ballon. The outer LS acts as an active shield [45]. The scintillation photons are detected by 1879 photomultiplier tubes mounted on a surrounding containment vessel [45]. One of the main disadvantages of these experiments is the energy resolution (7.3% at 2.458 MeV [45]). Figure 2.10 shows a diagram of the KamLAND-Zen experiment.

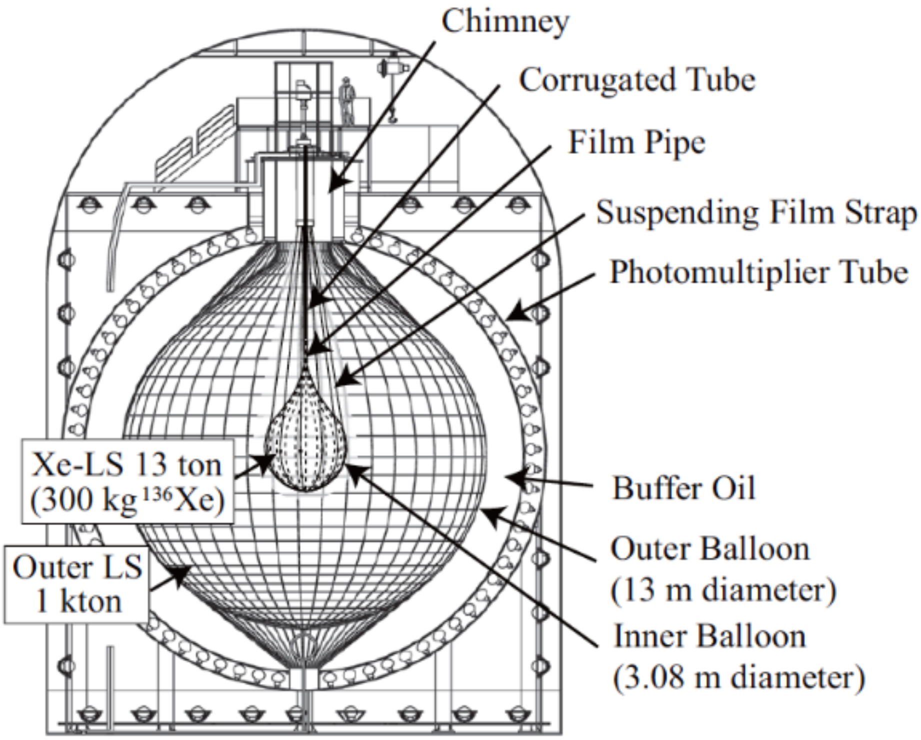

Figure 2.10: KamLAND-Zen.

Time Projection Chambers

The concept of a liquid time projection chamber (TPC) was first proposed by Rubbia [46] in 1977 for a large scale liquid argon detector dedicated to the study of proton decay. The concept is simple: charge carriers created inside a detection volume by ionizing particles drift along a uniform field toward a read-out plane see figure 2.11. We can thus identify the three main components of a TPC:

1. The detection volume: this is typically a gas or a liquid which is also the source of events to be detected.

2. The field cage: this is made of a cathode, an anode, and several field shaping rings in between. This creates a uniform electric filed which permeates the detection volume by reducing the electric potential ring by ring from the cathode to the anode.

3. The read-out plane: this is where charge carriers are detected. This can be implemented in a variety of ways. One of the most common is to have two wire planes at a crossed geometry for facilitating position reconstruction. The first plane (closest to the incoming/drifting) charge is called the induction plane and the second one is called the collection plane. This geometry is discussed in further details in section 3 with regards to EXO-200. Additionally photo-sensors can be placed around the field cage to detect light.

TPC's are powerful detection instruments because they allow three dimensional event imaging as well as energy measurement and particle identification. A light event would typically trigger (t_0) the detector. Charge carriers which drift are then detected some time t following the trigger and the drift time is given by:

$$t_d = t - t_0. \tag{2.45}$$

Let us say the field lines are along the z-direction. The z-coordinate of the event is determined as:

$$z = t_d \cdot v_e \tag{2.46}$$

It's important to note that light detection is basically instantaneous, especially since drift lengths are typically in the order of 1-30 cm (current generation experiments) to hundreds of centimeters (next generation/ ton scale experiments). x- and y- coordinates are derived from the energy signature on the induction and collection planes which are segmented, i.e. they are made out of groups of wires or pads. An example of TPC is the Enriched Xenon Observatory (EXO-200) which we discuss in more details in the next chapter.

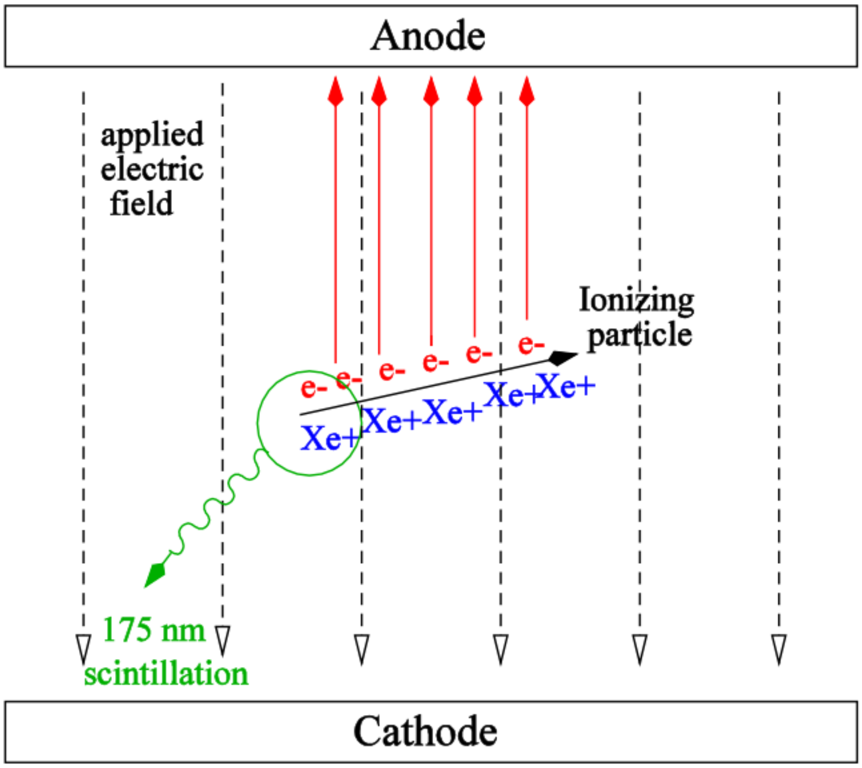

Figure 2.11: A Time Projection Chamber diagram. An ionizing particle creates charges which then drift in a uniform electric field toward the anode. With the proper choice of anode configuration both the x and y coordinate of the events can be determined. 3D imaging can be achieved by also collecting scintillation from the source material to calculate the drift time and z coordinate. Here the source is xenon.

Chapter 3

The Enriched Xenon Observatory

The Enriched Xenon Observatory (EXO-200) is a state of the art experiment to search for *neutrinoless double beta decay*. It has been in operation since 2011 in Carlsbad, New Mexico. EXO-200 uses xenon as both source and detector in a homogeneous, liquid phase TPC [47]. This gives it many advantages including event topology, efficacious self-shielding from external gamma backgrounds, and the ability to purify the xenon during its use. The xenon is enriched to 80.6% in the isotope ^{136}Xe and is operated at a temperature of 167 K and pressure of 147 kPa; under these conditions the liquid xenon has a density of 3.0 g/cm^3.

3.1 Sensitivity to $0\nu\beta\beta$

The experimental sensitivity is defined as the longest measurable half-life and is dependent on the number of background events and the exposure (source mass multiplied by the running time). Let us define the energy region of interest (ROI) δE. δE is typically determined (or limited) by the detector's energy resolution. Assuming the rate of background events in the ROI is constant, then the number of anticipated background events B is given by:

$$B = bMt\delta E \tag{3.1}$$

where b is the the rate of background events (in $keV^{-1}kg^{-1}yr^{-1}$)), M is the mass (in kg) of the $0\nu\beta\beta$ decays source, and t is the experimental running time t (in yr). The expected number of $0\nu\beta\beta$ decays $N_{0\nu\beta\beta}$ is given by:

$$N_{0\nu\beta\beta} = \lambda_{0\nu\beta\beta} N t \epsilon \tag{3.2}$$

where $\lambda_{0\nu\beta\beta}$ is the $0\nu\beta\beta$ decay rate, N is the initial number of isotopes undergoing $0\nu\beta\beta$ decay, and ϵ is the $0\nu\beta\beta$ event detection efficiency. Expressing N in terms of the isotopic abundance a, source mass M, and the isotope atomic mass m, equation 3.2 becomes:

$$N_{0\nu\beta\beta} = \lambda_{0\nu\beta\beta}(\frac{Ma}{m})t\epsilon = \frac{\ln 2}{T_{1/2}^{0\nu\beta\beta}}(\frac{Ma}{m})t\epsilon \tag{3.3}$$

where we've used the fact the half-life for an exponential decay process with decay rate λ is given by $T_{1/2} = \ln 2/\lambda$. Now let's write (as is customarily done) the condition for discovery of a $0\nu\beta\beta$ signal as:

$$N_{0\nu\beta\beta} = S\sqrt{B + N_{0\nu\beta\beta}} \tag{3.4}$$

where S is some multiple of the error of the underlying Poisson distribution. Setting $S = 1$ and remembering that background events are dominant in the ROI, it follows that:

$$N_{0\nu\beta\beta} \approx \sqrt{B} \tag{3.5}$$

$$\frac{\ln 2}{T_{1/2}^{0\nu\beta\beta}}(\frac{Ma}{m})t\epsilon \approx \sqrt{bMt\delta E} \tag{3.6}$$

$$T_{1/2}^{0\nu\beta\beta} \approx \ln 2 \frac{a\epsilon}{m}\sqrt{\frac{Mt}{b\delta E}} \tag{3.7}$$

Equation 3.7 implies that achieving the highest sensitivity for $0\nu\beta\beta$ requires a few critical conditions:

1. The source mass M should be as large as reasonably possible.

2. The experiment should be run for an extended period of time t.

3. the detector electronics should provide adequate detection efficiency ϵ. This is also achieved with the correct data analysis considerations.

4. the energy resolution δE at the Q-value should be optimized by ensuring that the ROI is as narrow as possible. This also suggests that the candidate isotope chosen should have a high Q-value.

5. In a background-free experiment $T_{1/2}^{0\nu\beta\beta} \propto Mt$ as opposed to $\sqrt{Mt}$. Every effort should be made to reduce the background rate.

All these considerations, which guided the design and construction of EXO-200, illustrate why neutrinoless double beta decay experiments are particularly challenging.

3.2 Liquid Xenon

The neutrinoless double beta decay program is rich and varied from the use of different isotopes to a multitude of experimental techniques. Liquid Xenon is particularly attractive for numerous reasons:

1. It serves as both the source and the detector.

2. It can be isotopically enriched to very high levels.

3. Its high atomic mass and density make it impenetrable to gamma backgrounds which are greatly attenuated. This property is often called self-shielding.

4. It can be reliably purified to facilitate long electron lifetimes.

5. There are no long-lived radioactive isotope of Xe produced via activation from cosmogenic sources.

6. Scintillation and ionization are anti-correlated in LXe, and this can be used to achieve superior energy resolution [48].

As the last item above states, a unique and important property of liquid xenon is the production of both electrons and scintillation photons in response to radiation. If detected efficiently, these ionization and scintillation signals can improve the resolution of LXe detectors.

3.2.1 Ionization

The energy deposited by ionization radiation into LXe is expended in the production of a number of electron-ion pairs N_i, excited atoms N_{ex}, and free electrons with kinetic energy lower than the energy of the first excited level (so-called sub-excitation electrons). The energy balance for this process first suggested by Platzman [49] is:

$$E_0 = N_i E_i + N_{ex} E_{ex} + N_i \epsilon \tag{3.8}$$

where E_0 is the energy deposited by the ionizing particle, N_i is the number of electron-ion pairs produced at an average expenditure energy E_i, N_{ex} is the number of excited atoms at an average expenditure energy E_{ex}, and ϵ is the average kinetic energy of sub-excitation electrons. The average energy required to produce one electron-ion pair is called the W-value and is given by:

$$W = E_0/N_i = E_i + E_x(N_{ex}/N_i) + \epsilon \tag{3.9}$$

Since solid and liquid noble elements and xenon in particular have been demonstrated to have band gap structures we can rewrite the Platzman equation with the band gap energy E_g as:

$$W/E_g = E_i/E_g + (E_x/E_g)(N_{ex}/N_i) + \epsilon/E_g \tag{3.10}$$

The ratios E_x/E_g and N_{ex}/N_i are estimated by using the oscillator strength spectrum of solid Xe obtained from photo-absorption data [16]. For an estimate of ϵ the Shockley model can be used and the resulting calculated W/E_g value for LXe is 1.65 [50].

The Fano factor defined by:

$$\sigma = \sqrt{FN_i} \tag{3.11}$$

is a quantity that parametrizes the number of electron-ion pairs produced when all of E_0 is absorbed. Fano was the first to realize that σ need not follow Poisson statistics [51]. Indeed $F = 1$ corresponds to Poisson statistics. The Fano factor for gaseous noble elements is well understood, where for example the theory for argon predicts $F = 0.16$ while experiment yields $F = 0.2$. However in the liquid phase it has been difficult to reconcile theory and experiment. In the case of LXe a value of $F > 20$ has been shown while theory predicts $F = 0.05$ [52]. This has impeded our understanding of energy loss and conversion in LXe and poses a problem for experiments because the large Fano factor limits the resolution of calorimeters used in nuclear and particle physics. Currently, the best energy resolution achieved in LXe is 30 keV at an energy of 554 keV [53, 54], which, extrapolated to the ^{136}Xe Q-value gives an energy resolution of 14 keV.

3.2.2 Scintillation

The production of scintillation photons in LXe is the result of relaxation of excited Xe dimers. The dimers are created in two ways [16]:

1. direct excitation by an energetic particle

$$\begin{aligned} Xe^* + Xe + Xe &\rightarrow Xe_2^* + Xe, \\ Xe_2^* &\rightarrow 2Xe + h\nu \end{aligned}$$

2. recombination of electron with a xenon molecular ion

$$\begin{aligned} Xe^+ + Xe &\rightarrow Xe_2^+, \\ Xe_2^+ + e^- &\rightarrow Xe^{**} + Xe \\ Xe^{**} &\rightarrow Xe_2^* + heat \\ Xe^* + Xe + Xe &\rightarrow Xe_2^* + Xe, \\ Xe_2^* &\rightarrow 2Xe + h\nu \end{aligned}$$

The released photon is in the VUV (vacuum uv) range with a wavelength of 177.6 nm. LXe being transparent to VUV light, the photon propagates freely to the photodiode where it is detected (see next section)

3.2.3 Anti-correlation

As already mentioned the anti-correlation between the ionization and scintillation signals can be used to improve the energy resolution in a LXe detector [48]. Figure 3.1 illustrates this autocorrelation using events from an EXO-200 source calibration runs. It is important to note the anti-correlation in question here is a microscopic effect which is distinguishable from the macroscopic anti-correlation that can result in the presence of high electric fields and whereby ionization electrons are prevented from recombining and generating scintillation photons.

3.2.4 Self-shielding

Shielding a detector from gamma rays is difficult. Figure 3.2 shows a plot of the cross section vs photon energy. The Q-value for ^{136}Xe $0\nu\beta\beta$ is 2.458 MeV. Gamma rays of this energy have an attenuation length less than 8 cm. This means that a large enough LXe detector would conceivably have an inner volume isolated from external gamma rays. EXO-200 somewhat benefits from this but not to the extent that nEXO will, discussed in chapter 5 will.

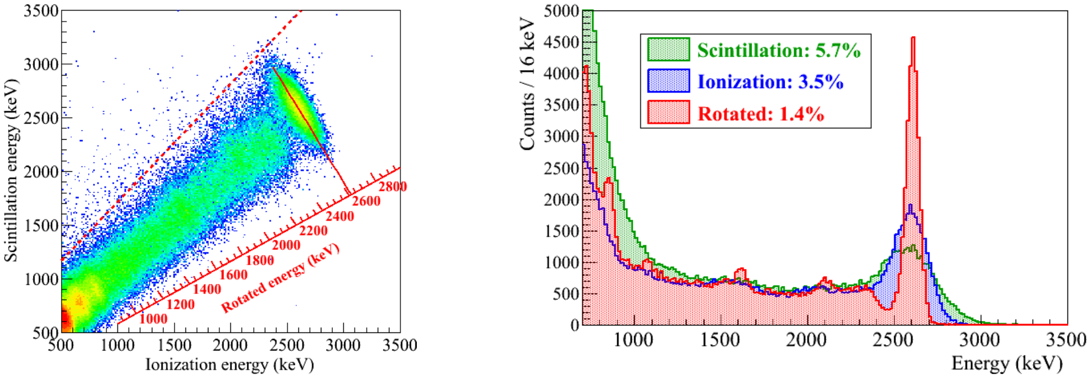

Figure 3.1:]
Calibrated ionization energy vs calibrated scintillation energy for EXO-200 Th-228 source run.

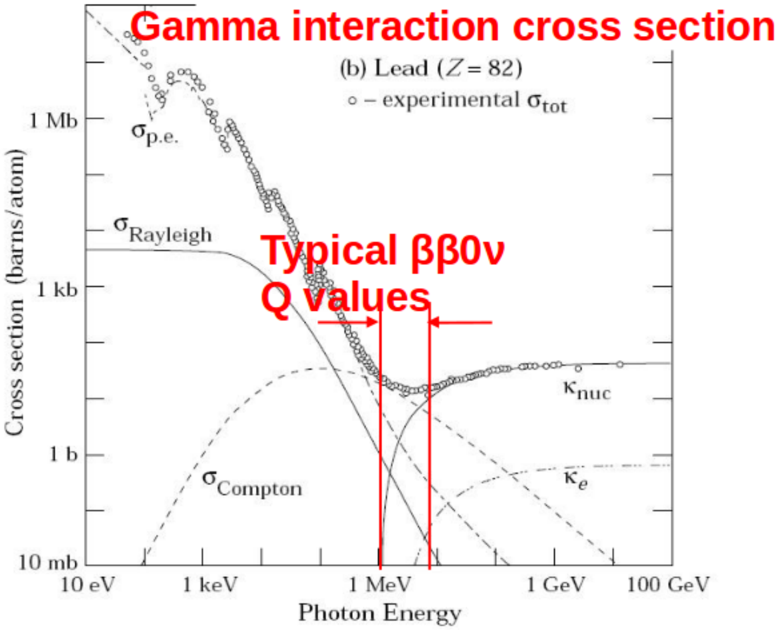

Figure 3.2: Gammas with energy similar to the Q-value of ^{136}Xe $0\nu\beta\beta$ are greatly attenuated by LXe.

3.3 Apparatus

3.3.1 Materials and construction

Very low background levels are achieved by selecting ultra-low radioactivity construction materials [55], minimizing the masses of passive components through careful design, specially cleaning and storing components before assembly, and building the detector in progressively clean, shielded layers. The LXe container ("vessel") was machined from selected copper stock and assembled using electron-beam welding. In order to reduce the activity nearest to the LXe, the copper vessel was built with a 1.37 mm thickness that is designed to reliably support only a 35 kPa pressure differential (in either direction). The copper vessel is designed to closely envelop the active Xe volume,flaring out at the ends to contain the frames of the wire planes, the LAAPDs, and the wiring. The vessel is welded shut at the two ends with a TIG field weld to minimize the use of materials and avoid sealing problems. An elaborate control system ensures that the pressure inside the TPC vessel tracks the pressure outside to within a tight tolerance ($\sim \pm 4$ kPa) during detector pump down, purge, cooling, liquid fill, and normal operations.

The cryostat is a twelve-sided, double walled, vacuum insulated copper vessel, made from specially selected low background copper. The copper was freshly produced in a dedicate low background run for EXO by the Norddeutsche Affinerie (now Aurubis, Germany [56]) to minimize its exposure to the cosmic radiation. The cryostat contains a total of 5901 kg of copper. All these components, with the exception of the muon veto, are located inside a class 1000 clean room. The inner cryostat contains an ultra-clean, dense (ρ = 1.8 g/cm^3 at 170 K) fluid (HFE-7000 [57]), providing both shielding and thermal uniformity. The fluid also transfers the pressure load to the 25 mm thick inner cryostat copper vessel that is designed to tolerate absolute implosive (explosive) loads $>$ 100 kPa ($>$300 kPa).

3.3.2 The TPC

The TPC is designed for the collection of both scintillation and ionization signals. The LXe vessel volume of 58 liters is set by the total amount of enriched Xe available. This volume includes the Xe and cable conduits and the high voltage (HV) feed-through, shown in figure 3.3, that are full of LXe during normal operations. The total mass of LXe in EXO-200 is $\sim$ 175 kg, with 110 kg available in the active detector volume. The remaining mass of Xe is in the gas handling system.

As previously discussed radiation depositing energy in LXe produces both scintillation and ionization. The scintillation is detected almost instantaneously by large-area avalanche photodiodes

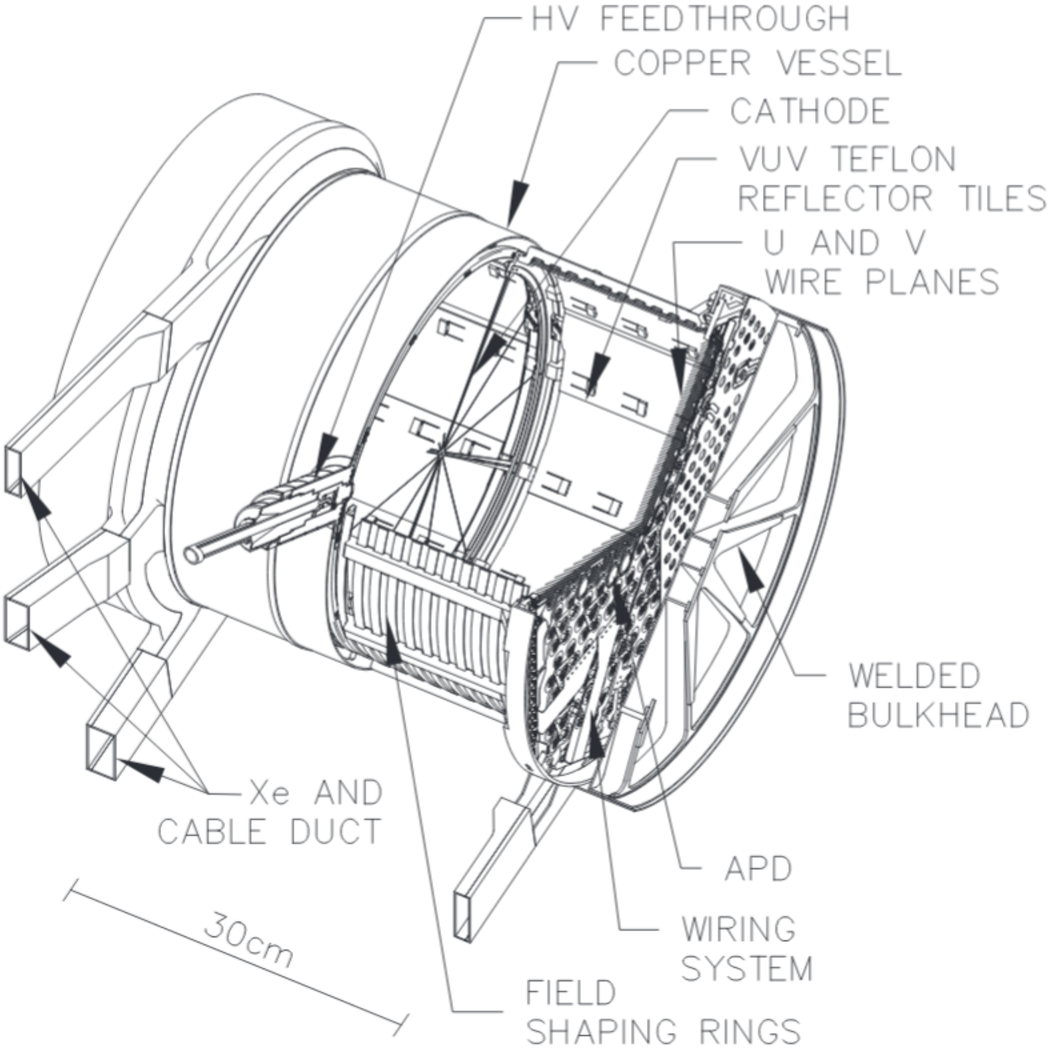

Figure 3.3: Cutaway view of the EXO-200 TPC with the main components identified. Picture from [58].

(LAAPDDs) while the ionization is drifted in a uniform electric field to a set of crossed wire planes. The TPC is divided into two almost identical drift regions, one of which is shown in figure 3.4. A cathode grid held at negative high voltage separates the two regions while the readout planes at both ends are held at ground potential. With this arrangement the drift voltage is reduced by a factor of two at the expense of little extra material (the cathode) in the active xenon volume.

The scintillation light is collected using 468 LAAPDs. These were chosen because compared to photomultiplier tubes (PMTs) they have substantially lower radioactivity, occupy less space, are

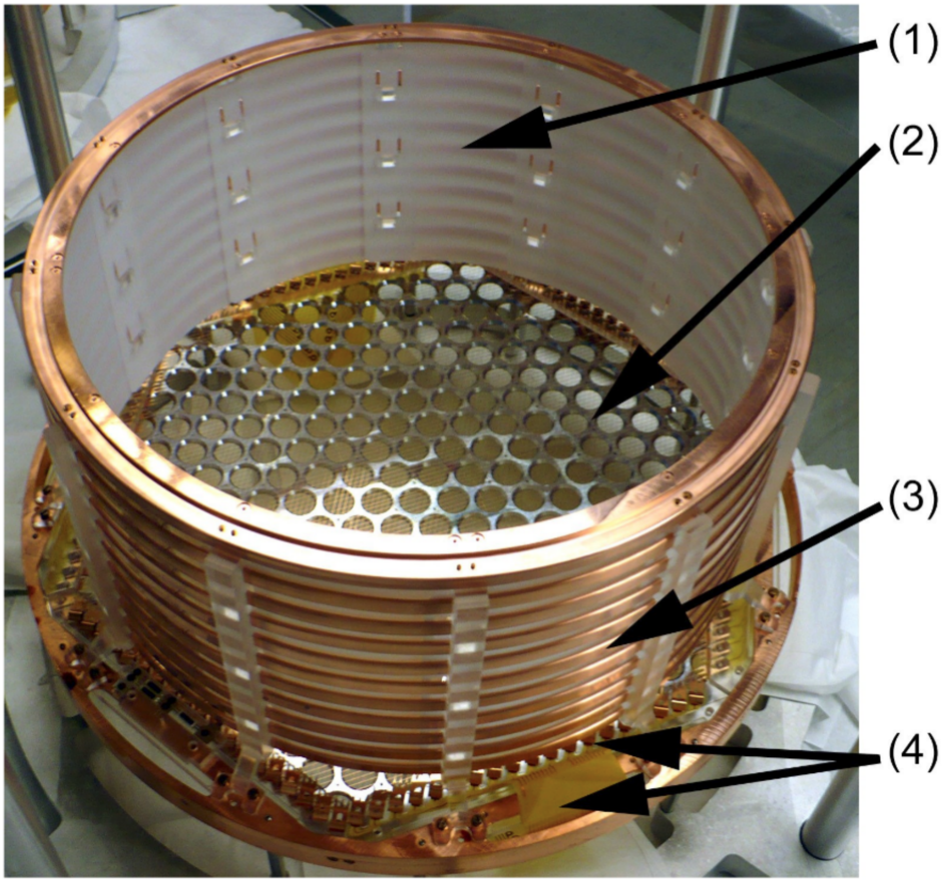

Figure 3.4: A view into the active Xe volume of one of the two EXO-200 TPC modules. PTFE tiles (1) installed inside the field-shaping rings serve as reflectors for the scintillation light. The aluminum-coated side of the LAAPD platter (2) is visible, as well as the field cage (3), ionization wires, and flexible cables(4).

intrinsically compatible with cryogenic operation, and have higher quantum efficiency at 178nm. Howver they have lower gain and higher noise at the operating temperature which was ok ^{136}Xe searches ($Q_{\beta\beta} = 2615$ keV) but turned out to be an obstacle for the ^{134}Xe ($Q_{\beta\beta} = 825$ keV). Light collection efficiency is improved through the use of reflective PTFE tiles around the field cage. Furthermore the cathode has a 90% optical transparency so that the LAAPD detect scintillation produced anywhere in the active LXe.

Each LAAPD has a 16 mm diameter active area (200 mm^2), with an overall diameter between 19.6 mm and 21.1 mm. The thickness of each varies between 1.32 mm and 1.35 mm. All LAAPDs were manufactured in a class 1000 clean room and stored in static dissipative boxes under nitrogen

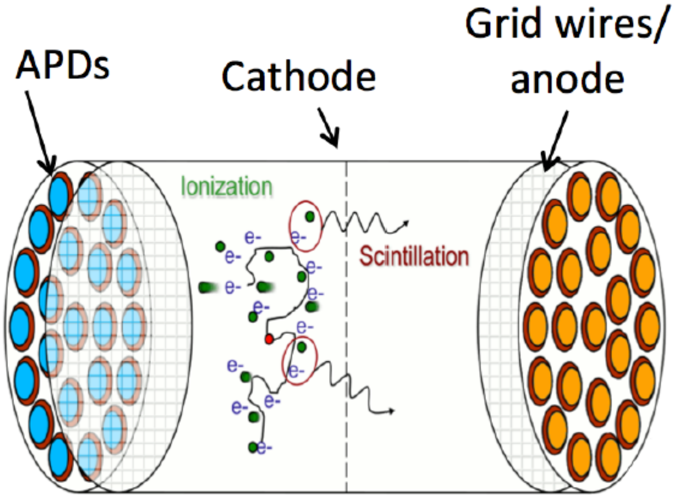

Figure 3.5: EXO -200 TPC concept.A central cathode (12 kV) splits the TPC in two identical drift regions. Charges drift toward and anode which is composed of V wire for induction and U wire for charge collection. Behind the U wires are large area avalanche photodiodes for the collection of scintillation light.

atmosphere from production to installation. The LAAPDs platters are machined from the same low-activity copper as the LXe vessel.

The ionization channel comprises the TPC cathode and field cage, defining a region of uniform electric field, the charge collection (U) wire plane, sitting at virtual ground, and a shielding (V) wire plane located in front of the U wires and biased to ensure full electron transparency. The V wires are also read out, and their inductive pickup signals provide a second coordinate without an additional shielding wire plane. Both U and V wires are in front of the LAAPDs, and each has 95.8% optical transparency. The distances between the two wire planes and the APD platter (6 mm each) and the wire pitch (3 mm) were chosen to maximize the fiducial volume while not requiring excessive high voltage on the V wire plane to achieve electrical transparency. Figure 3.6 shows a diagram of the readout planes.

EXO-200 was designed to operate at a maximum drift field of 3.7 kV/cm. The drift region, 38.4 cm in length and with a radius of 18.3 cm, is bound radially by a series of copper field shaping rings (outer diameter of 37.4 cm) and longitudinally by the V wire plane. Each ring is 0.97cm long and the pitch between ring is 1.69 cm. For each drift region the electric field is graded in ten steps

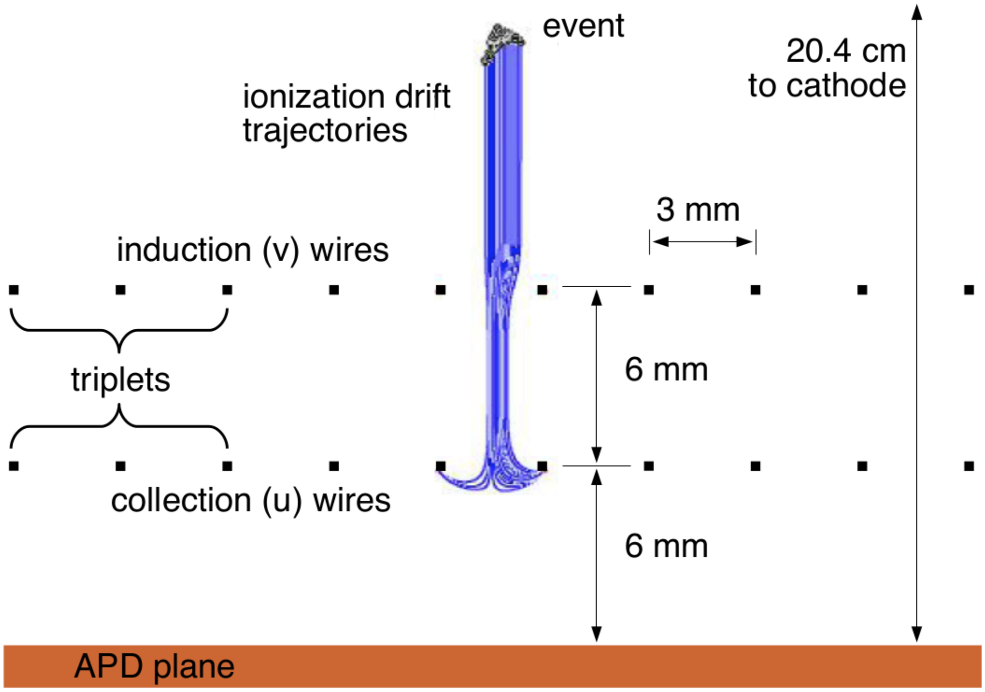

Figure 3.6: EXO wire geometry.

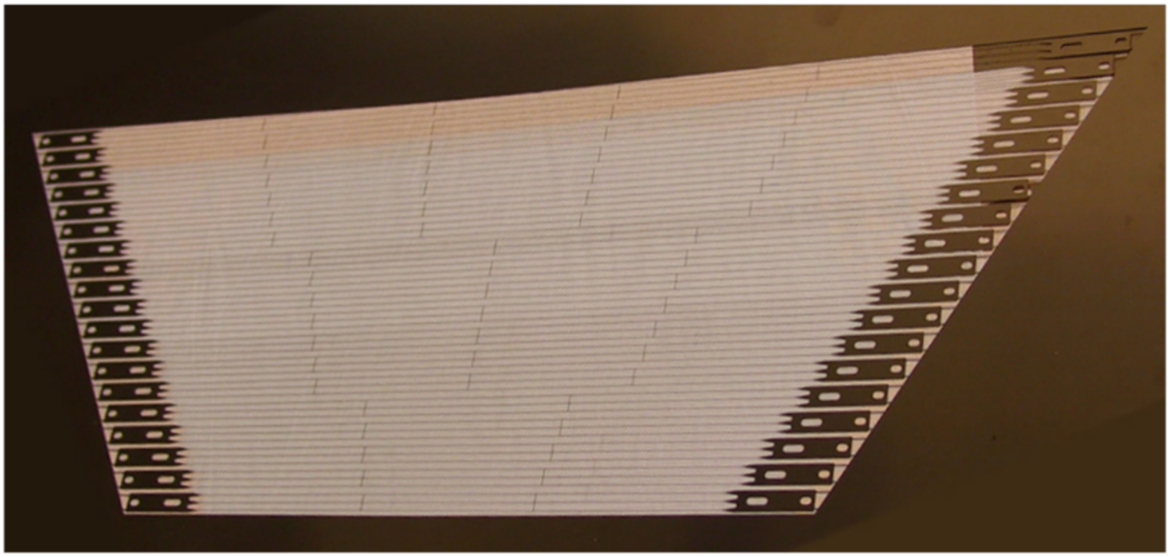

Figure 3.7: A panel of photoetched phosphor bronze wires. The panel contains wire triplets for half of one U or V wire plane.

from the cathode (to the V-wire) with the use of ten 900 MΩ resistors.

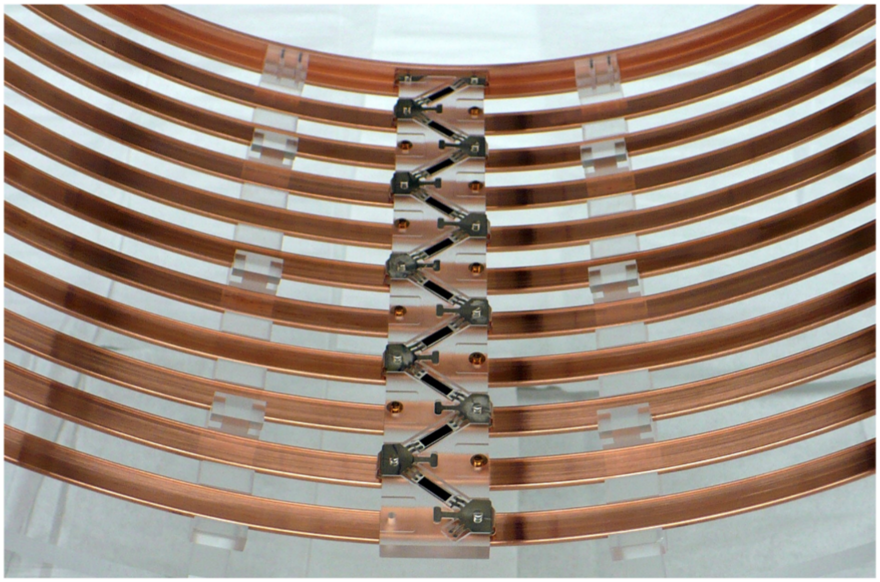

Figure 3.8: The resistor chain which grades the electric field in each TPC. Platinum plated phosphor bronze springs make contact between the resistors and field shaping rings.

3.3.3 LXe system

EXO-200 maintains $\sim$ 200 kg of the xenon mass in liquid form. To keep this stable a sophisticated cryogenic system was built. Figure 3.9 shows a simplified schematic of this system. The xenon is fed from storage bottles into a set of purifiers in gas form. The purifiers mainly removes electronegative impurities such as O_2 and N_2. From there the gas goes into purity monitor (GPM 2) where the electron lifetime is measured. Then the xenon gas is liquefied by the condenser which is coled by a commercial cryogenic refrigerator to $\sim$ 167 K. The liquid xenon then flows into the vessel/tpc which sits in a (inner) cryostat filled with HFE-7000, a commercial cryogenic fluid. The thermal HFE bath transfers heat from the vessel to the wall of the inner cryostat which is inside a large outer cryostat. The outer cryostat is also cooled with a commercial refrigerator and removes heat from inner walls. The xenon flows from the vessel to the heater where it is vaporized and then fed into a purity monitor GPM 3. From tGPM 3 the gas xenon Goes through a recirculation pump that pushes it back into the purifier so that the process repeats.

The system is monitored 24 hours a day to ensure stable operation. The TPC is maintained at an overpressure of 8.1 kPa relative to the HFE bath. The ”bleed” and ”feed” valves ensure that

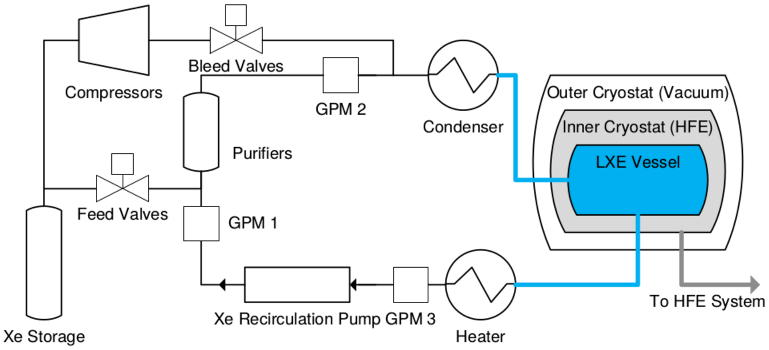

Figure 3.9: Schematic of the EXO-200 gas handling, cooling, and recirculation system.

xenon can be vented out (and recovered) or injected as needed should the overpressure vary outside the tolerance window. This happens very rarely. The tolerance window was set to ensure the thin copper vessel would not collapse due to pressure changes.

3.3.4 Electronics

The fast data-acquisition (DAQ) system for the EXO-200 detector integrates the readout of 226 hardware channels (76 U-wire signals, 76 V-wire signals, and 74 APD gangsignals), muon veto panel output, and a high-voltage (HV) glitch detector into a single data stream. The veto system triggers asynchronously from the TPC when both instrumented ends of a panel record a hit within a 1-μs coincidence time window. The HV glitch detector monitors high-voltage transients with $\sim$ μs duration.

Each TPC hardware channel is coupled to the DAQ via front-end electronics, consisting of a low-noise charge amplifier with a dual two-stage shaper followed by a 12-bit, 1 MS/s analog-to-digital converter. The digitized data are fed to a trigger electronics module (TEM), which synchronizes the data from all hardware channels and forms detector triggers.

For the muon veto, each panel's light-readout channels (four PMT), are fed into a discriminator module, which supplies a bit pattern of the panels above threshold. For a valid trigger, both ends of any one panel are required to be simultaneously above threshold to reduce the random trigger rate.

Whenever a trigger condition is met, data is written from the TEM to a control computer to

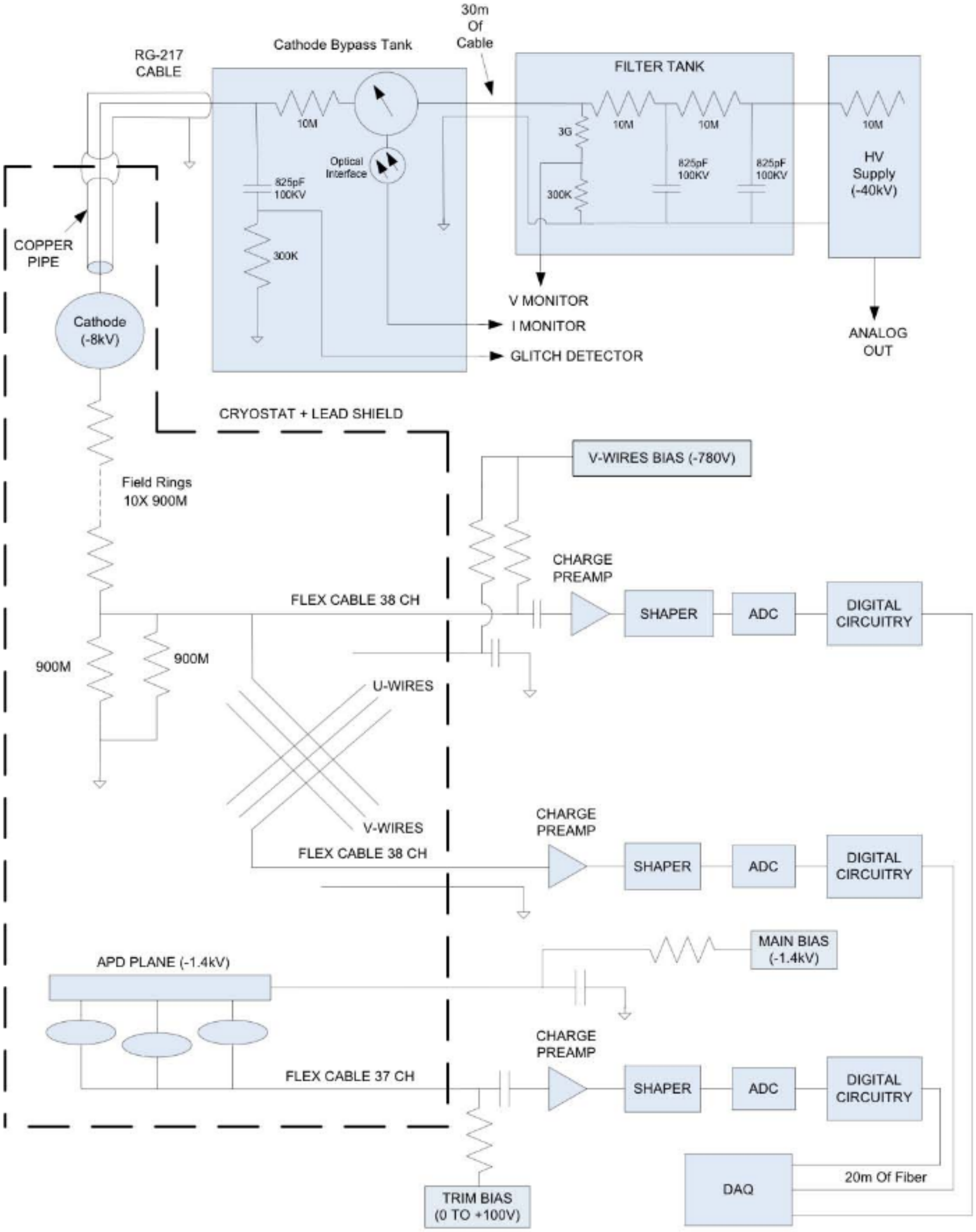

Figure 3.10: TPC biasing and readout electronics systems (2011 original). The bias voltages are indicated for a cathode potential of -8 kV. After an electronics upgrade in 2015 and 2016 the applied voltage is now -12 kV.

be stored on disk. If a TPC trigger occurs, the TEM transfers digitized data for all 226 hardware channels for sample times starting 1024 μs before the trigger to ending 1024 μs after it. During a normal physics run, there are four types of TPC triggers used, with rough thresholds noted in parentheses: (a) individual U-wire trigger for LXe γ and β events ($\sim$ 100 keV), (b) APD individual trigger for activity inside the respective APDs ($\sim$ 3–4 keV), (c) APD sum trigger for LXe α events ($\sim$ 25 000 photons), and (d) solicited (forced) trigger at 0.1 Hz, for monitoring detector performance.

3.3.5 Calibration System

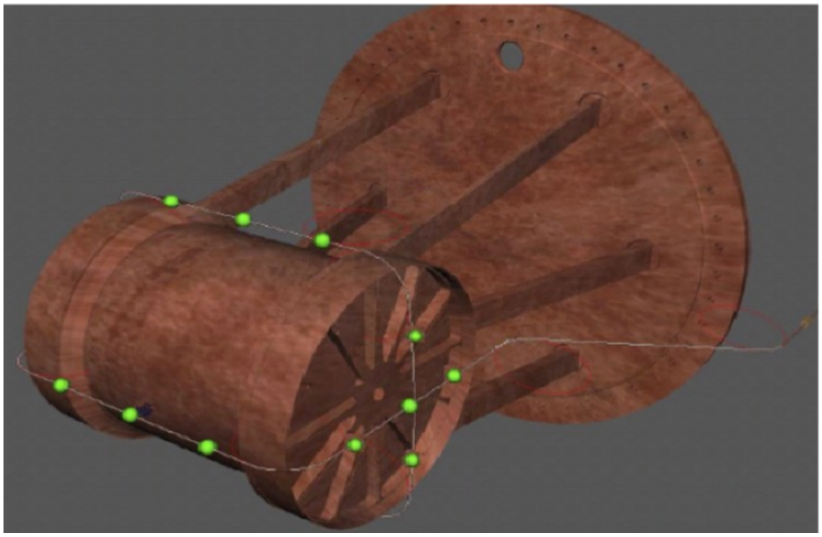

Figure 3.11: Calibration guide tube position around the LXe vessel.

In order to understand and monitor the response of the TPC to ionizing radiation, calibration with radioactive γ-ray sources (^{137}Cs, ^{60}Co, and ^{228}Th) are performed three times a week. Sources are deployed around the detector to known locations via a copper guide tube that wraps around the outside of the LXe vessel in the HFE-7000 volume (see Figure 3.11). This delivery method ensures that the sources are close enough to the detector and large full absorption efficiencies in the active detector volume are achieved.

3.3.6 WIPP, clean room, and veto system

EXO-200 is located at a depth of 1624 m.w.e at the Waste Isolation Pilot Plant (WIPP) near Carlsbad, New Mexico. The actual depth is approximately 2150ft (650m). WIPP is a Department of Energy (DOE) facility built for the permanent disposal and storage of low-level radioactive waste left from the production of nuclear weapons [59]. WIPP is located in a salt deposit which has high levels of $40K$ and is naturally low in ^{238}U and ^{232}Th in contrast to typical hard rock mines. WIPP was selected to house EXO-200 because of existing underground facilities.

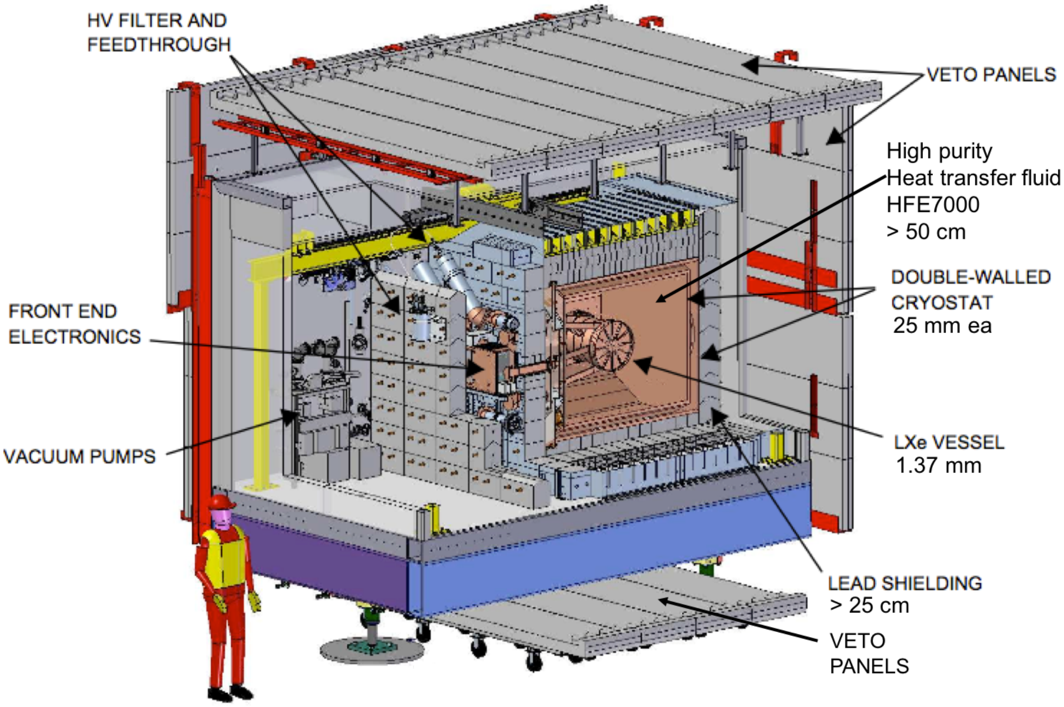

Figure 3.12: Cutaway view of the EXO-200 setup. Primary sub-assemblies are also identified.

Figure-3.12 shows a view of the underground installation, including a class 1000 clean room, a double-walled copper cryostat with 25 cm of lead shielding, and an active muon veto system. The detector as well as all supporting systems are housed in connected class 1000 clean room modules. To ensure low levels of particles in the air rigorous protocols are implemented, including requiring that personnel and all visiting shifters clean off and wear designated protective suits before entering clean room.

The TPC sits in the cryostat and is immersed in ultra-clean heat transfer fluid (HFE-7000).

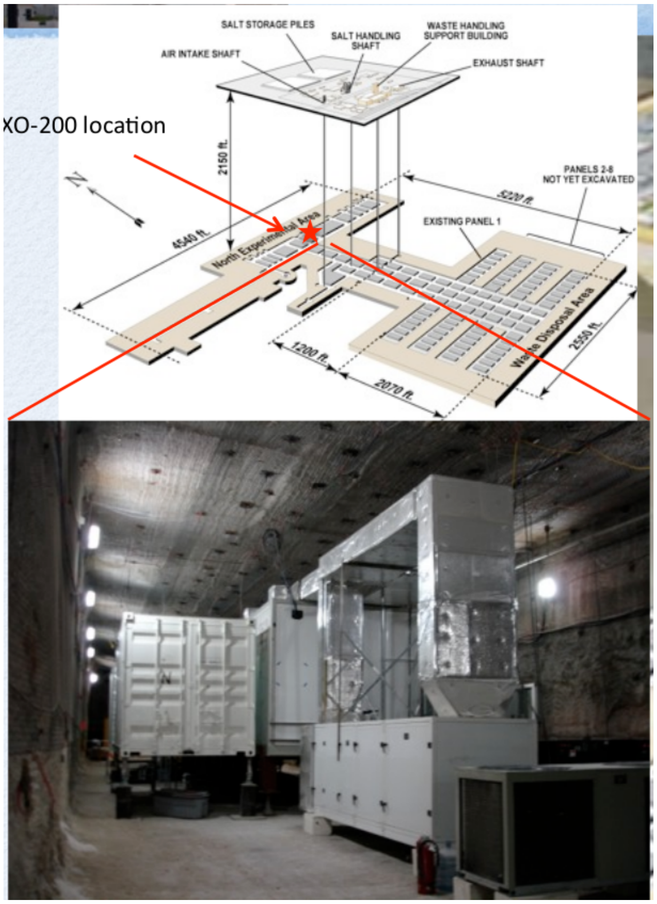

Figure 3.13: EXO-200 at WIPP.

With a thickness $>$ 50 cm HFE has the added benefit of being an absorber of thermal neutrons via neutron captures on the ^{1}H in the HFE molecule. The lead shield, due to lead's high atomic mass and density, passively blocks gammas from external background sources.

In order to identify TPC events induced from cosmic ray muons, 29 Bicron BC-412 plastic scintillator panels, each optically coupled to 8 photo-multiplier tubes (PMTs), surround the exterior of the clean room module housing the detector to provide $> 95\%$ solid angle coverage. The scintillator panels are composed of a polymerized organic molecule that will emit faint scintillation light in response to the passage of ionizing particles, such as cosmic ray muons, through the panel. Following such an event, the PMTs immediately detect the faint scintillation light. Together, all the panels and PMTs are enshrouded in a light-tight thin material. Coincidences on any two PMTs within 1 μs of each other will trigger the veto system and be recorded through the TEM (see

Section 4-1).

3.3.7 Detector performance

The EXO-200 detector has met or exceeded its design goals in all major areas: electron lifetime, energy resolution, and background rejection capability using event topology (discussed in next chapter). The xenon in the TPC is continuously recirculated and cleaned by a hot getter gas purifier. At a flow rate of > 15 slpm (standard liters per minute), electron lifetimes of 3–5 ms are routinely achieved in EXO-200. The electron lifetime is likely limited by outgassing of impurities from the large plastic surfaces (Teflon, acrylic, and Kapton) in direct contact with the LXe (see subsection).

Detector energy resolution is a critical parameter for double beta decay experiments, as it is the only experimental handle for separating $0\nu\beta\beta$ events from the tail of $2\nu\beta\beta$ continuum. As already discussed, energy conservation requires that the light and charge signals from LXe detectors be anti-correlated. By forming a linear combination of the two signals, the detector energy resolution can be improved considerably. This technique was first demonstrated in a small LXe test cell by the EXO-200 collaboration [48], and later confirmed by other groups [60]. The same anti-correlation is observed in the EXO-200 detector (see figure 3.1). EXO-200 was designed to reach an energy resolution of 1.6% at $Q_{\beta\beta}$, but was able to achieve an energy resolution of 1.23% in its Phase-II running. Detailed simulation and analysis show that the energy resolution is limited by the APD front end electronic noise, APD avalanche gain fluctuations, and the overall light collection efficiency.

The EXO-200 detector demonstrates the power of LXe TPCs for rejecting background events. As a monolithic detector, surface αs and βs can be rejected by a fiducial volume cut. Decays producing αs inside the LXe bulk are rejected by a light to charge ratio cut, as α events create much denser charge clouds than electrons, and therefore a larger amount of scintillation light is produced from recombination. Coincidence techniques can also be used to identify backgrounds. For example, the delayed coincidence of ^{214}Bi–^{214}Po is used to measure the ^{222}Rn content of the LXe. In stable operation, the ^{222}Rn in the detector is found to be 3.6 ± 0.4 μBq/kg (~ 1 decay/hr)

[61].

For γ backgrounds, which preferentially Compton scatter leaving multiple energy depositions, the 3-D event reconstruction capability of a TPC and its monolithic active volume are critical for background rejection. TPC events can be separated into “Multi Site” (MS) and ”Single-Site” (SS) events based on the number of spatially separated energy depositions inside the chamber (This is discussed in details in the analysis/next chapter). Events in the MS spectrum are predominantly Compton scattering events and are excluded from the signal region. Furthermore, the MS spectrum measures the γ backgrounds, providing constraints on the leakage of such background events into the SS spectrum. The observed SS/MS ratio for the EXO-200 detector is approximately 1:5 near the $Q_{\beta\beta}$ value. In the most recent 0ν analysis (published March 2018), topological information for each event was used to further discriminate between signal and γ backgrounds in the SS event population. A multivariate discriminator was developed that combines the number of collection wires for each event, the signal rise time, and the event standoff distance (defined as the distance of the event vertex from the nearest detector surface) in a boosted decision tree (BDT) using the TMVA software package [62]. The use of BDT variable provides a $\sim 15\%$ increase in sensitivity compared to the SS/MS classification alone [63]. The search carried in this thesis uses the standard SS/MS discrimination described in the next chapter.

3.4 Main physics results

With its first 2 years of data taking EXO-200 was able to publish the most precisely measured half-life of any $2\nu\beta\beta$ decay to date, namely $T_{1/2}^{2\nu\beta\beta} = 2.165 \pm 0.016(stat) \pm 0.059(sys) \times 10^{21}$ yr. Figure 3.14 shows the best-fit model for the single site (described in more details in Chapter 4) spectrum for the ^{136}Xe $2\nu\beta\beta$ search:

In 2018 EXO-200 published results from a search for $0\nu\beta\beta$ decay of ^{136}Xe. This analysis used the first year of data taken with the upgraded detector (Phase ii dataset). The detector upgrade performed in the earlier part of 2016 primarily consisted of an electronics upgrade that aimed to

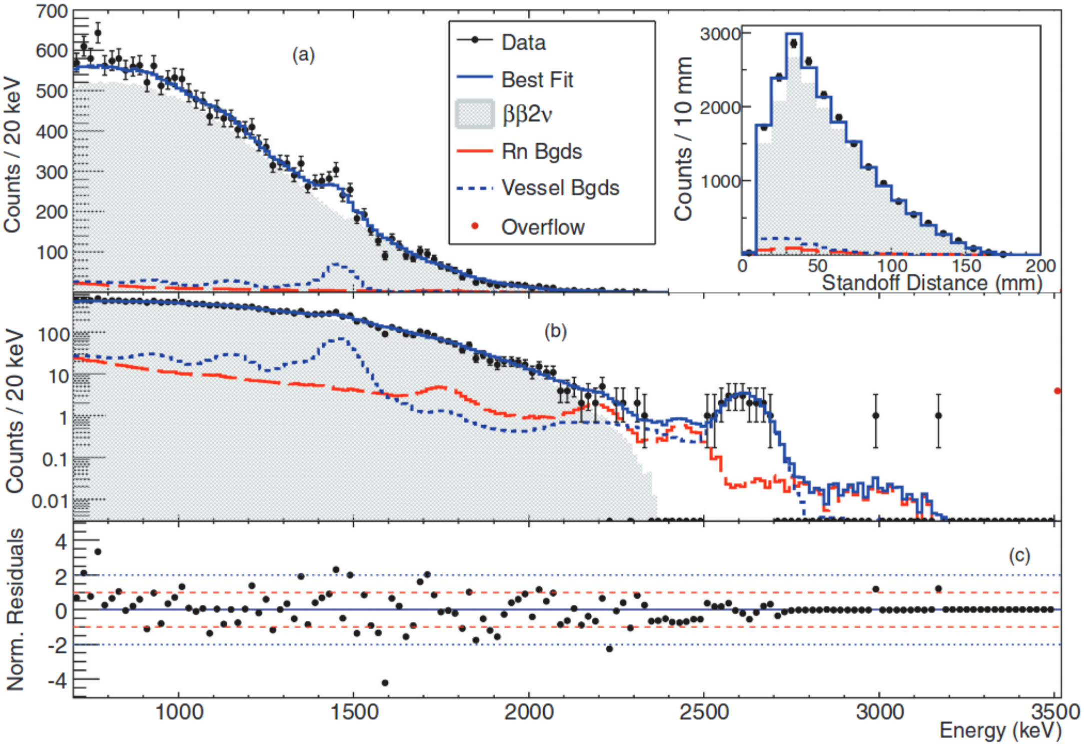

Figure 3.14: Fit results. Data and PDFs for single site (SS) energy spectra shown in linear (a), log (b), with residuals (c). The residuals have been normalized by the bin error. SS standoff distribution is also shown (inset). Backgrounds have been grouped together according to Rn components and components in or near the TPC vessel.[11]

minimize the APD readout noise observed in Phase I (data taken between 2011 and Feb 2014) [11, 12, 58]. This upgrade had a substantial impact on the detector performance, improving the livetime and position averaged resolution from $\sigma/E(Q_{\beta\beta}) = 1.38\%$ in Phase I to 1.23% in Phase II (see figure 3.15) [63]. This led to a combined (Phase I + Phase II) median 90% confidence level $0\nu\beta\beta$ half-life sensitivity of 3.7×10^{25} yr – a twofold increase from the Phase I value. A lower limit on the $0\nu\beta\beta$ half-life of 1.8×10^{25} yr was also set. Fits from this analysis are shown in figure-3.16.

The EXO-200 results are competitive with other leading experiments, as shown in Table 3.1. The Majorana neutrino mass limit of EXO-200 is comparable to those of GERDA and CUORE. Although EXO-200 has a lower $0\nu\beta\beta$ decay half-life limit than KamLAND-Zen, the sensitivities of the two experiments are close and, providing a more specific signature, EXO-200 has better handles to validate a signal in the case of a discovery. EXO-200 will continue to take data until the

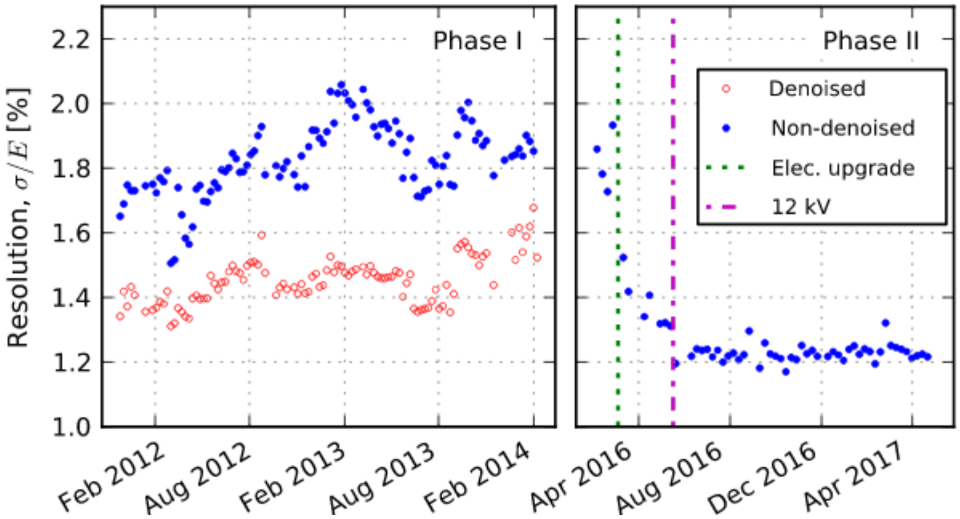

Figure 3.15: Measured energy resolution σ/E for the 2615 keV ^{208}Tl γ line in calibration data taken at the cathode position throughout Phase I and Phase II. The measured resolution before (blue) and after (red) applying the software denoising algorithm in Phase I is shown [63]

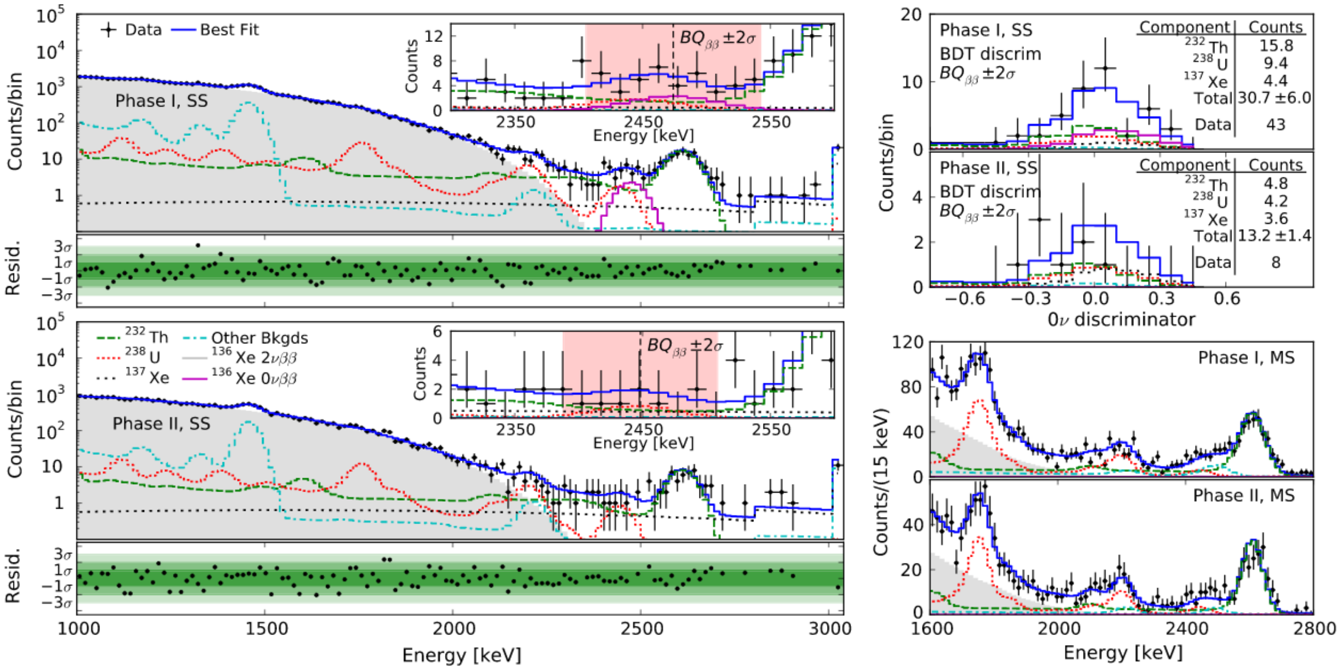

Figure 3.16: Best fit to the low-background data SS energy spectrum for Phase I (top left) and Phase II (bottom left). The energy bins are 15 and 30 keV below and above 2800 keV, respectively. The inset shows a zoomed-in view around the best-fit value for $BQ_{\beta\beta}$. Top right: Projection of events within $BQ_{\beta\beta} \pm 2\sigma$ on the BDT fit dimension. Bottom right: MS energy spectra above the ^{40}K γ line. [63]

end of 2018. With the entire data set, it is expected to reach a $0\nu\beta\beta$ decay half-life sensitivity of 5.7×10^{25} yrs, as shown in Figure 3.17.

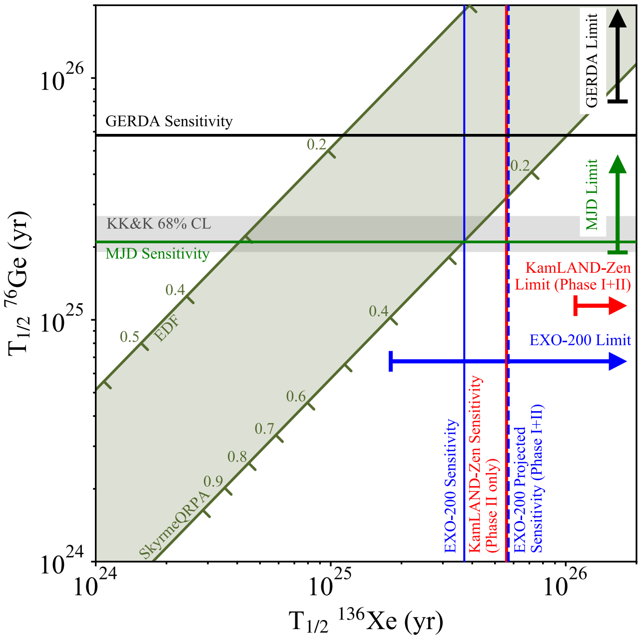

Figure 3.17: Comparison of ^{76}Ge and ^{136}Xe derived $0\nu\beta\beta$ half-lives. The horizontal and vertical lines represent the GERDA [42], MAJORANA DEMONSTRATOR (MJD) [64], KamLAND-Zen [45], and EXO-200 [63] sensitivities and limits. The shaded diagonal band indicates uncertainties due to different matrix element calculations. The marks on the diagonals denote model-specific effective Majorana neutrino masses.

Experiment	Isotope	Exposure (kg·yr)	$T^{0\nu}_{1/2}$ sensitivity (yrs)	$T^{0\nu}_{1/2}$ limit (yrs)	$\langle m_{\beta\beta}\rangle$
EXO-200 [63]	^{136}Xe	177.6	3.7×10^{25}	$> 1.8\times10^{25}$	< 0.15-0.40
KamLAND-Zen [45]	^{136}Xe	504	5.6×10^{25}	$> 10.7\times10^{25}$	< 0.06-0.17
GERDA [42]	^{76}Ge	46.7	5.8×10^{25}	$> 8.0\times10^{25}$	< 0.12-0.26
MJD [64]	^{76}Ge	9.95	2.1×10^{25}	$> 1.9\times10^{25}$	< 0.24-0.52
CUORE [44]	^{130}Te	86.3	0.7×10^{25}	$> 1.3\times10^{25}$	< 0.11-0.52

Table 3.1: A list of $0\nu\beta\beta$ decay experiments and results (July 2018). (MJD = MAJORANA DEMONSTRATOR) Table from [14].

EX0-200 has also carried out searches for a number of exotic decays;

1. A search for instability of nucleons decay bound in ^{136}Xe nuclei was conducted using 223 kg·yr. This resulted in the most stringent limits to date for the nucleon decays to ^{133}Sb (3.3×10^{23}) and ^{133}Te (1.9×10^{23}) [63].

2. A search for the two-neutrino $\beta\beta$ decay of ^{136}Xe to the first 0^+ excited state of ^{136}Ba was conducted using 100 kg·yr exposure. Using a machine learning algorithm a lower limit of $T^{2\nu}_{1/2}(0^+ \rightarrow 0^+_1) > 6.9 \times 10^{23}$ yr at 90% CL was found. This result was found to be consistent with the estimated half-life of 2.5×10^{25} yr. Furthermore the half-life sensitivity was determined to be 1.7×10^{24} yr [65].

Chapter 4

Two-Neutrino and Neutrinoless Double Beta Decay of ^{134}Xe

EXO-200 has been in operation since 2011. In February 2014 an underground fire at WIPP caused the experiment to cease operations. The detector was recommissioned in December 2015 and data taking resumed in February 2016. All data acquired since the restart in 2016 are classified as Phase II data. Data acquired prior to February 2014 are classified as Phase I data. The search conducted in this thesis and described in sections 4.3 and 4.4— deals exclusively with the first year of the Phase II dataset. Some improvements were made to the detector between the phases and the analysis tools have also improved. Many analysis techniques from Phase I that apply to Phase II are also presented here.

The phase space for neutrinoless double-beta decay scales strongly with the Q-value [7, 9]. For this reason searches for the process has focused on isotopes with Q-values greater than 2 MeV. Experiments measure half-lives, which are linked to the phase space factor G and the nuclear transition matrix element. This nuclear matrix element (NME) is purely Gamov-Teller (GT) [9] in the case of $2\nu\beta\beta$.

$$\frac{1}{T_{1/2}^{2\nu}} = G \times |M_{GT}|^2. \tag{4.1}$$

As we mentioned in chapter 2 these NMEs are difficult to calculate. Since equation 4.1 does not contain any unknown from the particle physics point of view, measurements of $2\nu\beta\beta$ decay half-lives can provide crucial information about the NME. By comparing double beta emitters from the same element (separated by a difference of two neutrons in the same shell) the NME calculations can be well probed. This has been done for Te [66] where the half-lives of both ^{128}Te and ^{130}Te have been measured. Other candidate elements with 2 or 3 emitters include: ^{46,48}Ca, ^{80,82}Se, ^{94,96}Zr, ^{98,100}Mo, ^{114,116}Cd, ^{122,124}Sn, ^{134,136}Xe and ^{146,148,150}Nd. Unfortunately the Q^{11}-dependence of the phase space for $2\nu\beta\beta$-decay makes it difficult if not impossible to observe emitters (for the same element) with lower Q-value.

The double beta decay of ^{134}Xe into ^{134}Ba has a Q-value of 825.8 ± 0.9 keV [67] and its natural abundance is 10.4%. Despite the fact that the much higher Q-value of ^{136}Xe will cover a potential ^{134}Xe signal, careful analysis can nonetheless yield good sensitivity. The current limit on the $2\nu\beta\beta$-decay half-life is 8.7×10^{20} yrs set by EXO-200 with its Phase I dataset [13].

The aim of the present analysis was to calculate an improved limit for ^{134}Xe with the first year of the Phase II dataset and demonstrate that a significant improvement to the published values can be expected from the full dataset once it is available . This is possible because of the improved detector electronics and MC simulations. Furthermore, ^{85}Kr, the main background (aside from ^{136}Xe) is expected to have decayed enough to measurably reduce its impact on the main signals. A more complete ^{85}Kr analysis would include a combined analysis of the full Phase II and Phase I datasets. Here we only focused on the first year of Phase II, which is what was available at the time of writing this thesis.

4.1 General data analysis strategy

The primary backgrounds to ^{136}Xe $2\nu\beta\beta$ (Q = 2457.8 keV) in EXO-200 are gamma and beta interactions due to trace quantities of ^{40}K, ^{232}Th, and ^{238}U in the detector materials. These same backgrounds apply for the ^{134}Xe $2\nu\beta\beta$ (Q = 825.8 keV) but more prevalent at these low energies are β's from ^{85}Kr (with end point at 687.4 keV) and 661.7 keV γ's from ^{137}Cs. We separate these backgrounds from $2\nu\beta\beta$ candidates by taking advantage of the detector's good energy and position resolution and its ability to perform pattern recognition. First, we label an event as being "single-site" (SS) if it is consistent with having all charge deposits confined to a single volume with a characteristic dimension of ∼2-3 mm, as expected for most $2\nu\beta\beta$ events in LXe. Otherwise the event is labeled as "multi-site" (MS). Secondly, we calculate for each event the "standoff distance", or the shortest distance between the various charge depositions to an anode wire or reflector surface. Gamma events and $2\nu\beta\beta$ events have distinguishable standoff probability distributions because the latter are uniformly distributed in the LXe whereas the former tend to originate in the passive detector materials and exhibit some attenuation in a detector of the size of EXO-200. Third, we measure the total energy of each event by combining the charge and scintillation signals in a manner which takes advantage of the anti-correlation between these channels to improve the energy resolution [48]. This last procedure is essential for the search for ^{136}Xe $0\nu\beta\beta$, where the signal is a resolution-limited feature at the Q-value, but is also utilized in the measurement of the $2\nu\beta\beta$ decay. While resolution is not as crucial for the present analysis it is nonetheless optimized. These steps are described in more details in section 4.2

We exploit these three variables by selecting fiducial β-like events in the data, dividing them into the SS and MS categories, and performing a simultaneous maximum likelihood fit to the energy spectra and standoff distance of both event samples. The probability distribution functions (PDFs) provided to the fit are determined by a Monte Carlo simulation of the relevant signal and background sources. This strategy is validated by comparing data and simulation for calibration sources. The efficiency of the event selection for $2\nu\beta\beta$ events is determined by a combination of data and Monte Carlo studies and is cross-checked by the external calibration source data. These steps are described in more details in section 4.3.

4.2 Data and simulations

The data acquisition system (DAQ) for EXO-200 was described in chapter 3. We summarize it again here. Then we will briefly outline the data processing steps before giving a detailed description of the event reconstruction process. We will also briefly discuss how we use Monte Carlo simulations to understand the detector.

4.2.1 Data collection and processing

EXO-200 collects data from the TPC using a DAQ system composed of 226 hardware channels (76 U-wire signals, 76 V-wire signals, and 74 APD gang signals), muon veto panel output, and a high-voltage (HV) glitch detector. All the hardware channels are coupled to the front-end electronics system where the data is passed into the Trigger Electronics Module (TEM). The TEM also records output from the veto system and glitch detector. The TEM records data based on pre-determined trigger conditions. When a triggering condition is met, waveforms from all channels are recorded by the TEM, with a window of 1024 μs before and after the triggering time (so all recorded waveforms are 2048 μs long). When a veto or glitch detector trigger is met, that information is timestamped, recorded to disk, and later synchronized with the TPC data. The four main TPC trigger conditions are:

1. Individual U-wire trigger for γ and β events in LXe. Those thresholds are $\sim$ 100 keV in size.
2. Trigger on the summed APD waveform for α events ($\sim$ 25 000 photons) in LXe.
3. Solicited (forced) trigger at 0.1 Hz, for monitoring detector performance.

The TPC triggers at an average rate of 0.2 Hz during a nominal low-background data taking. The event rate jumps to about 35 Hz during source calibration runs. Physical hard disks containing the waveforms are shipped from WIPP to SLAC National Accelerator Laboratory where they are copied to permanent storage disk before they can be carefully analyzed.

Once the data are at SLAC, they are processed in multiple stages before they are ready for physics analyses [11]:

1. ”rootification”: conversion of binary data files to ROOT files; low-level verification of data validity.
2. ”Reconstruction”: noise and muon events are tagged and waveform characteristics are calculated.
3. ”Processing”: this is the final reconstruction stage where events are clustered and data corrections (gain, grid efficiency, purity) are applied.
4. ”Trending”: extraction of parameters (e.g. noise threshold) useful for tracking detector trends over time.

After this processing is complete the data can be further processed by individual analysis groups into specific optimized data sets suitable for their work.

4.2.2 Reconstruction

The goal of the reconstruction step is to define LXe events' topology, i.e. energy and position. This is accomplished by finding signals in stored channel waveforms, estimating the parameters of these signals, and clustering (or grouping) based on their energy and position.

Event topology

Events in the EXO-200 TPC are classified as either single site (SS) or multi-site (MS) (see figure 4.1). This classification is motivated by the topology of events. γ rays in the TPC are likely to scatter off and deposit energy at several interaction sites, hence they are MS. In addition to the fact that ~ 2.5 MeV γs have a characteristic attenuation length (traveled distance before first interaction) of 8 cm they also tend to primarily Compton scatter in the 15-3500 keV range. (Below 15keV the primary interaction for γs is photoelectric absorption and above 3.5 MeV it is pair production). For this reason EXO-200 was designed in such a way that the wire grid has a 9 mm

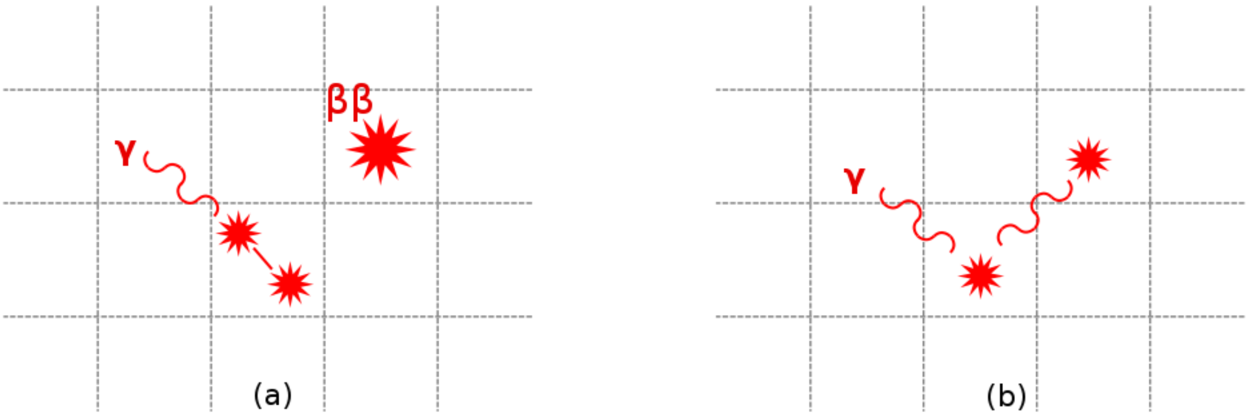

Figure 4.1: Illustration of the SS (a) and MS (b) event topologies for a gamma(γ) and aa double-beta ($\beta\beta$) decay event, projected onto wire grid.

position resolution; this ensures that charge clusters with a separation greater than $\sim$ 1 cm can be individually distinguished in the x and y directions. On the other hand ”β-like” events will be more localized. This is because electrons are greatly attenuated in LXe through collisional energy losses. Monte Carlo simulations have confirmed that double-beta decay events are approximately 90% SS.

Signal finding

Signal on waveforms do not always arrive at the same time (e.g. specified by trigger).We thus need to search for them and we do this using two separate methods: (a) we can apply a matched filter or (b) we can ”unshape” the waveform by identifying pulses closely following one another within a signal found by the matched filter.

The matched filter algorithm has been shown to produce stable performance over time in varying noise conditions [68]. We apply it in Fourier space:

$$y(t) = F^{-1}X(f)H^{*}(f) \tag{4.2}$$

where y(t) is the filtered signal, F is the discrete Fourier transform (FT), $X(f)$ is the FT of the original waveform, $x(t)$, and $H^{*}(f)$ is the complex conjugate of the FT of the transfer function,

$h(t)$, for the particular channel. For the APD channel equation 4.2 is further divided by the noise spectrum of the channels to whiten the spectrum.

U- and V- channels are filtered by applying a template model defined for each respective channel. In contrast, for the APD channels, we first sum the waverforms from all channels for each APD plane; the two resulting waveforms are then filtered with equation 4.2. After this, a peak-search algorithm is performed on the filtered waveform looking for amplitudes above a certain threshold, which is calculated for each waveform on an event by event basis to reduce the sensitivity to channel and time based noise variations. Effectively, if we assume normally distributed deviations from the baseline, the peak-search algorithm removes values greater than 3σ. Figure 4.2 shows an example of this procedure.

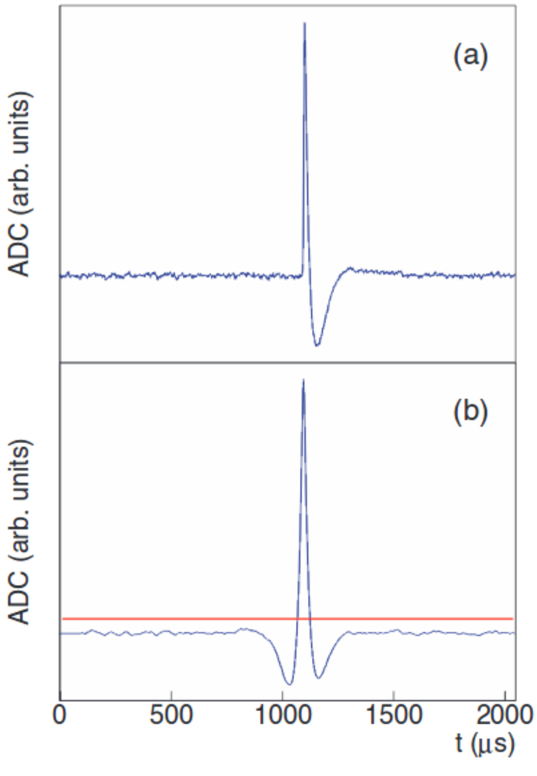

Figure 4.2: A U-wire waveform (a) and the result of the matched filter (b). The horizontal line in (b) is the calculated threshold.[11].

The matched filter is robust at finding signals but it does not always succeed in finding signals that are close in time. For this reason, a second algorithm is applied to the original waveform after the signals have been identified by the matched filter. The algorithm ”unshapes” the signal, obtaining the original charge deposited $q(t)$:

$$q(t) = F^{-1}H^{-1}(f)X(f) \tag{4.3}$$

where $H^{-1}(f)$ is the inverse transfer function. $q(t)$ is then reshaped with a 2-μs triangular, or moving average filter. And finally a peak-search algorithm is applied to determine the presence of any additional signal.

Parameter estimation of signals

To determine the amplitude and time of signals we fit them. The cost function χ^2 is constructed as:

$$\chi^2 = \sum_{l=0}^{L} \frac{[x_i - b - \sum_{i=0}^{N}(A_i f_{SM}(x_l, t_i))]^2}{\sigma^2_{noise}} \tag{4.4}$$

where x_i is the value of the waveform sampled at time l, b is the baseline voltage of the waveform, σ_{noise} is the RMS noise of the waveform, i is the index of the *i-th* signal (out of N) found on the waveform, A_i is the amplitude of the *i-th* signal, f_{SM} is the signal model (constructed from the channel transfer function), and t_i is the time of the *i-th* signal. χ^2 is numerically minimized using MIGRAD algorithm from ROOT. An example of these fits is shown in figure 4.3. Sometimes charges can drift close enough to a U-wire and induce a signal on that channel without actually depositing charge on it. This is a problem because some SS events might then be mistakenly classified as MS and this would result in an erroneous accounting of possible $0\nu\beta\beta$ candidates. To identify and flag these U-wire induction signals, the following discrimination criteria are applied:

1. Pulse timing: the risetime of the pulse is defined as the time between 10% of pulse height and 90% of pulse height. The time from pulse maximum to minimum of following pulse is defined using similar thresholds of 90% and 10%.

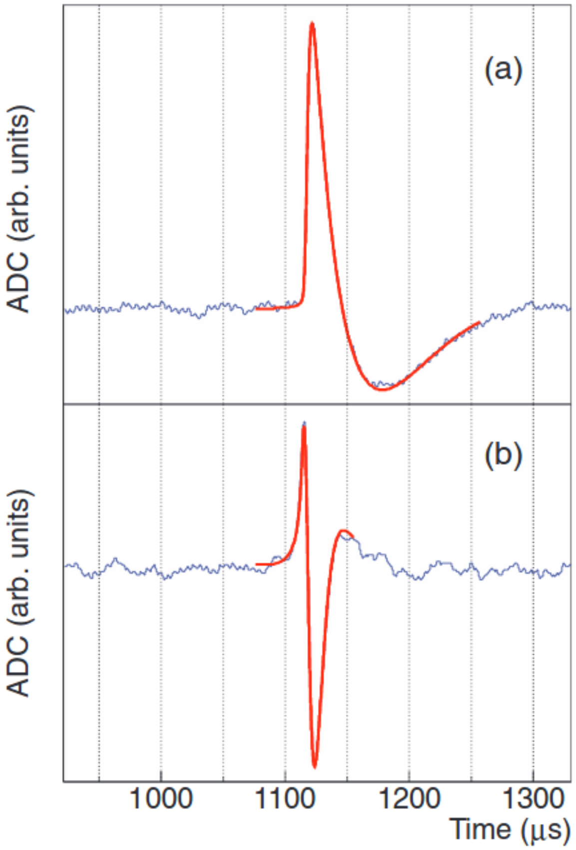

Figure 4.3: Examples of fits to a U-wire (a) and V-wire (b) on an expanded vertical scale. One can see that the V-wire peaks earlier than the U-wire signal.[11].

2. Pulse integral: integral of pulse is calculated in a time window around the peak, defined as $t_{peak} - 10\mu s$ to $t_{peak} + 40\mu s$.
3. Fit χ^2: U-wire signal is fitted according to the procedure highlighted earlier. χ^2 is then calculated in a window restricted to 20 μs before and 30 μs after the peak.
4. Nearest-neighbor amplitude: total energy on neighboring channels signals close in time.

Figure 4.4 shows the distributions of these discriminators for simulated induction and collection U wire signals.

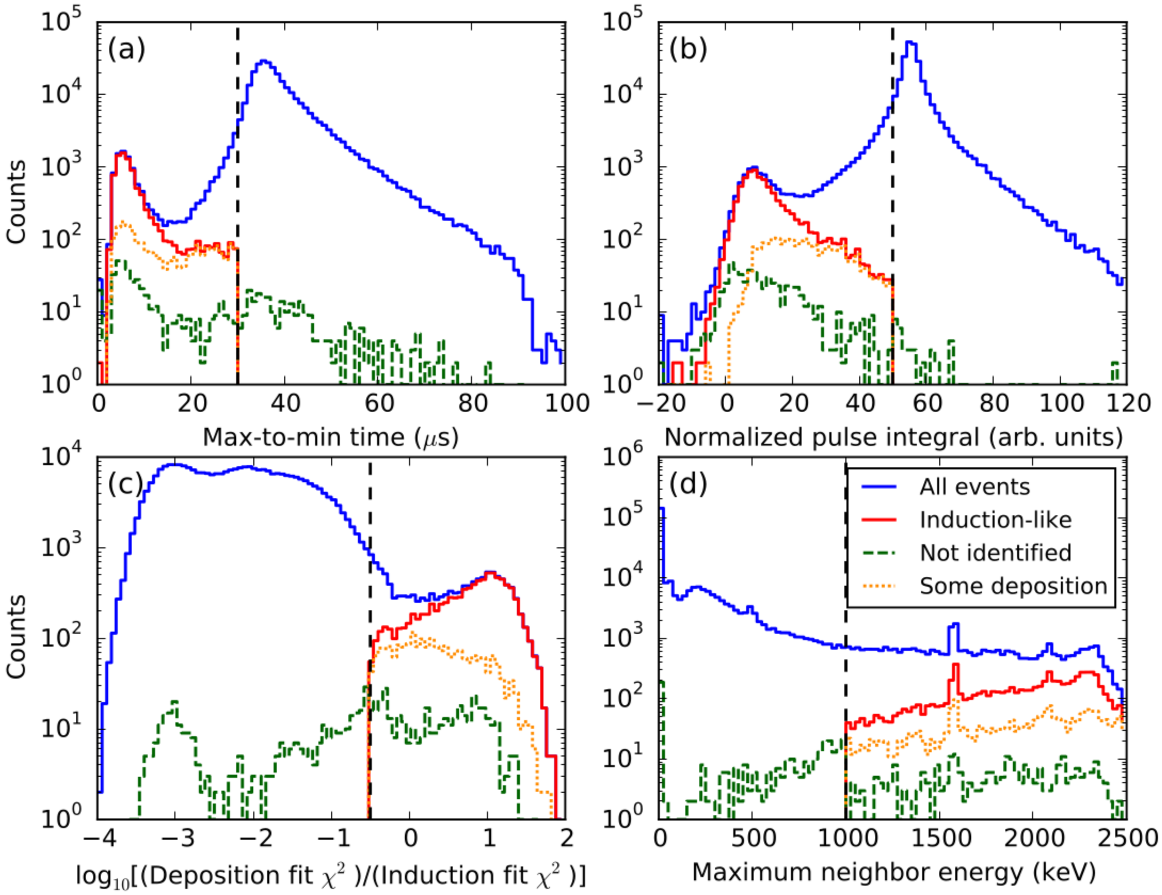

Figure 4.4: Distributions of the discriminants used to identify induction signals, calculated for waveforms generated from ^{228}Th Monte Carlo simulations. The distribution of these values for all U-wire signals is shown as the solid histogram, with the cuts used for each value denoted by the vertical dashed lines. U-wire signals must satisfy all cuts to be identified as "induction-like" signals. Also shown are the distributions of simulated induction pulses which were not identified as induction-like by the cuts ("Not identified") and simulated pulses containing at least some deposition, but which were identified as induction-like ("Some deposition").[11].

Clustering

Once the time and amplitude of signals on U, V, and APD channels have been found, these signals are grouped together to form 3D charge clusters. We first bundle U-wires by grouping signals on adjacent channels arriving within 3.5 μs of each other; the time of the bundle is calculated as the energy-weighted average time of the U-wire signals that make up the bundle. Then V-wire signals are bundled according to time using:

$$|t_i - t_0 - (2.97\ \mu s/chan)\Delta V| \leq 4.5\ \mu s \tag{4.5}$$

where t_0 is defined by the V channel with the largest amplitude, t_i is determined from V channel of interest, and ΔV is defined as the absolute channel number difference of the two signals. This means that 'outer' signals are expected to arrive earlier than the 'central' (or largest-energy-) V-signal and that the amount of time that they arrive earlier grows (roughly) linearly with the number of channels between the signal and the central signal. The time of the V wire bundle is the time of the largest V-wire signal; this is done because doing a time average was shown to dilute the time-correlation between U-wire and V-wire bundles.

To calculate the Z-position of a U-wire bundle, a corresponding scintillation cluster is found. This is done in a very simple way: From all scintillation clusters that occurred between 3 μs after and maxDriftTime + 3 μs before the U-wire bundle, the one scintillation cluster with the smallest absolute time difference from the U-wire bundle is picked (maxDriftTime is given by the drift velocity and the distance between Cathode and U-wire plane). If no scintillation cluster lies in that time range, the Z position is set to -999.0 mm.

The clustering has probability density functions (pdfs) that model how likely it is that a U-bundle belongs to a V- bundle. At the moment there are three pdfs. One for the time difference between U- and V-bundles, one for how well the sum of signal amplitudes in the U-bundle compares to the sum of signal amplitudes in the V-bundle, and one that models whether the resulting (U,V) coordinate is physical at all. The negative log of the product of the three pdfs (the 'cost') is used as a measure of how well a U-bundle matches a V-bundle. The lower the cost, the better they match. A matching is a set of 1-to-1 connections between U-bundles and V-bundles. The best matching is the one whose sum of costs is minimal (the sum runs over all connections in the matching). Once the best matching is found, a charge cluster is created for each of the connections in the matching and the U- and V- positions of the charge cluster can be set.

4.2.3 Corrections

APD light map

The amount of scintillation light collected by the APDs depends on the location of the energy deposition. This variation is caused by differences in the solid angle covered by the APDs and by their gain differences. 3-D correction functions are used to account for this position dependence. Such correction functions are generated from ^{228}Th calibration runs with the source placed at the two anodes and three positions around the cathode plane. The detector volume is divided into 1352 spatial voxels (13 radial bins, 8 azimuthal bins, and 13 Z bins). The bin widths are chosen to ensure adequate statistics, and to optimally map the response in the regions with a high light collection gradient.

Electron lifetime correction

As mentioned earlier electrons can attach to impurities as they drift, resulting in a loss of charges. The number of electrons is given by:

$$N_e(t) = N_0 e^{-t/\tau} \tag{4.6}$$

where N_0 is the initial number of electrons and τ_e is the electron lifetime, defined as the time it takes for the number of electrons to decay by 1/e.

The electron lifetime varies over time due to small changes in the xenon recirculation rate, occasional interruptions due to xenon pump maintenance or failure and power outages, and events where xenon gas is added to the detector by the detector monitoring system. To account for this a correction factor of exp(t/τ_e) is applied to all ionization signals in the data by evaluating the τ_e history function at the time of each event.

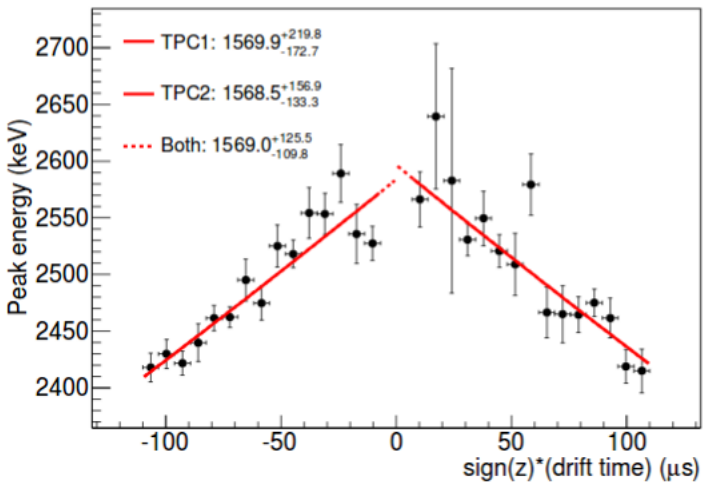

Figure 4.5: An example electron lifetime τ_e measurement obtained by fitting a decaying exponential to the ^{228}Th full-absorption peak energies binned by drift time. TPC 2 (negative Z) is assigned a negative drift time for convenience in visualization. Fits to separate τ_e for each TPC and the combined fit value are shown. This data is from a single source calibration run.[11].

Shielding inefficiency correction

The presence of V-wires is supposed to shield U-wires for ”seeing” a drifting charge. However this shielding is well known to not be 100% effective and as a result the U-wire signal amplitude will always contain some small induction, which is manifested by a dependence on the initial position of the drifting charge; this is common to all ionization chambers [69]. The Shockley-Ramo theorem [70] tells us that the induced charge on the U-wires from a charge q moving from $\mathbf{z}_0$ to $\mathbf{z}$ is given by $q(\phi(z)-\phi(z_0))$, where ϕ is the weighting potential for the particular U-wire. For the V-wires to fully shield the U-wires from the drift region, $\phi(z)$ would have to be 0 throughout the entire drift region.

We measure this effect in the data by fitting the purity-corrected peak-position of the ^{208}Tl gamma line at 2615 keV as a function of the z-coordinate of the energy deposit. The fit function is given by:

$$E_{means} = E_0 \frac{1}{1 + p_0 e^{(|z|-192.5)/p_1}} \tag{4.7}$$

where E_{means} is the purity corrected peak energy, E_0 is the true peak energy, and $z_{max} = 192.5$ mm is the maximum drift distance. The calculated best fit parameters are (p_0, p_1) = (0.043,7.02

mm) and (0.064, 8.09 mm) for one-wire and two-wire charge deposits respectively. The function is then inverted to correct the measured charge deposit energy to the true energy. This correction is typically less than 1% for events in the fiducial volume.

Rotated energy

As already mentioned, EXO-200 takes advantage of the anti-correlation between the ionization and scintillation signals to optimize the energy resolution near the ROI for ^{136}Xe $0\nu\beta\beta$. The energy resolution $\sigma(E)$ is parametrized by:

$$\sigma^2(E) = \sigma^2_{elec} + r_1 E + r_2 E^2 \tag{4.8}$$

where σ_{elec} is the electronic noise, $r_1 E$ represents statistical fluctuations in the ionization and scintillation, and $r_2 E^2$ represents position- and time-dependent changes in the gain. These resolution parameters are used to smear the true energy in Monte Carlo simulations and must be calculated accurately. The optimal energy variable figure 4.6 is calculated by combining the charge E_I and scintillation E_S according to

$$E_R = E_S \sin(\theta^R) + E_I \cos(\theta^R) \tag{4.9}$$

where E_R is the 'rotated' energy and θ^R is the rotation angle.

4.2.4 Monte Carlo

Sophisticated numerical simulations to better understand the detector have been carried out. These simulations are important as the detector responses they predict can be compared to actual measurements. I will not discuss the details of these simulations as they are beyond the scope of this thesis. In brief: EXO-200 uses GEANT4 to simulate radiation in particle interactions inside the detector. The generation of simulated events uses a Monte Carlo method of pseudorandom number generation to randomly sample the probability density functions describing the particular decay process being

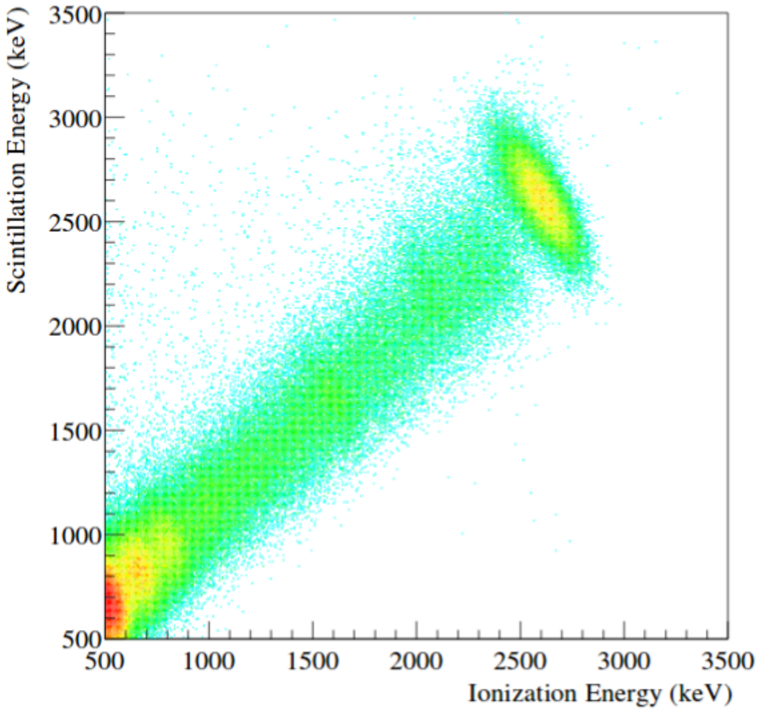

Figure 4.6: Anti-correlation between ionization and scintillation for SS events from a ^{228}Th source. The prominent island at the upper end of the distribution is the 2615 keV gamma line of ^{208}Tl.[11].

modeled. Ultimately, the Monte Carlo simulations give us the shapes of the probability density functions, parameterized by the energy and standoff distance, for all the possible radioactive decays that are expected to occur in EXO-200. The specific pdfs will be discussed in section 4.3. Figure 4.7 shows the detector geometry used in the simulations.

4.3 Physics analysis

4.3.1 Monte Carlo validation

The success of EXO-200 depends on its ability to reconcile measured/observed quantities with expected behavior as modeled by MC simulations which capture how well the detector is understood. Three important improvements were made to the MC for this analysis, relative to those previously published (before June 2016) EXO-200 analyses:

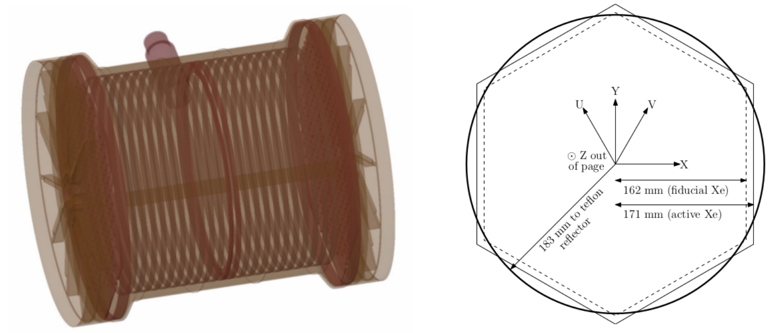

Figure 4.7: (Left) Simplified model of the EXO-200 TPC used in the GEANT4 Monte Carlo simulations. Visible on the left is the copper LXe vessel with the field cage rings inside and the high voltage feedthrough port on the top middle. (Right) the TPC coor- dinate system. LXe lying within the hexagonal apothem defined by the outermost wire is called the active LXe, while LXe outside this apothem is the inactive LXe. The U and V-wire coordinates are transformed into x and y coordinates on perpendicular axes. The z direction is oriented out of the page.[11].

1. The upgraded electronics had the effect of minimizing the APD read-out noise observed in Phase I and the result of this was a lower light detection threshold and a better energy resolution. A more realistic light map reflecting this was thus included in the MC for this analysis.
2. The transverse diffusion of electrons is now included in the MC, following EXO-200's measurement of this effect [71, 13].
3. Charge collection is exponentially attenuated with drifting distance before the simulation of pulse shapes. This is because impurities can capture drifting electrons. An average electron lifetime of $\tau \sim 4.5$ ms was included in the simulation.

MC simulations are validated through a process known as source agreement whereby the MC predictions are compared to actual data from source calibration runs for a variety of different metrics. The process of validating can be split into two main areas: shape agreement (agreement of variable distributions normalized to number of counts), single site fraction agreement pf SS classification, and rate agreement. While validation is generally performed for each dedicated analysis some of the details presented below may have been carried for other analyses but are included here because they are still valid.

Shape agreement

Shape agreement is the first validation we ran for this analysis. It consists in comparing the shapes obtained from MC to that measured for source runs. Good agreement has been demonstrated for the standard ^{136}Xe analyses in the $\geq$ 1 MeV range. However the low Q-value for this analysis required a substantially lower threshold. Improvements to the MC mentioned above produced an agreement between data and MC better than 10% for energies above 300 keV. This is a substantial improvement from a previous analysis of Phase I data which could only achieve 10% or better agreement for energies above 600 keV. Plots of the shape agreements for different sources are shown in figure 4.8

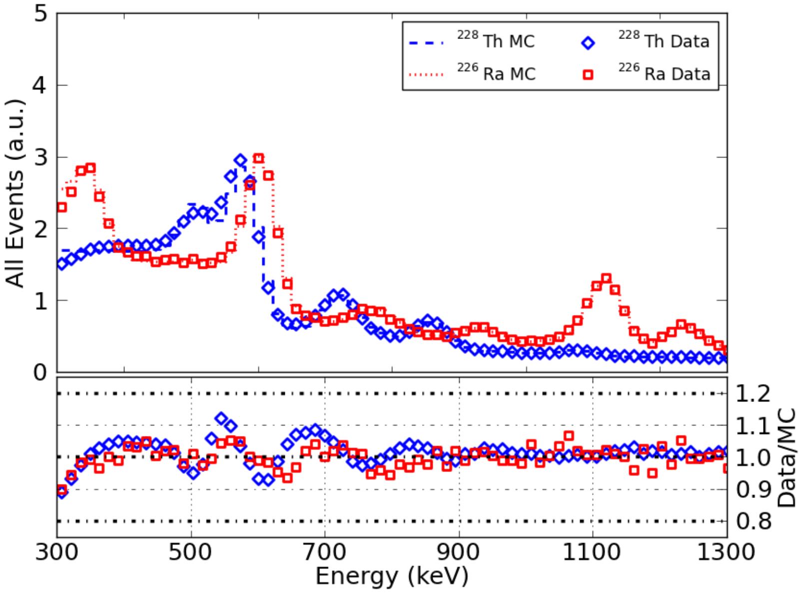

Figure 4.8: shape agreement for Phase II dataset. The lower panel shows the residual between data and MC.

SS fraction agreement

The single site (SS) fraction is defined as the ratio of number of events that are single site to the total number of events that are either single site or multi site, i.e SS/(SS+MS). The difference in SS fractions between data and MC will be used to constrain the error of the SS fraction of components used in the low-background fit model. Figure 4.10 shows the SS fraction agreement.

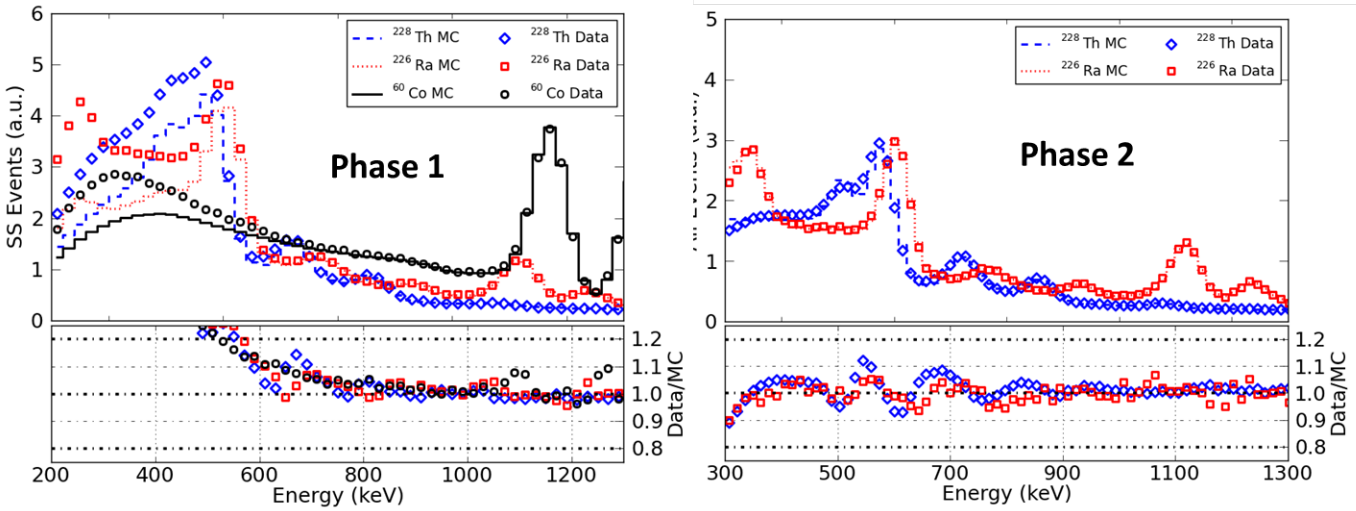

Figure 4.9: shape agreement. Clear improvement in Phase II compared to Phase 1.

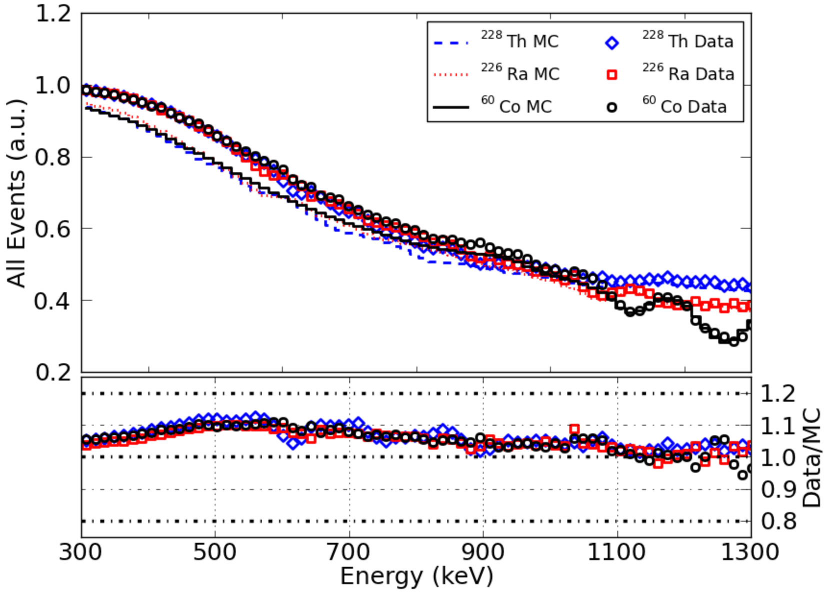

Figure 4.10: SS fraction agreement. The lower panel shows the residuals between data and MC.

4.3.2 Fiducial volume and event selection

The fiducial volume (FV) is defined as the region inside the detector within which all events considered for analysis are located. In particular it requires that the position of all charge deposits making up an event be reconstructed within the defined volume. In choosing a fiducial volume we strive to maximize the mass ^{134}Xe (or ^{136}Xe since the mixing is uniform) to ensure we get the best sensitivity. However we must also limit ourselves to a physical region of the TPC that is well modeled so that systematic uncertainties may be minimized.

The FV is defined by a set of cuts on the coordinates of events. Several fiducial volumes have been considered for the many different analyses EXO-200 has run. In general there is very good energy shape agreement between MC and data for all sources, for all fiducial volumes, but there are few noticeable effects on the energy spectra when the fiducial volume is increased. I will not discuss these details as they have presented and published in other analyses [11]. The FV chosen for this analysis is defined as follows

1. All evens must be more than 10 mm from the anode and cathode planes as well as from the cylindrical PTFE reflector covering he side of the TPC, i.e. 10 mm $<|z|<$182 mm.

2. The events must lie within a hexagon with apothem of 162 mm (see figure 4.7).

This choice of fiducial volume corresponds to 94.8 kg of total xenon. With 19.1% of it being ^{134}Xe, we get a fiducial mass of 18.1 kg (of ^{134}Xe) for this analysis, i.e. $8.14 \cdot 10^{25}$ atoms.

4.3.3 Fit Model

We fit the SS and MS samples separately but simultaneously with binning in energy and and standoff distance by constructing a negative log likelihood (NLL) function between data and MC:

$$NLL = -\ell(\theta; x) = -\log L(\theta; x) = -\log f(x; \theta) \tag{4.10}$$

where $L(\theta; x)$ is the likelihood function defined by f, the joint probability distribution function (over all bins) for observed the data described by the set of parameters θ. Let's assume the probability of observing k_i decays in a given amount of time t is Poisson distributed:

$$f(x; \theta) = \prod_{i=1}^{N} f(x = k_i; \theta) = \prod_{i=1}^{N} \frac{\mu_i^{k_i} e^{-\mu_i}}{k_i!} \tag{4.11}$$

where μ_i is the expected number of decays in the *i-th* bin from MC simulations. We can then write:

$$\begin{aligned} NLL &= -\log\prod_{i=1}^{N}\frac{\mu_i^{k_i}e^{-\mu_i}}{k_i!} \\ &= -\sum_{i=1}^{N}\log\frac{\mu_i^{k_i}e^{-\mu_i}}{k_i!} \\ &= -\sum_{i=1}^{N}\Big[\log(\mu_i^{k_i}e^{-\mu_i}) - \log(k_i!)\Big] \\ &\approx -\sum_{i=1}^{N}\Big[\log\mu_i^{k_i} + \log e^{-\mu_i}\Big] \\ &\approx \sum_{i=1}^{N}[-k_i\log\mu_i + \mu_i], \end{aligned} \tag{4.12}$$

where we've dropped the $\log(k_i!)$ term since it is independent of the model parameters and contribute only a fixed additive offset to the NLL value. During the fit each model parameter is given a Gaussian constraint G$_{constr.}(\theta)$. These constraints are determined by carefully studying he systematic errors that affect each parameter. Furthermore equation 4.12 is independently valid for SS and MS fits. We can thus write the total NLL as:

$$\begin{aligned} NLL &= NLL^{SS} + NLL^{MS} + \sum_j G_{constr.}(\theta_j) \\ &= \sum_{i=1}^{N}[(\mu_i^{SS} + \mu_i^{MS}) - (k_i^{SS}\log\mu_i^{SS} + k_i^{MS}\log\mu_i^{MS})] + G_{constr.}(\theta) \end{aligned} \tag{4.13}$$

The three main parameters for the low-background fit (specific to each component) are: (i) the SS fraction, (ii) the number of decays, and (iii) the overall normalization constant that incorporates errors on event detection efficiency. For this analysis the following components (PDFs obtained from MC) are included:

1. ^{85}Kr dissolved in the LXe, producing β decays with end point at 687.4 keV. This is a critical background for ^{134}Xe double beta decay searches. It will be discussed in details later. The simulated energy spectrum of ^{85}Kr includes the two β-decay modes with branching ratios of 99.56% and 0.44% to the ground and excited states of ^{85}Rb, respectively. The latter is

followed by the release of a 514 keV γ-ray.

2. ^{137}Cs in the materials near the LXe.
3. $2\nu\beta\beta$ ^{136}Xe.
4. ^{238}U, ^{232}Th, ^{40}K.
5. Gamma rays from neutron capture on ^{1}H in the HFE, and ^{63}Cu ^{65}Cu in the TPC vessel and cryostats.
6. ^{222}Rn, ^{137}Xe, ^{135}Xe: backgrounds in the LXe.
7. ^{65}Zn, ^{60}Co, ^{54}Mn: activated by-products in the copper TPC vessel from neutron capture on the corresponding stable isotopes.

Constrained parameters are incorporated by multiplying the likelihood function by the corresponding probability distribution functions for the parameter value. This means that if the constraint is Gaussian-distributed all we need to do is multiply the likelihood by a Gaussian PDF. These constraints are useful as they help limit the available parameter space during a fit. For a single uncorrelated parameter θ_i in θ, $G_{constr.}$ contributes:

$$\frac{1}{2}(\frac{\theta_n - \theta_{n,0}}{\sigma_n})^2 \tag{4.14}$$

to the total NLL, where σ_n is the standard deviation and $\theta_{0,n}$ is the expected value of the n-th parameter θ_n. In general, the number of parameters is not equal to the number of fit components; the low-background models typically have ~ 45 parameters and are quite complex.

The specific parameter constraints for this analysis are (i) ^{222}Rn dissolved in LXe as a function of time 20%, (ii) the SS fractions for all components in the low-background data as determined by the error (see next section) found to be 5.23%, and the overall normalization factor (see next section) 6.2% (calculated for analysis in [13]).

4.3.4 Systematic errors

There are a number of separate factors that contribute to systematic error on the measurement of the number of decays for each fit component. These include but are not limited to: event selection criteria, inadequacies in the Monte Carlo simulations, and issues with the DAQ system. To account for these, five Gaussian constraints are added to the minimization function:

1. uncertainty in the activity of radon in LXe;
2. uncertainty in the relative fractions of neutron capture related PDF component;
3. uncertainty in SS fraction;
4. uncertainty in the overall signal detection efficiency caused by imperfections in the MC model;
5. uncertainty in signal pdf shape, also called signal-specific normalization, which arises from differences between data and MC.

The first two are determined from external studies and were briefly discussed in the previous section on the Fit Model. The uncertainty in SS fractions is evaluated using calibration data and is defined as the weighted average of the the SS fractions residuals ((data-MC)/data) with weights based on the signal spectrum and detector livetime.

Overall normalization term

This is also known as the signal detection efficiency. Imperfections in the MC model, common to all components, result in a difference of counts between data and MC. We account for these by aggregating them into a single additional degree of freedom N in the fit which scales each fit component equally. This normalization factor is constrained to unity within the estimated systematic error and the largest contributions to it arise from the event selection criteria and FV cuts. For this analysis the fiducial volume is the same as that used in [63]. The corresponding overall normalization error was determined to be 3.6%.

Signal normalization error

Shape discrepancies between data and MC are propagated into the signal rate through a normalization parameter that only scales the coefficient of the signal PDFs, in this case ^{134}Xe $2\nu\beta\beta$ and $0\nu\beta\beta$. This normalization parameter is also referred to as the shape error N$_s$. This factor N$_s$ is freely floated with an expected value of 1 and error σ_s. We determine σ_s by performing toy MC studies to find out how the measured number of decays is systematically affected by the "skewed" PDF shapes. Skewed PDFs refer to the PDFs obtained from MC and used in the fit as described above; they are labeled "skewed" because their shapes do not perfectly agree with those measured from source runs. The "unskewing" procedure is as follows:

1. From the best fit model construct a set of corresponding "unskewed" PDFs where each PDF$_j$ is corrected to match the shapes of the energy and standoff distance distributions seen in source calibration runs. A PDF is unskewed/corrected by multiplying it with a bin-dependent correction factor. In other word the ith bin of PDF$_{skewed}$ is multiplied by $C(E_i, r_{SD,i})$ to obtain the ith bin of PDF$_{unskewed}$ where E_i is the energy of bin i and $r_{SD,i}$ is the standoff distance. The correction factor is defined as

   $$C(E_i, r_{SD,i}) = \frac{1}{1 - f(E_i)} \frac{1}{1 - g(r_{SD,i})} \tag{4.15}$$

   with

   $$\begin{aligned} f(E) &= p_0 + p_1 E \\ g(r_{SD}) &= q_0 + q_1 r_{SD} \end{aligned} \tag{4.16}$$

   f and g are correction functions defined from the observed shape deviations between Monte Carlo simulations and source calibration data. Separate correction functions are applied to SS and MS. Moreover separate correction functions for the energy are derived: one for ^{60}Co and applied to Co-like backgrounds (^{60}Co); one for ^{228}Th and applied to Th-like backgrounds; one for ^{226}Ra and applied to Ra-like backgrounds (^{238}U for instance). For β-like components (mainly the signal) the correction function is derived by: (i) subtracting the best-fit model excluding the $2\nu\beta\beta$ ^{136}Xe from the low-background data; (ii) subtracting the best fit $2\nu\beta\beta$ ^{136}Xe from the background subtracted data in (i); and (iii) taking the ratio of (i) and (ii) and fitting a line to the observed energy dependence.

2. Create a toy MC dataset by randomly sampling the unskewwd PDFs a large number of times.
3. Fit the toy dataset with the original, skewed PDFs and extract the number of signal decays.
4. Take the number of signal decays from the toy dataset and compare it to the number of decays from the original best-fit model. Compute relative difference between the two.

This process was repeated 10k times, i.e 10k toy data sets were built and fitted so a distribution of the relative difference could be built. The median of the distribution is then used as the systematic error σ_s. σ_s is included into the low-background fit as constraint by adding the following coefficient to the overall NLL:

$$\frac{1}{2}\Big(\frac{N_s - 1}{\sigma_s}\Big)^2 \tag{4.17}$$

For this analysis we first checked the reliability of the toy MC generation. This is done by generating toy MCs modeled from the "skewed" PDFs and scanning the number of $2\nu\beta\beta$ input into the model. The idea is that if our toy Monte Carlo generation is representative of the real data then the toy MC should output (after fitting) a $2\nu\beta\beta$ count similar to the input (user set) number. Similar studies were carried for other analyses and the toy MCs were found to be reliable. Figure 4.11 shows the results from this study. The median number of $2\nu\beta\beta$ output by the model is consistently below the input by about 10.5%. This is an additional systematic error we'll include in the shape error.

The next step involves generating toy MCs modeled after the "unskewed" PDFs as described above. A similar $2\nu\beta\beta$ input scan is performed. Results from this are shown in figure 4.12, where both the median and the mean output values for each 2.5k toy MC set are shown. These results are also shown in tables 4.1 and 4.2. The difference between skewed and unskewed toys relative to the true (best fit) input is the shape error.

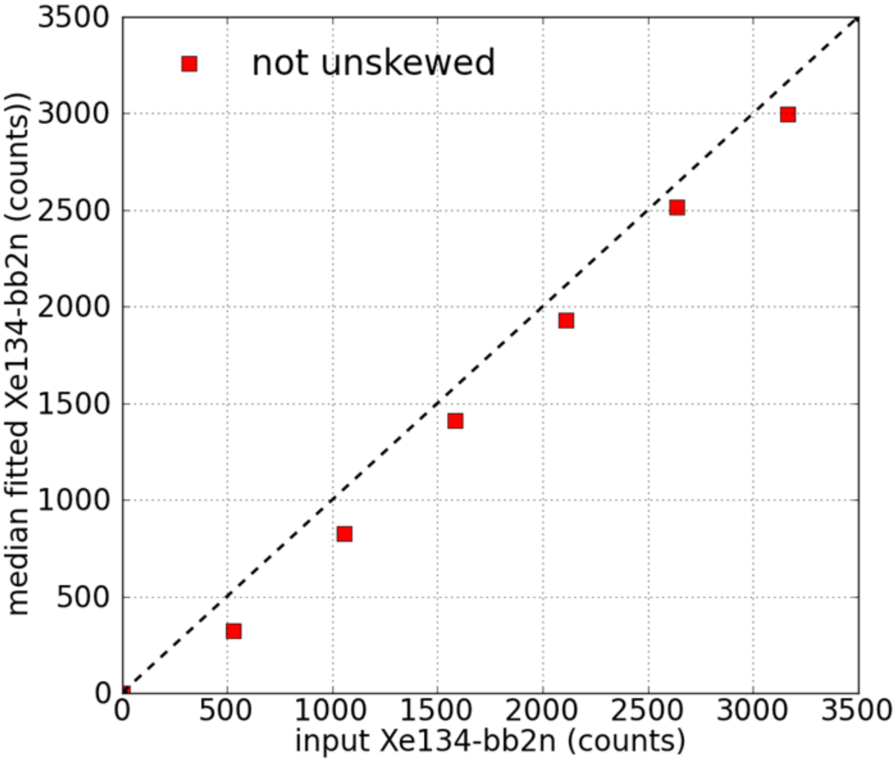

Figure 4.11: Toy MC study. The number of calculated events from toy data set is consistently below the number of events from best fit.

Input	unskewed	skewed	difference	difference/input
564.8	302.7	440.2	137.5	0.243
753.0	464.2	701.6	237.4	0.314
847.2	570.5	823.4	252.9	0.299
941.3	646.9	978.1	331.2	0.352
1035.4	729.7	1117.1	387.4	0.374
1129.6	826.7	1204.9	378.2	0.335

Table 4.1: Median output values for skewed and unskewed PDFs as the the input number is varied. The best fit value was found to $num\_bb2n\_Xe134 = 941.3$ counts.

Using the average difference for the means we get 260 counts and the shape error is estimated to be $\sigma_s = 260/941.3 = 27\%$. The pulls on the input values are greater than expected and do not agree with previous studies. Further study is warranted. We think the shape error reported here is thus a conservative value and is comparable to that from Phase I (25%) [63]. It should be emphasized that this error grows as the energy threshold is lowered. This is because the detector is not well understood at low energies and so the shape agreement are generally poor.

Input	unskewed	skewed	difference	difference/input
564.8	482.7	667.6	184.9	0.327
753.0	607.3	822.7	215.4	0.286
847.2	683.1	920.7	237.6	0.280
941.3	744.9	1050.9	306.0	0.325
1035.4	819.3	1121.7	302.4	0.292
1129.6	909.1	1225.7	316.6	0.280

Table 4.2: Mean output values for skewed and unskewed PDFs as the the input number is varied. The best fit value was found to $num_bb2n_Xe134 = 941.3$ counts.

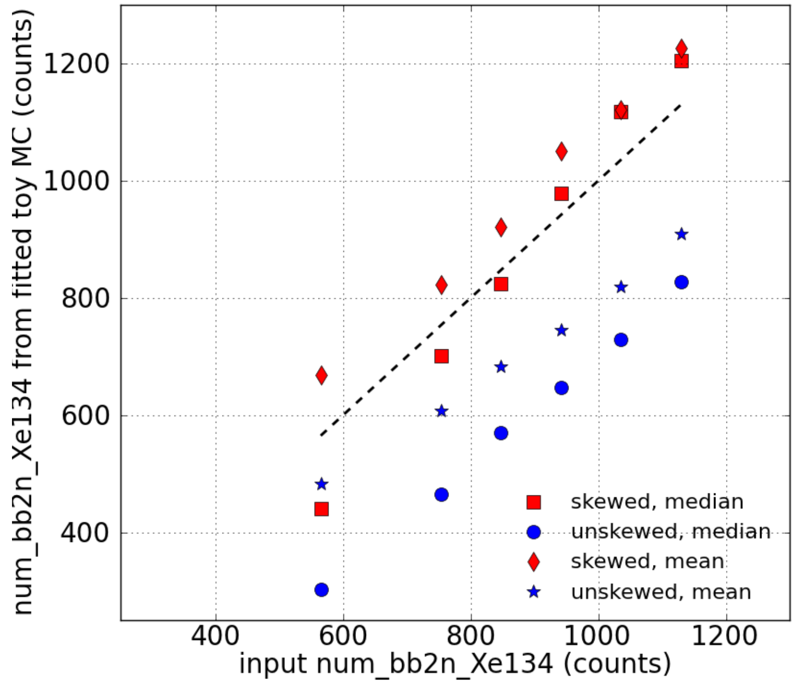

Figure 4.12: Toy MC study. The number of calculated events from toy data set is discrepant with the number of input events. The difference is used to determined the shape error. We observed rather large pulls between skewed toy numbers and the input numbers. This is not consistent with previous studies of the toy MC generation toolkit and further study is warranted. A conservative shape error is used for this analysis.

4.4 Results

For this measurement the following configuration was used in the fitting of the first year of the Phase II dataset:

1. The detection efficiency for ^{134}Xe $2\nu\beta\beta$ ($0\nu\beta\beta$) is 22.8% (70%) at the chosen energy threshold of 300 keV (740 keV). The detection efficiency actually improves all the way down to 210 keV however the shape error increases significantly at low energy (see shape agreement figure 4.8). 300 keV was chosen to balance the two effects.

2. The energy calibration is the same as that used in [63]. This is because even though the energy calibration uses two known peaks in the standard energy range ($\geq$ 1000 keV), it is linear and thus adequate for low energies too. The resolution somewhat worsens but it is not a factor for this search.

3. Since the dataset is the same as that used for the low background analysis in [63] the same model constraints are used. We however recalculate the shape error and single site fraction constraints as they are specific to this analysis.

All of these combined result in a total ^{134}Xe exposure of 13.46 kg·yr or 6.07×10^{25} atoms·yr. Figures 4.13-4.14 show the low background fits.

The best fit values is found to be 941 counts for $2\nu\beta\beta$ ^{134}Xe decays. Overlaid on figure 4.13 is the $0\nu\beta\beta$ ^{134}Xe spectrum for which the best fit value is consistent with zero (45 $\pm$ 98). Note that in the $0\nu\beta\beta$ case a threshold of 740 keV was used. This allowed us to omit the low background PDFs (^{85}Kr and ^{137}Cs) from the analysis. We also performed profile likelihood scans to determine the confidence intervals for the number of counts observed. These are shown on figures 4.15-4.16. When the shape error is added the net result is a widening of the profile curves.

The 90% CL limit for ^{134}Xe $2\nu\beta\beta$ is N$_{Xe-134}$ = 2766.1 decays. The corresponding half-life is given by:

$$T_{1/2}^{Xe-134} = \frac{\ln(2)\cdot t_l \cdot N_0 \cdot \epsilon}{N_{Xe-134}} \tag{4.18}$$

where t_l is the detector livetime (271.8 days = 0.744 yr) for the data set, ϵ is the $2\nu\beta\beta$ ^{134}Xe detection efficiency, and N$_0$ is the initial number of ^{134}Xe. Plugging in these values we get a half-life limit of $T_{1/2}^{2\nu} > 3.22\times10^{21}$ yr. This is a factor of >3.5 improvement to our Phase I result (8.7×10^{20} yr), with less than 50% the Phase I exposure (29.6 kg·yr). Despite the larger shape error (27%

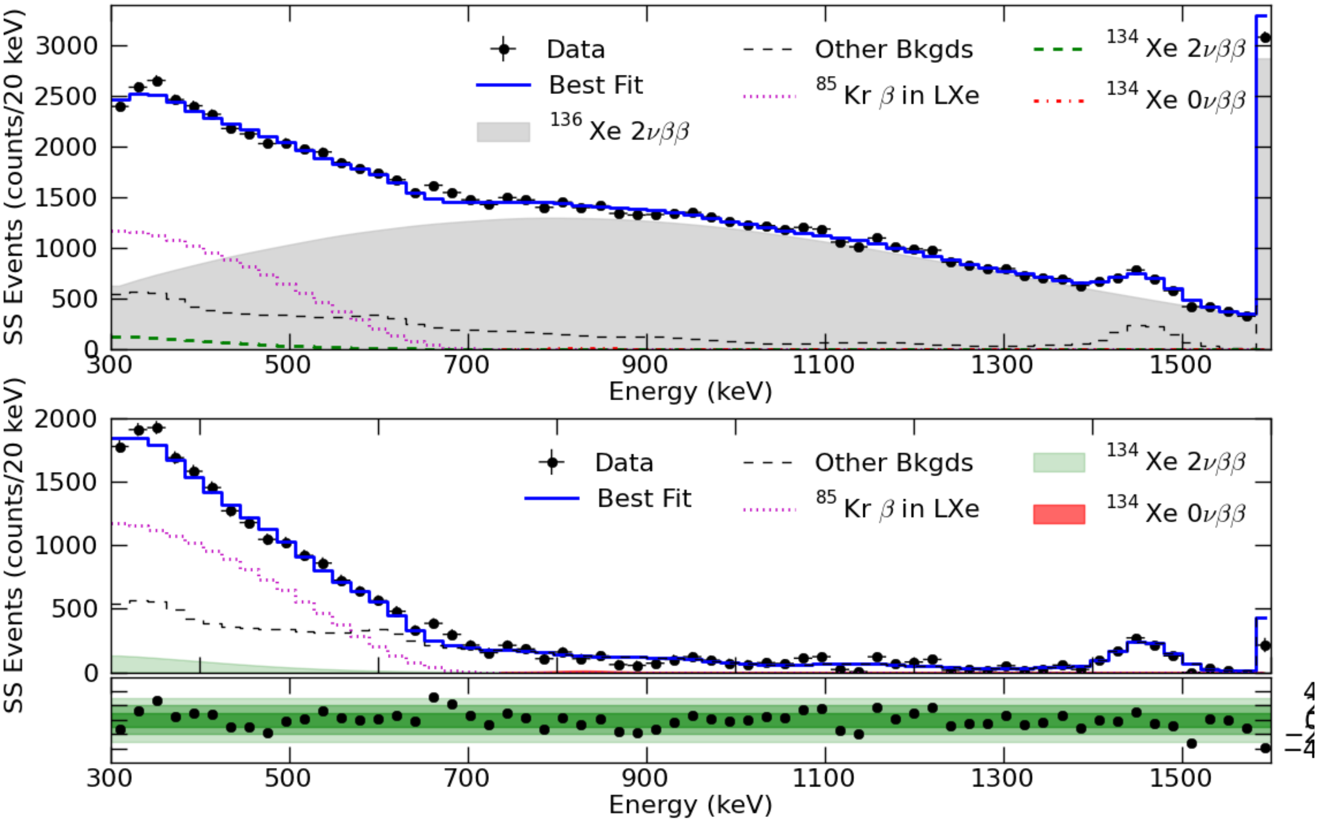

Figure 4.13: SS best fit. The top panel shows the full SS spectra. The last bin is the summed contents of all bins between 1600 keV and 9800 keV. The middle panel shows the spectra when the ^{136}Xe $2\nu\beta\beta$ background is subtracted. The bottom panel shows the residuals between data and best fit normalized to the Poisson error. The $0\nu\beta\beta$ (magenta) is overlaid on.

to Phase I's 25%) we obtained an improved limit mainly due the improved detection efficiency (22.8% in Phase II to 5.6% in Phase I). The sensitivity is 5.3 $\times$ 10^{21} yr. In the case of neutrinoless double beta decay we get $T^{0\nu}_{1/2} > 4.9 \times 10^{22}$ yr.

The ^{85}Kr beta decay spectrum is somewhat degenerate with the ^{134}Xe $2\nu\beta\beta$. THis is therefore a significant background to observing the double beta decay signal. The MIGRAD program calculated a correlation coefficient of -0.91 between the two PDFs before the shape error is included and -0.21 after inclusion of the shape error. Further detailed study of this background is required. However we tried to get an idea of its impact on the signal for the present analysis.

The number of ^{85}Kr decays observed in the best fit model with shape error included (figure

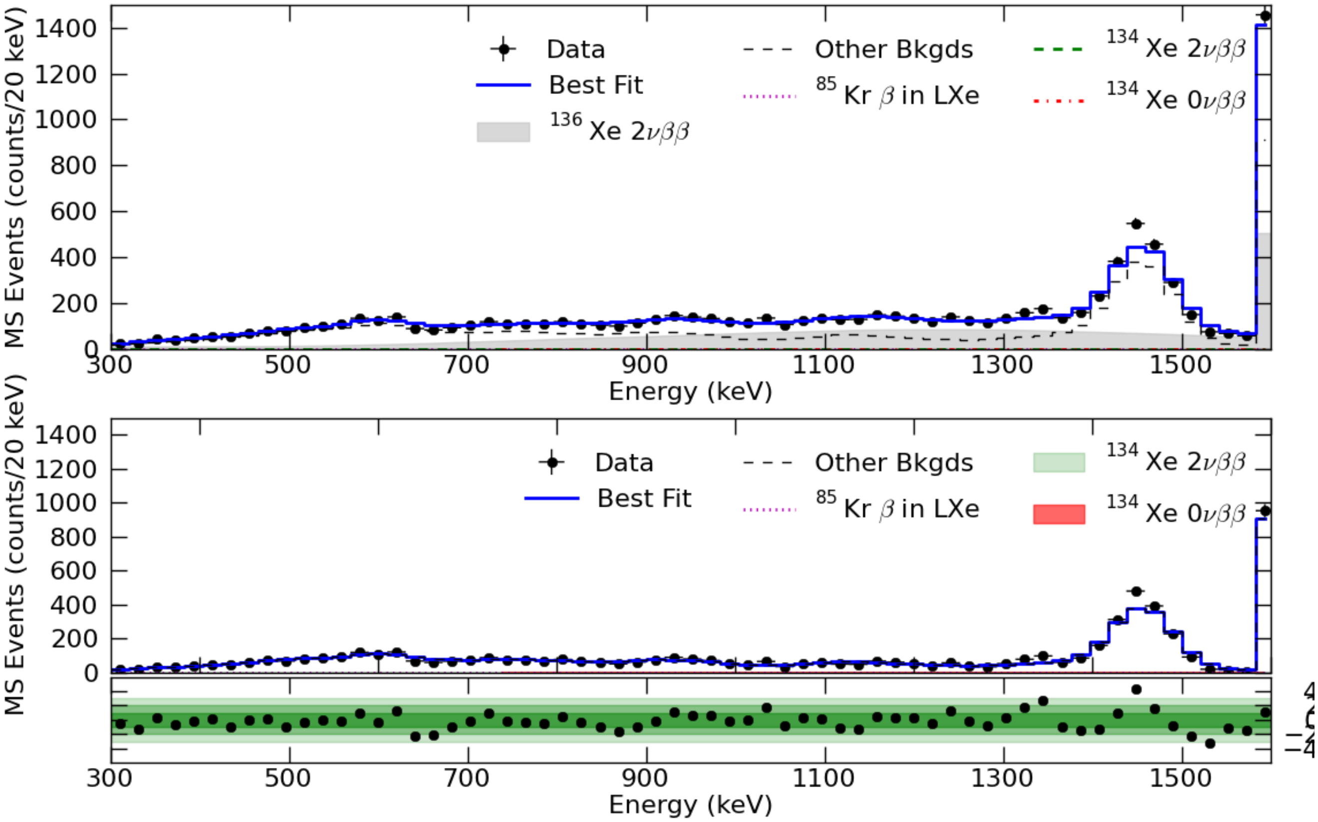

Figure 4.14: MS best fit. The top panel shows the full MS spectra. As expected from the SS fraction most of the $2\nu\beta\beta$ contribution is SS. The last bin is the summed contents of all bins between 1600 keV and 9800 keV. The middle panel shows the MS spectra when the ^{136}Xe $2\nu\beta\beta$ background is subtracted. The bottom panel shows the residuals between data and best fit normalized to the Poisson error.

4.13) is 11756 ± 1060 (vs 941 $2\nu\beta\beta$ counts). Another fit was performed where only the background PDFs are included, i.e. no $2\nu\beta\beta$ PDF. In this configuration we found 12876 ± 327 ^{85}Kr decays. This means that the total number of ^{85}Kr (12876) in the ”background-only” fit is consistent with the sum (12697) of ^{85}Kr and ^{134}Xe $2\nu\beta\beta$ in the background + signal fit.

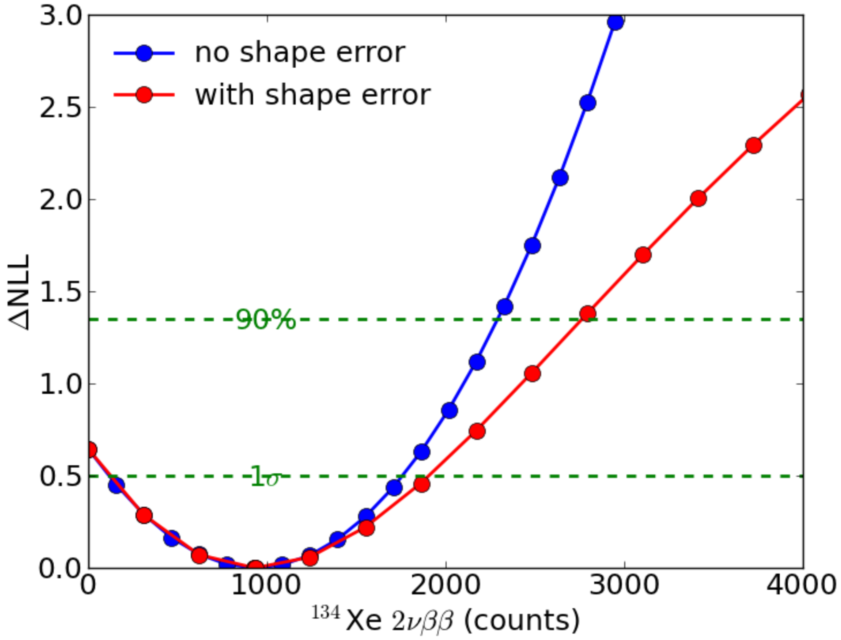

Figure 4.15: Profile likelihood scan for the number of $2\nu\beta\beta$ decays. When the shape error is added the profile widens. A more parabolic shape should be recovered with the addition of more data to the analysis.

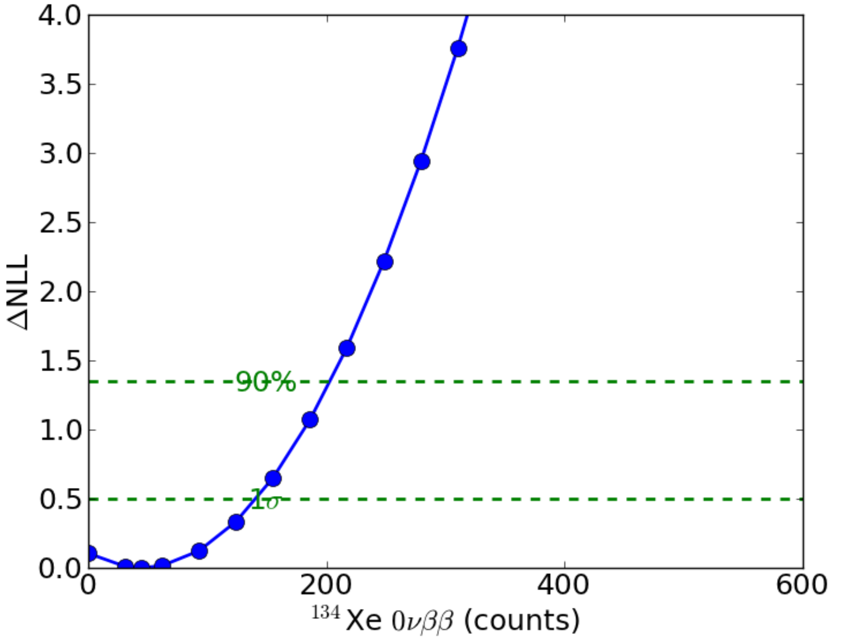

Figure 4.16: Profile likelihood scan for the number of $0\nu\beta\beta$ decays.

Chapter 5

The nEXO Concept

5.1 Overview

The nEXO concept is based on a Time Projection Chamber (TPC) filled with five tonnes of liquid xenon (LXe) enriched to 90% in the isotope with atomic mass number A = 136 (^{enr}Xe). This choice is directly derived from the success of EXO-200 and is motivated by the ability of large homogeneous detectors to identify and measure background and signal simultaneously. While the range of few MeV electrons in LXe is too short to be directly measured in a large detector, the most insidious background to $0\nu\beta\beta$ decay derives from γ-rays and, at the energies of interest, such backgrounds can be identified and separated from electrons of similar energies by the multiple Compton scattering they are likely to undergo. A fully efficient and monolithic detector is ideal for this purpose. This technique acquires more power as the linear size of the detector becomes large compared to the γ-ray attenuation length that, at 2.4 MeV energy in LXe, is $\lambda_{att} = 8.7$ cm. For detectors with linear size substantially larger than λ_{att}, backgrounds due to external γs are more attenuated the deeper the location is in the detector. Therefore, in a detector such as nEXO with linear dimensions exceeding 1 m, the external background can be identified over a wide range of energies, fit simultaneously with the signal, and rejected. According to the nEXO background model γ radiation emitted by sources external to the xenon constitutes the dominant background component. Backgrounds originating inside the LXe have been found to be entirely negligible at the 100 kg scale. Because of the efficiency with which a noble element such as xenon can be purified, this is expected to also be the case at the tonne scale. Backgrounds from α emission either from Rn dissolved in the LXe or from contaminations in the materials in direct contact with the LXe, are identified and rejected using their characteristically large scintillation-to-ionization ratio, as well as their spatial location for those on detector surfaces.

Energy resolution around the Q-value of the decay ($Q_{\beta\beta}^{^{136}Xe}$ = 2458.07 ± 0.31 keV [72]) is important, but not as crucial as with other types of detectors. Yet, the energy measurement remains the only handle capable of separating the $0\nu\beta\beta$ mode from the SM $2\nu\beta\beta$ decay.

nEXO is designed to optimize the unique features mentioned above, along with providing the best possible energy resolution for a LXe TPC. The total amount of enriched xenon in the system, 5109 kg, is chosen in such a way as to achieve a sensitivity consistent with the Nuclear Physics community's 2015 Long Range Plan [73]. A conceptual sketch of nEXO is shown in Figure 5.1 and the principal parameters of the experiment are presented in Table 5.1.

5.2 Background model and sensitivity

The details of the sensitivity calculations can be found in [?]. Here we will just summarize some of the key results in the interest of completeness.

nEXO's size and extremely low background levels, coupled with an analysis that exploits the multi-parameter event signature provided by the TPC technique, result in a dramatic improvement in sensitivity compared to EXO-200. nEXO's median sensitivity to the $0\nu\beta\beta$ half-life for ^{136}Xe at 90% C.L. is shown in figure 5.2 as a function of the experiment's livetime. After 10 years of data collection, the median 90% C.L. sensitivity reaches 9.2×10^{27} years. A 3σ discovery potential of 5.7×10^{27} years is predicted for the same live time.

The sensitivity to the $0\nu\beta\beta$ half-life of ^{136}Xe can be converted into the corresponding sensitivity to the effective Majorana neutrino mass $\langle m_{\beta\beta}\rangle$ under the assumption of light Majorana neutrino

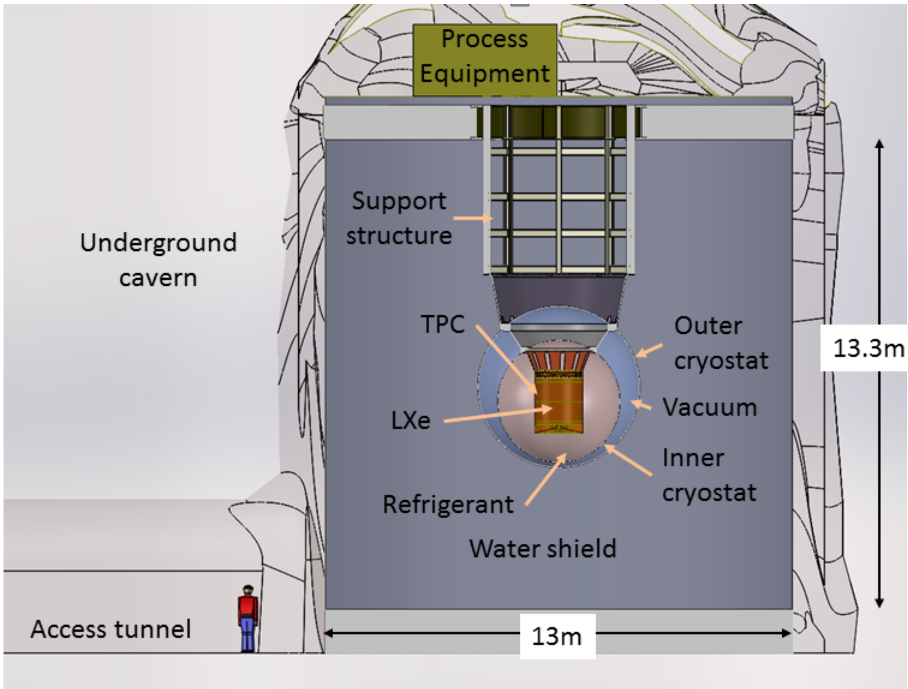

Figure 5.1: Sketch of the nEXO detector concept, showing the LXe TPC located inside a vacuum insulated cryostat filled with HFE-7000 refrigerant fluid, doubling as the innermost γ-ray shield. A substantially thicker shield is obtained with a large water tank, which also acts as an active cosmic-ray veto detector, based on Cherenkov light. While the host lab for nEXO has not been chosen, for concreteness, the sketch assumes that the detector will be located in the Cryopit at SNOLAB [14].

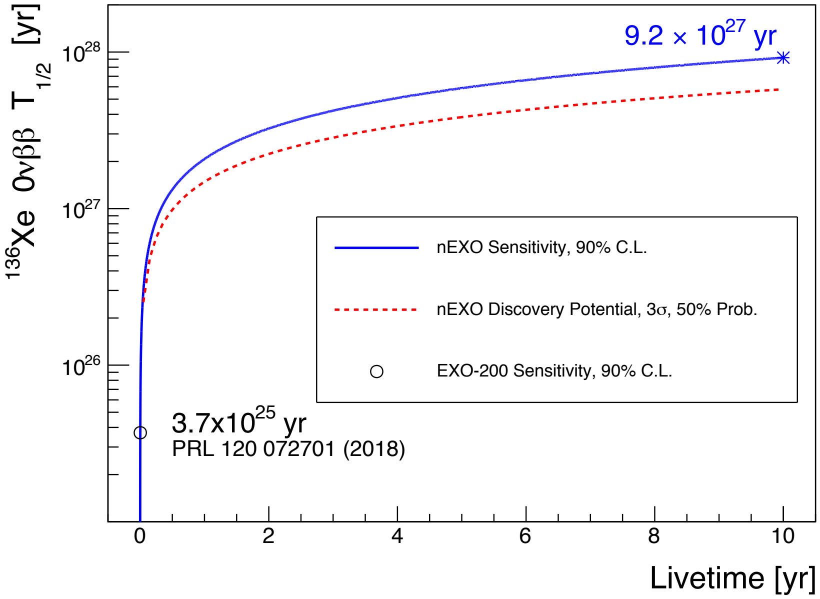

Figure 5.2: nEXO median sensitivity at 90% CL and 3σ discovery potential as a function of the experiment livetime.[14].

Parameter	Primary Value
^{en}Xe inventory	5109 kg
Maximum fiducial enr Xe	4038 kg
136 Xe isotope abundance	90%
enr Xe operating temperature	165 K
enr Xe liquid density	3.057 g/cm^3
Electric drift field	400 V/cm
Maximum electron drift distance	125 cm
Electron lifetime in LXe	>10 ms
Xe recirculation rate	350 slpm
Diameter of drift volume	116 cm
Charge read-out strip pitch	3 mm
LXe scintillation light wavelength	175 nm
Photodetector area	4.5 m^2
Photodetector dark noise rate	50 Hz/mm^2 0.1 p.e. threshold
Overall light detection efficiency	$>3\%$
RMS electronics noise (charge channel)	$200-250e^-$
RMS electronics noise (scintillation channel)	0.1 p.e
Inner Cryostat Vessel diameter	338 cm
Outer Cryostat Vessel diameter	446 cm
HFE-7000 mass	32,000 kg
Cool-down/warm-up time	30 days
Minimum HFE-7000 shielding thickness	0.76 m
Water Tank height	13.3 m
Water Tank diameter	13 m
Minimum water shielding thickness	4.25 m
$\beta\beta$ decay Q-value	2458.07 ± 0.31 keV
Energy resolution $\sigma/Q_{\beta\beta}$	$\leq 1.0\%$
MS rejection at $Q_{\beta\beta}$	$>10:1$
SS background rate inner 3000 kg	8.6×10^{-4} events/(FWHM·kg·yr)
SS background rate inner 2000 kg	3.6×10^{-4} events/(FWHM·kg·yr)
SS background rate inner 1000 kg	1.4×10^{-4} events/(FWHM·kg·yr)
90% CL sensitivity $T_{1/2}$	$9.2\dot{1}0^{27}$ yr (10 yr data)
90% CL sensitivity $\langle m_{\beta\beta}\rangle$	5.7-17.7 meV (10 yr data)
$3\dot{\sigma}$ discovery potential $T_{1/2}$	$5.7\dot{1}0^{27}$ yr (10 yr data)
$3\dot{\sigma}$ discovery potential $\langle m_{\beta\beta}\rangle$	7.3-22.3 meV (10 yr data)

Table 5.1: Compilation of primary design values of some important nEXO parameters. The explanation of symbols and the description of functions can be found in various sections of this document.[14].

exchange. Figure 5.3 shows the nEXO exclusion sensitivity to $\langle m_{\beta\beta}\rangle$ as a function of the lightest neutrino mass. The allowed neutrino mass bands are derived from neutrino oscillation parameters from [74]. The $\langle m_{\beta\beta}\rangle$ exclusion band between 5.7 and 17.7 meV arises from the range of nuclear matrix elements, with EDF [75] and QRPA [76] at the minimum and maximum extreme respectively. Majorana neutrino masses are computed assuming the unquenched value of the axial-vector coupling constant of gA = 1.27 [34].

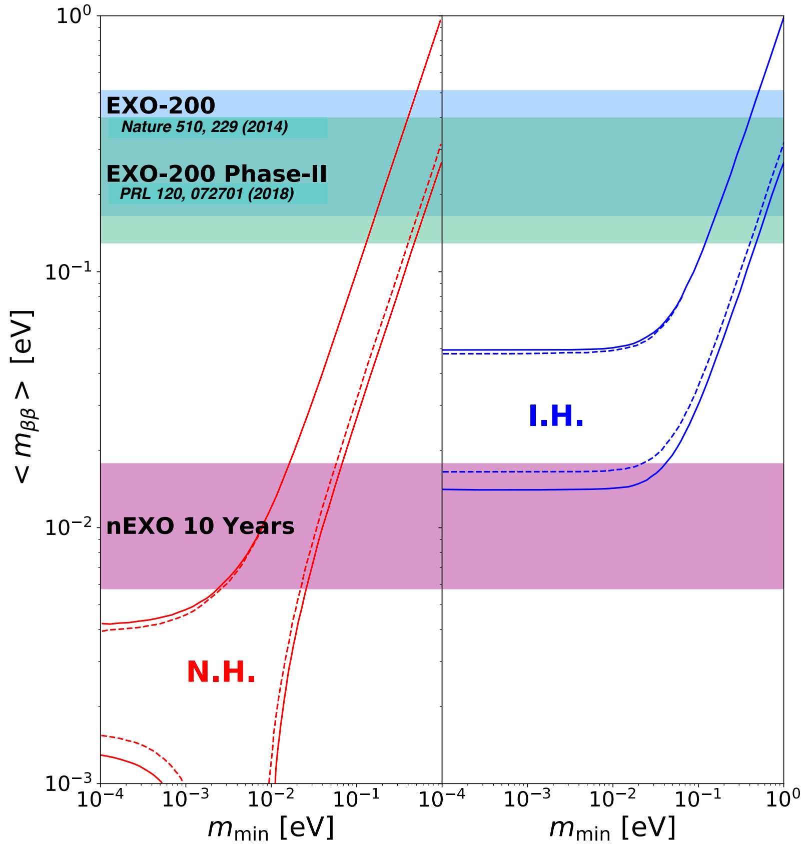

Figure 5.3: 90% C.L. exclusion sensitivity reach to the effective Majorana neutrino mass $\langle m_{\beta\beta}\rangle$ as a function of the lightest neutrino mass for normal (left) and inverted (right) neutrino mass hierarchy. The width of the horizontal bands derive from the uncertainty in nuclear matrix elements (see text) and it assumes that $g_A = 1.27$. The width of the inner dashed bands result from the unknown Majorana phases and is irreducible. The outer solid lines incorporate the 90% CL errors of the 3-flavor neutrino fit of reference [74].[14].

Ongoing efforts focus on reducing the SS backgrounds through advancement in material screening and selection, optimization of the detector components (e.g. mass and location), and improved analysis. A parametric study was performed to evaluate the improvement in $0\nu\beta\beta$ sensitivity as a function of the total background. All materials activities from Table 6.1 were uniformly scaled down by a progressively larger fraction, with the exception of the $2\nu\beta\beta$ component which was held constant. New toy data sets were generated and then fit to obtain a median sensitivity estimate for different background scenarios. The resulting curve is shown in Figure 5.4, assuming 10 years of data taking. The $0\nu\beta\beta$ sensitivity increases by a factor 4 as the background rate is lowered by two orders of magnitude. The point labeled “baseline” refers to the case described in this report, while “aggressive” refers to a case in which plausible improvements are made.

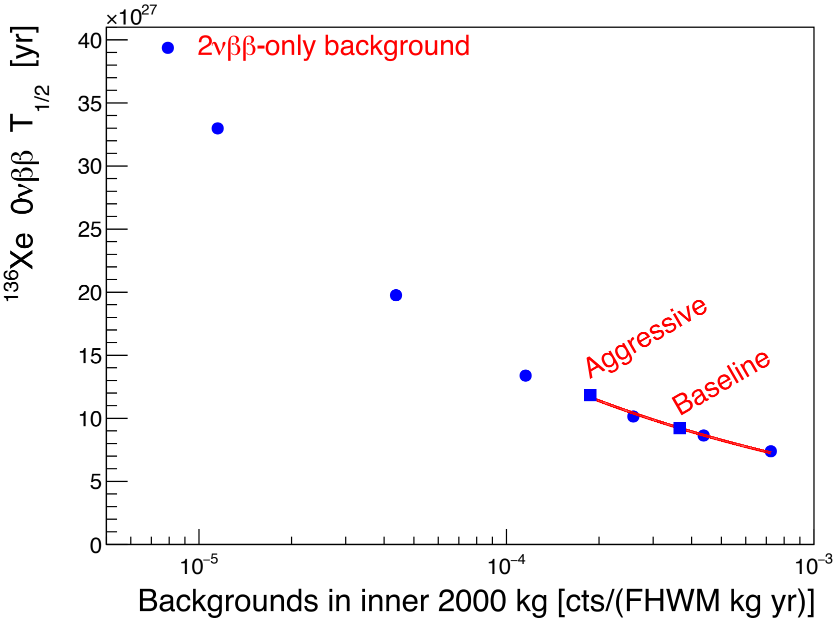

Figure 5.4: Sensitivity (blue circles) to the $0\nu\beta\beta$ half-life of a nEXO-like experiment as a function of total background in $Q_{\beta\beta} \pm FWHM/2$ in the inner 2000 kg. All components of nEXO’s background model except for the $2\nu\beta\beta$ term are scaled to generate this curve. The red curve is the result of fitting the computed values with $T^{0\nu}_{1/2} \propto B^x$, giving $x = -0.35$ over the fitted region. The blue squares represent the sensitivity of the primary detector design discussed here, as well as an aggressive, but plausible improvement of the detector performance.[14].

5.3 The detector

5.3.1 The TPC

The design of the nEXO Time Projection Chamber (TPC) is rooted in that of EXO-200 [58]. It is a single-phase, LXe TPC filled with 5 tonnes of enriched xenon. The main design driver for the nEXO TPC is the realization of the largest possible, monolithic, instrumented LXe volume that allows to maximally exploit the background identification, suppression, and discrimination capabilities demonstrated by EXO-200.

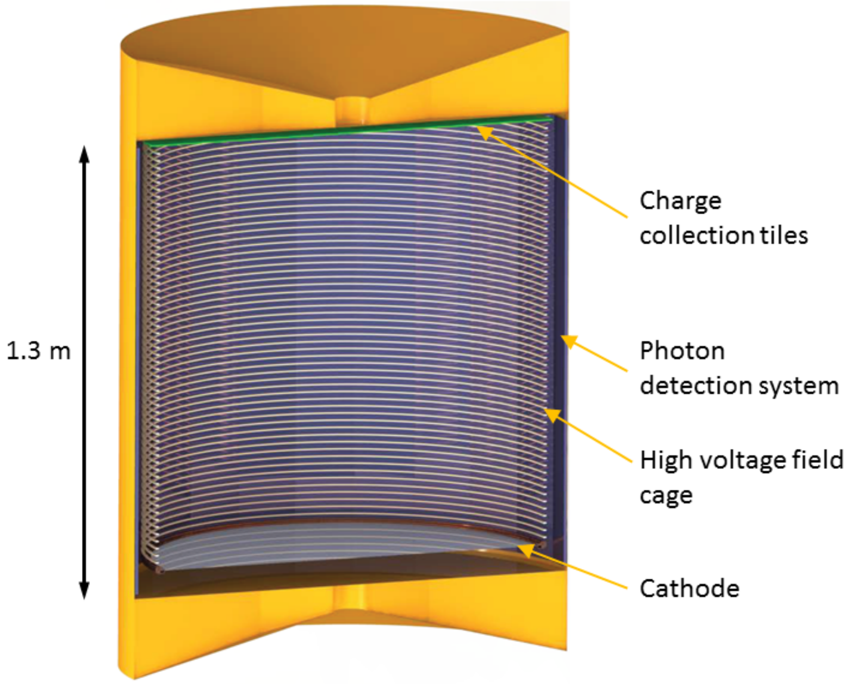

Figure 5.5: Sketch of the nEXO TPC. The copper vessel, cathode, charge collection anode and photodetectors, behind the field-shaping rings are schematically shown. For simplicity, this sketch does not show the high voltage and other electrical and Xe recirculation feedthroughs.

The main features of the nEXO TPC design include:

1. One single, 125 cm long drift volume, with anode and cathode at opposite ends of a cylinder having its base of 115 cm diameter (see Figure 5.5). This choice allows to define a large, all-xenon core of the detector where the radioactive background is essentially reduced to that intrinsic to the xenon source itself.

2. In nEXO, the single, long drift volume requires excellent xenon purity from electronegative contaminants, with electron lifetimes better than 10 ms. This requirement derives from the expected quality of the electron lifetime correction needed to obtain a sufficient energy resolution. More details regarding the derivation of this requirement can be found in [14]. The nEXO TPC is designed with minimal use of large-area plastic components, which are

known to out-gas impurities in vacuum-grade systems. In addition, the larger a monolithic detector is, the smaller the surface-to-volume ratio becomes, which reduces the load from out-gassing impurities. Finally, the diffusion of the ionization as it drifts the entire length of the TPC [71] is small enough not to degrade the topological information provided by the TPC.

3. The HV design parameters are derived from EXO-200, with appropriate scaling arguments. In the current, very conservative, configuration, the cathode needs to be safely biased to up to -100 kV, allowing for a maximum drift field of $\sim$ 800 V/cm, twice that adopted in EXO-200 phase I [63].

4. A particularly delicate component of the nEXO TPC is its cathode. The primary design calls for a thin, slightly tensioned, $\sim$125 μm-thick copper (or bronze) sheet, made VUV reflective by a thin layer of vacuum-evaporated aluminum protected by a final MgF_2 coating. Figure 5.5 shows the assembly.

5. For nEXO, it was suggested [77, 78] to adopt a modular charge collection scheme without a Frisch grid. Fused silica tiles of approximate dimensions $\sim 10 \times 10$ cm^2 are metalized with crossed strips of interleaved square pads, nominally 3 mm center-to-center. A tiled anode has the advantage of allowing for a modular assembly, with individual modules assembled, tested, installed, and integrated with the readout electronics, interconnections, and cables.

6. Efficient scintillation light collection is an essential requisite for nEXO to attain proper energy resolution and to provide the start time to localize events along the drift field. This challenge increases with the size of the detector, due to the larger surface area to be instrumented. Recent technological advances, however, make the task possible by using Silicon Photo-Multipliers (SiPMs). In nEXO, xenon scintillation light will be collected with a large-area array ($\sim$c4.5 m^2) of SiPMs, a departure from EXO-200, where Large-Area Avalanche Photodiodes (LAAPDs) were used [79].

7. The SiPM array for nEXO is installed on the xenon vessel barrel surface, behind the TPC field shaping rings. This is a departure from EXO-200, where the LAAPD photosensors are placed behind the anode crossed-wire planes. This arrangement is motivated by the larger surface of the TPC that can be covered to improve the overall light collection efficiency, and by the anode tiled design, which is no longer optically transparent (in the primary nEXO TPC concept the cathode is also opaque).

8. In nEXO, ionization and scintillation signals will be read out by cryogenic, in-xenon, low-radioactivity front-end electronics.

9. The nEXO TPC package will be mounted to a top flange and vertically lowered into the xenon vessel, as is standard for cryogenic setups. This is a departure from the cantilevered EXO-200 design, which was dictated by the limited vertical clearance available at the WIPP site.

5.3.2 Readout Electronics

The purpose of the electronics is to amplify, condition and digitize the charge and scintillation signals produced in the nEXO TPC. Locating these functions near the origin of the signals, inside the TPC at cryogenic temperature, has a number of advantages. The capacitance from the connections of the charge collecting devices to the preamplifiers is minimized with respect to more conventional room temperature electronics that would have to be located over 2 m away, outside of the cryostat. In addition, the long cables transmitting analog signals would be more susceptible to electromagnetic pickup. The low temperature environment results in lower noise for the input transistors. Finally, digitizing all signals inside the TPC reduces the number and/or size of cables and feedthroughs, simplifying the assembly and increasing the reliability. While many experiments have found it difficult to produce ultra-low background cables, in several cases silicon devices have been measured to have extremely low radioactive contaminations. Thus, the replacement of long cable runs with silicon chips in proximity of the fiducial volume is likely to reduce the overall radioactivity load of the detector.

The design of electronics to be located in the TPC presents a number of challenges that have to be met in order to achieve the advantages described. In particular, the electrical specifications need to be fulfilled while complying with the ultra-low outgassing and radioactivity requirements. This leads to limits in both the total amount of materials and the number of different components, as each component needs to be carefully tested. In the case of electronics, these issues generally preclude the use of discrete components and naturally lead to the use of integrated techniques, where several channels can be integrated onto a very thin piece of silicon measuring only a few millimeters on each side.

Another important factor in the design of the nEXO electronics is the limited power budget, needed to ensure that the power dissipation within the cryostat does not cause unwanted temperature gradients which, in turn, may lead to excessive convection and, in the extreme, formation of gas bubbles within the LXe.

The main requirements for the nEXO electronics are listed in Table-5.2.

Parameter	Charge channel	Scintillation channel
Operating temperature	165 K	165 K
Number of channels	< 6000	< 6000
Front end type	current amplifier with anti-alias filters	current amplifier
RMS noise floor	$200e^{-}$	0.1 single photoelectrons
On chip calibration	0.2%	N/A
ADC resolution	12 bits	12 bits
ADC, INL, DNL	< 1 bit	N/A
Sampling rate	2 MS/s	N/A
ADC, INL, DNL	continuous time waveform sampling bit	photon counting with spatial trigger
Power	< 10 mW/ch	< 10 mW/ch

Table 5.2: List of key specifications of the nEXO front end readout. INL (DNL) refer to integral (differential) non-linearity.[14].

5.3.3 Cryogenic system

The cryogenic system includes the cryostat, the refrigeration infrastructure and the xenon and HFE-7000 handling systems. The tasks of the cryogenic system are to support stable conditions for optimal detector operation and to protect both the delicate apparatus and enr Xe stockpile in liquid phase. These goals must be accomplished while also meeting low background requirements, including the requirement on dissolved Rn, and guaranteeing a sufficient electron lifetime in the TPC. It is useful to consider that the components physically located inside the cryostat (including the cryostat) have to be built out of low background materials, while for elements in the cryogenic fluid systems which are outside the cryostat the concern is only that of outgassing and Rn emanation.

Here is a summary of requirements for the cryogenic system:

1. The LXe vessel is cooled and shielded by a vacuum-insulated cryostat containing 32,000 kg of HFE-7000 fluid. Both the inner and outer cryostat vessels will be spherical in order to optimize the strength/mass ratio. In the primary concept, the vessels will be made of carbon composite material and lined with a thin, low background liquid-resistant material such as titanium.

2. The "system pressure", that is the pressure of the LXe and, by design, the HFE-7000, during operations, is a free parameter that can be chosen at the design phase. The range of temperature over which xenon is in liquid phase increases with pressure, going from 3.6 K at 1 bar to 11 K at 1.5 bar. Hence, running at a higher system pressure reduces the risk of boiling or freezing of the LXe.

3. The refrigeration system must provide sufficient cooling power to cool down the large thermal mass from room temperature to 165 K in less than one month. It must also be capable of maintaining the system at low temperature with temporal variations of < 0.1 K over the course of many years of data taking.

4. In order to be useful as a detection medium, the LXe must be free from electronegative impurities such as oxygen, nitrogen, and water vapor. Xenon purification is accomplished in the gas phase through the use of heated zirconium getters, a technique already employed by EXO-200 [58], XENON [80, 81], and LUX/LZ [82, 83].

5. The xenon recovery system is a critical component, meant to safely recover the xenon in gas form when the detector is emptied, either for planned operational reasons or in case of emergency. While the large thermal mass at base temperature makes the system resilient to short-term power outages or other interruptions of cooling, a recovery system is being developed to safely return the xenon to high pressure storage.

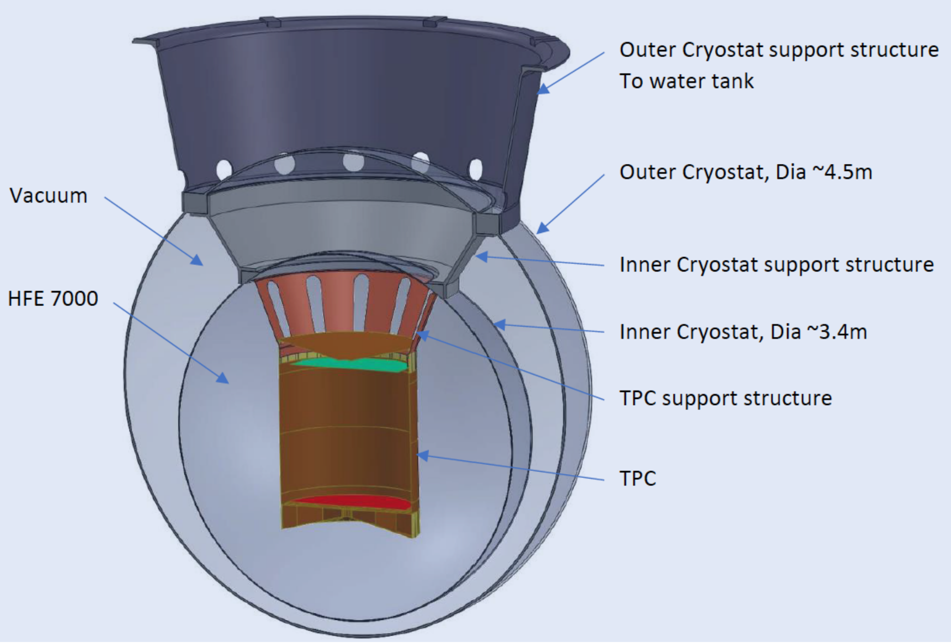

Figure 5.6: Cutout model of the nEXO cryostat system.[14].

5.3.4 Calibration

SBU leads the calibration R&D effort for nEXO. An important component of the detector design is the incorporation of a set of capabilities to:

1. achieve a complete understanding of the detector response to double beta decays over the full range of energies throughout the detector volume.
2. accumulate the required calibration data to monitor variations in the calibration parameters.

To this end a ”baseline” calibration to understand the ionization and scintillation responses, the charge-light anti-correlation and the electron drift parameters over the entire fiducial volume is being developed. One key aspect is developing an adequate external source calibration.

The use of external sources for nEXO is challenging due to the size of the detector. This is because, as previously mentioned, gammas in the energy region of interest have an attenuation length of just 8 cm. Nevertheless a series of simulations have shown that a useful energy calibration can still be achieved using external γ-ray sources. The questions to be answered are 1) what source activity is adequate? And 2) how long and how frequent should calibration campaigns be performed.

In one of the MC simulation exercises six ^{228}Th sources are simultaneously deployed in guide tubes around the TPC as shown in figure 5.7. It is found that the optimal source activity for a regular two-hour run is 850 Bq for the sources at PX, PY, NX, and NY and 85 Bq for the remaining two positions.

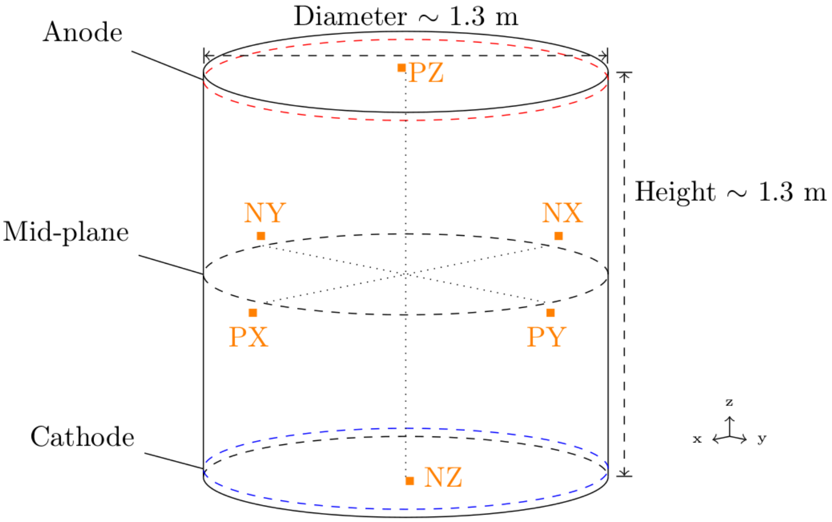

Figure 5.7: Source positions (shown as orange squares) around the TPC.[14].

Another MC study looked at the calibration needs for the electron lifetime requirements. Ionization was generated using the ^{228}Th as described above and resulting electrons were drifted in the TPC at various lifetimes. The reconstruction technique is detailed in the pCDR [14]. Table-5.3 compares the true (simulated lifetime) to the reconstructed (fitted lifetime). The takeaway here is that 10 ms lifetimes can be measured to better than 4%. Another study showed that the uncertainty in the lifetime measurement had a minimal impact on the charge energy measurement.

True Lifetime [ms]	Inverse Lifetime $[(ms)^{-1}]$	Fitted Inverse Lifetime $[(ms)^{-1}]$
2	0.5	0.4989 ± 0.0035
5	0.2	0.2016 ± 0.0037
10	0.1	0.1015 ± 0.0038
20	0.05	0.0535 ± 0.0037
50	0.02	0.0212 ± 0.0031

Table 5.3: The fitted (inverse) lifetimes from simulated calibration data compared with the values fed into the Monte Carlo.[14].

To implement external calibration the necessary hardware will need to be developed. Currently this hardware consists of a) two guide tubes; b) source-cable assemblies; and c) deployment-retraction manipulators. The design of these elements is inspired by the hardware developed for EXO-200 which performed satisfactorily. More details can be found in the pCDR [14].

nEXO also needs to understand the light collection efficiency as a function of event position. This calibration corrects the portion of the event energy measurement that depends on the total light collected. To determine this correction, nEXO will produce calibration events throughout the TPC at a known energy or energies and observe how the measured light of these events varies according to event position. The final result of the calibration is a light response function (LRF) that describes the measured light response as a function of energy and position.

There are other calibration ideas being explored. One involves the possibility of injecting ^{220}Rn or ^{222}Rn in the LXe with the purpose of generating events deep in the TPC. This method would provide a more uniform event distribution in the detector and could be used to occasionally map, over the entire volume, the scintillation collection and the LXe purity. Another emergent idea is to have a continuous monitoring system relying on calibrated laser pulses driving judiciously placed photocathodes or tuned to produce localized charge clusters from multi-photon ionization of LXe. This is in fact a major component of the present thesis and is discussed in great details in chapter 6.

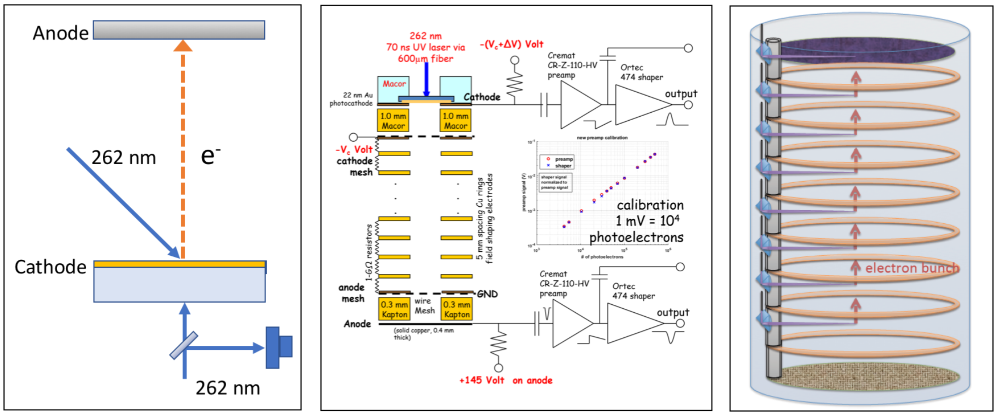

Figure 5.8: Concept of laser calibration by photoinjection of charge (left); SBU-BNL test setup (center); possible concept for calibration by multiphoton ionization of LXe (right).[14].

5.3.5 Water shielding and veto detector

Large water tanks are commonly used to shield against external backgrounds and veto the passage of muons. This approach is attractive because of cost considerations, hermeticity and the possibility of being instrumented as Cherenkov counters. While the low density of water increases the required thickness, its hydrogen content makes it ideal for neutron moderation. The light nuclei in water also minimize neutron production by cosmic-ray spallation.

A tank of ultra-pure deionized water has been identified as shielding of choice for nEXO. The cryostat, containing the TPC, will be submerged and placed at the center of this water volume, serving three purposes: (I) shield against γ-rays originating from radioactive decays in the walls of the underground cavern; (II) moderate and stop neutrons also produced in the walls and (III) detect cosmic radiation, i.e. muons, passing through the water and potentially producing correlated events in the TPC. Items (I) and (II) require passive shielding only, while the detection of cosmic muons requires instrumentation. In addition to rejecting cosmogenic backgrounds, the direct measurement of incident muons allows the validation of the Monte Carlo simulation of cosmogenic backgrounds.

Photomultiplier tubes (PMTs) will be installed on the outer walls of the water tank, where they are shielded by the water with respect to the central detector, to detect the Cherenkov light produced by muon tracks. The information collected in this way will be added to the data stream so that correlation with events in the TPC can be studied offline (see e.g. [63]).

5.4 Facilities

nEXO will require a sufficiently deep underground site to properly operate. While the overburden of SURF [84, 85] at the 4850 ft level is expected to be sufficient for the experiment, the deeper SNOLAB site further reduces risk associated with cosmogenic backgrounds and minimizes shielding requirements [15].

Figure 5.9 shows a cutaway of the Cryopit at SNOLAB with access from both the top and bottom levels. More details can be found in the nEXO pCDR [14].

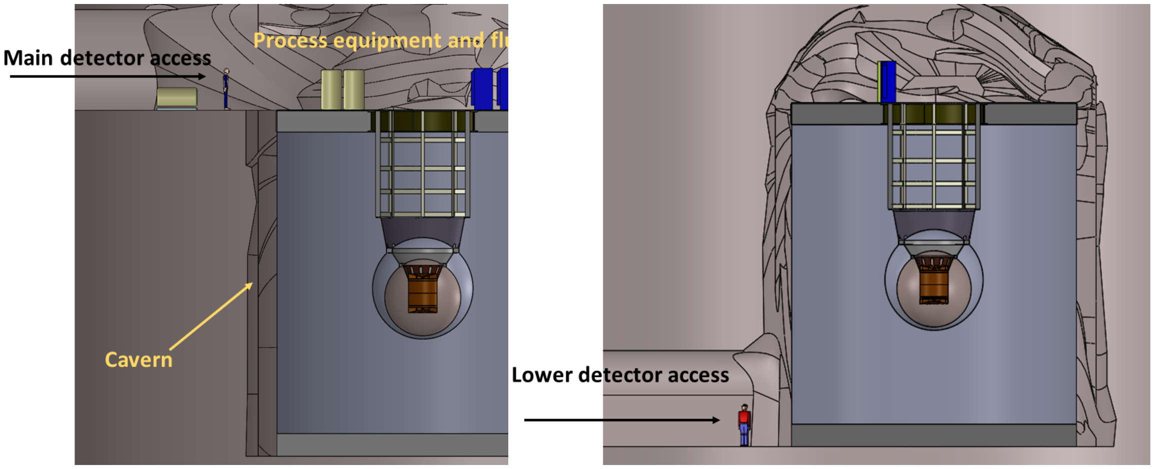

Figure 5.9: Access to the nEXO detector in the Cryopit at SNOLAB. Left: main access from the drift at top level. The drift is expected to be roughly level with the deck above the veto tank, from where the cryostat is supported. Most other services are located on the deck. Right: lower access, which is normally sealed because it is connected to the “dirty” portions of the mine. Some equipment may be installed in the lower drift, near the main heat exchangers for SNOLAB. The lower drift is also used for emergency personnel egress.[14].

Chapter 6

Laser-Driven *In-Situ* Electron Lifetime Monitoring

6.1 Introduction

In chapter 3 we described how EXO-200 exploits the anti-correlation between ionization and scintillation in LXe to optimize its energy resolution. nEXO plans to do the same to achieve its 1% design resolution (see Chapter 5). Another factor in achieving this goal is to purify the xenon in such a way that electronegative impurities that can deplete cluster charge is well below 1 ppb O_2 equivalent. The purity of the xenon is parametrized by the electron lifetime which is defined as the time it takes for a charge cluster drifting in the LXe to lose 63% (decay to 1/e) of its charge. The maximum drift time in nEXO will be of the order of 650 μm, a factor of 6 or so longer than in EXO-200 where we achieve an electron lifetime greater than 3 ms. This means that in EXO-200, even clusters that drift the full length of the detector lose at most 3.3% of their charge, so knowing the electron lifetime to 10% is sufficient to make any impact on energy resolution negligible.

We aim for an electron lifetime of 10 ms in nEXO. This implies a loss of 6.3% of the charge for a cluster that drifts from the cathode. In order to have a negligible effect on the energy resolution, we will need to monitor the electron lifetime to 2 or 3% over time and position inside the TPC.

In chapter 5 we showed that Monte Carlo simulations suggest this is achievable, with no more than 10% loss in data collection efficiency, if we perform a daily (2 hours) radioactive source calibration. However this may not be sufficient since the sources primarily sample the drift region in the peripheries of the TPC vessel. This is why it would be advantageous to have an *in-situ* method to monitor the electron lifetime (and achieve this without further loss of data collection efficiency).

Our proposal is to measure the electron lifetime by periodically illuminating small photocathodes (spread over the TPC cathode) with calibrated amounts of laser light. In this scheme, the resulting charge clusters will be measured at the anode (Q_a) and the ratio of the expectation (Q_c) to the measured charge would reveal the electron lifetime. If the expectation for the amount of charge is known accurately enough, the required accuracy for a 10 ms lifetime of better than a few % can be achieved. Demonstrating the feasibility of this approach was one main thrust of my thesis. In the rest of this chapter we will describe the cell we built and measurements we made towards this effort.

6.2 Apparatus

The Laser Metrology group at BNL's instrumentation division operated a mini Liquid Argon TPC between 2011 and 2014 as part of an R&D effort for the DUNE experiment at FermiLab. Results from their work can be found in [86]. We inherited this cell in the early part of 2015. Though operational, some upgrades needed to be made to the components inside the cell. The purity requirements for LXe are typically more stringent than those for LAr due to the fact that LXe (161 K at 1 bar) is much warmer than LAr (87 K = at 1 bar). Another major upgrade to the existing setup was the construction of a xenon recovery system. The Ar used for testing was generally released into atmosphere at the end of runs; this would not be possible for LXe which is considerably more expensive (1.20 USD/gram). Lastly the original drift structure was built using G10, a material made of high-pressure fiberglass, and which we later determined inappropriate for the required

LXe purity.

6.2.1 LXe cell

We generate electrons (used interchangeably with charge cluster in this chapter) by driving a semitransparent gold photocathode with a pulsed UV laser. Figure 6.1 shows a cartoon of the entire system. The cell is a 0.53 L aluminum cylinder with an inner diameter of 5 cm and a height of 27 cm. The top/cover is a 4-1/2" ConFlat (CF) flange which supports three smaller 2-3/4" CF flanges on which various vacuum feed-throughs (thermocouples, high voltage, optical fiber) are mounted. On the main body of the cell near the top are two 1/4" holes for gas xenon delivery and recovery and a third one to which is attached the pressure gauge and a (2 bar) pressure relief valve.

The cell can be pressurized to 2 bar, only limited by the glass viewport located at the top of the cell for visual inspection and confirmation of liquefaction. We employ all stainless steel pipes and valves in the xenon gas purification and recovery system (described in next subsection). Furthermore, the biggest components inside the cell are made of ceramics to minimize out-gassing. All high voltage (HV) feed-throughs and thermocouples are Kapton-insulated. With these considerations and proper UHV (Ultra-High Vacuum) handling techniques, vacuum levels in the low 10^{-9} torr range are achieved without need for regular system bake out.

The cell houses an optical fiber for photon delivery, thermocouple sensors for temperature measurement, a drift stack composed of a gold (Au) photocathode, copper field shaping rings, and an anode grid followed by a copper anode (see figure 6.2). The photocathode is a 22 nm thick gold film ($\sim$50% transmission at 266 nm) thermally evaporated on a 1 mm thick, 10 mm diameter sapphire disk (see figure 6.3). Before evaporating the gold for deposition the sapphire disk was coated with chromium to facilitate gold adhesion. All photocathodes are made by the Instrumentation Division at BNL. The sapphire disk sits in a macor holder at the top of the drift stack. Figure 6.4 shows a picture of the drift stack.

A 250 μm thick phosphor bronze disk with a clear inner diameter (ID) of 8 mm is negatively biased and makes electrical contact with the photocathode; it is securely fastened to the macor

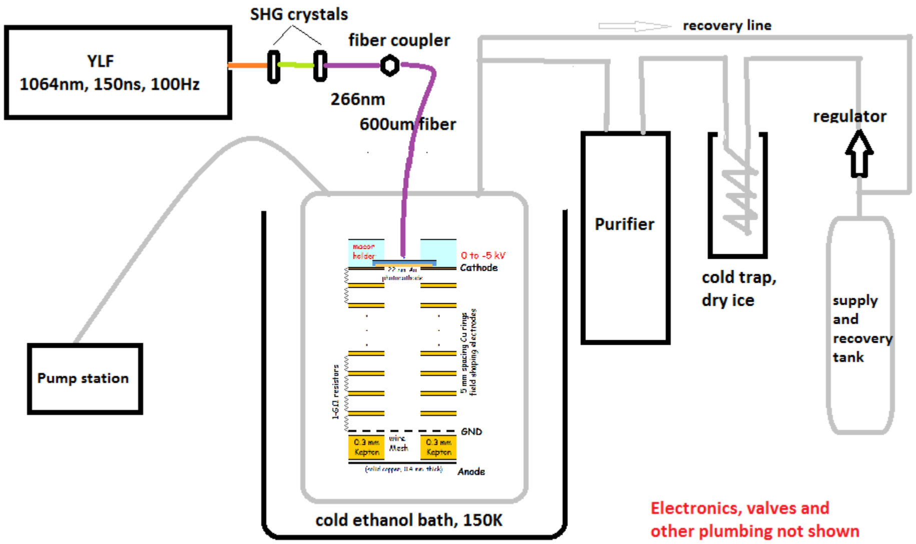

Figure 6.1: Diagram of the LXE system.

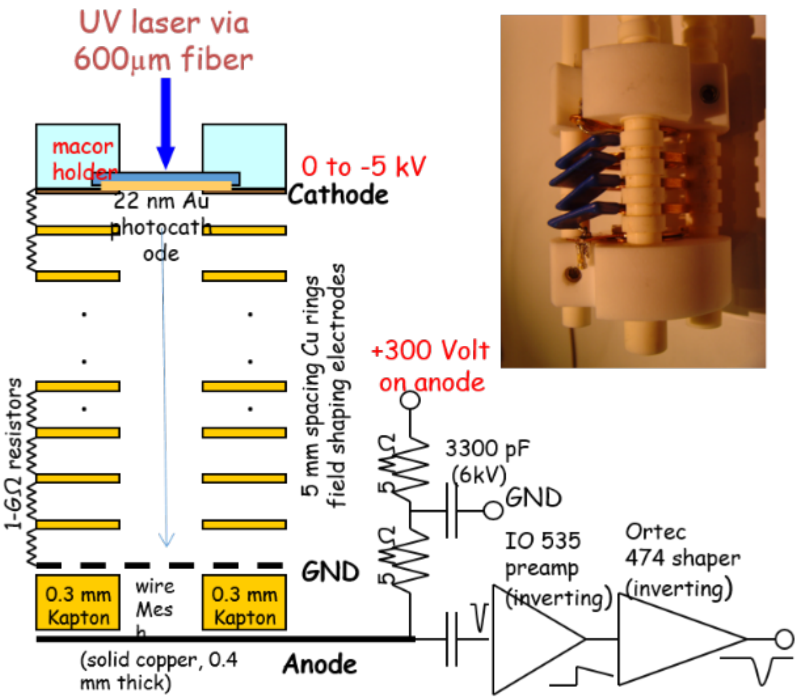

Figure 6.2: Schematic diagram of the drift stack. A uv laser back-illuminates a gold photocathode via a 600 micron fused silica fiber. The space between the photocathode and the mesh define the drift region, where a uniform drift field is maintained with the help of copper field shaping rings. The electron signals are collected with the charge-sensitive preamplifier. The calibration for the preamplifiers is shown on the right.

Figure 6.3: Picture of a photocathode. It is a 1mm sapphire disk on which gold was evaporated to a thickness of 22 nm. Between the gold and the sapphire is a layer of chromium to facilitate adhesion. The discoloration on the edge is a result of the phosphor bronze plate contact fo HV biasing.

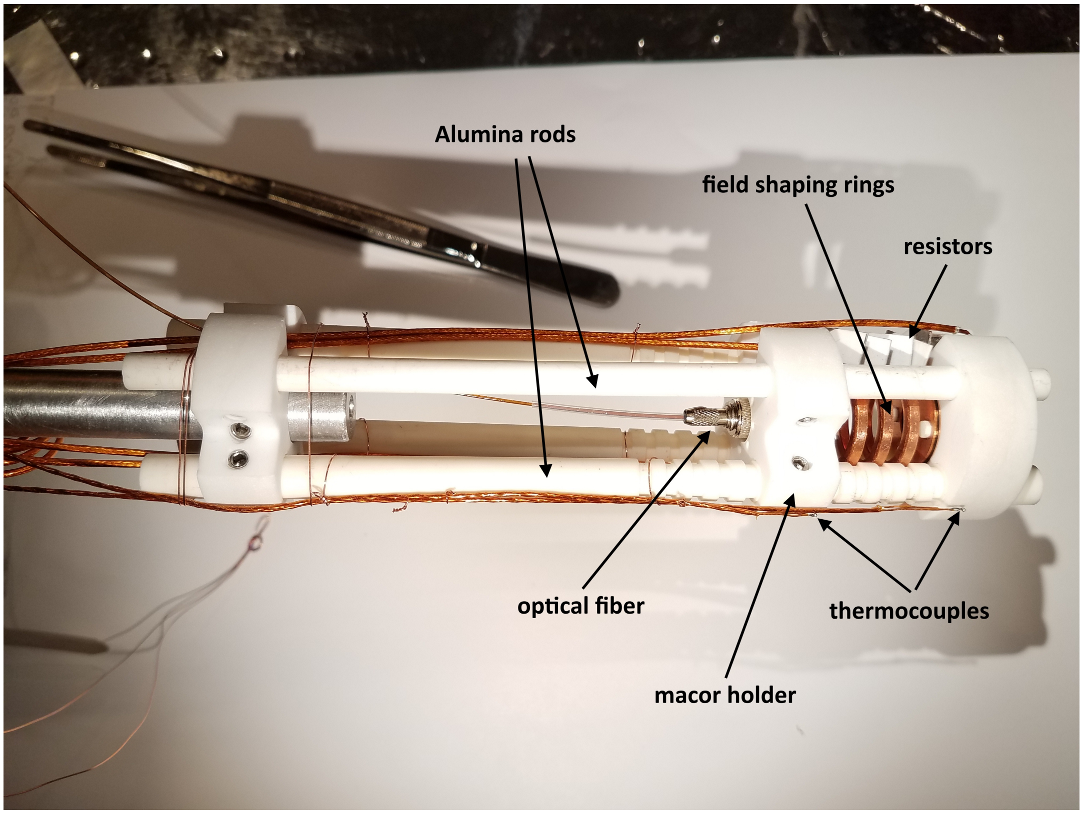

Figure 6.4: Picture of the drift stack. The upper macor holder is held against the aluminum rod via set screws.

holder with ceramic screws (figure 6.5). To ensure the uniformity of the drift field, field shaping copper rings (2 mm thick, 21.3 mm outer diameter, 15.7 mm ID) are spaced 5 mm apart (center-to-center) between the cathode and the anode. The rings are precisely locked in place by four slotted alumina rods (figure 6.4). The drift distance can be modified by adding or removing field shaping rings as needed and by shifting the cathode and anode assembly. A series of 1 GΩ cryogenic- and vacuum-compatible resistors electrically connect the photocathode, the field shaping rings, and the grounded anode mesh. A 300 μm thick Kapton spacer disk is sandwiched between an (anode) mesh and the anode. The bias voltage of +300 V is applied on the anode disk for the collection of drifted electrons. The anode mesh is a 70 lines/inch x-y grid mesh and is mounted onto an identical 250 μm thick phosphor bronze disk with an ID of 8 mm, and all three components are secured by ceramic screws to another macor holder at the bottom of the drift stack. Due to the low thermal expansion coefficients of macor and alumina the change in drift distance (and hence the drift field) with temperature is negligible. The field between the anode and anode grid, the collection field, is kept constant at 10 kV/cm; the collection efficiency flattens for fields above 5 kV/cm (see figure 6.40). The alumina rods extend past the drift region and connect to a third macor plate which is fastened to an aluminum rod hanging from the top flange (see figure 6.4) with set screws.

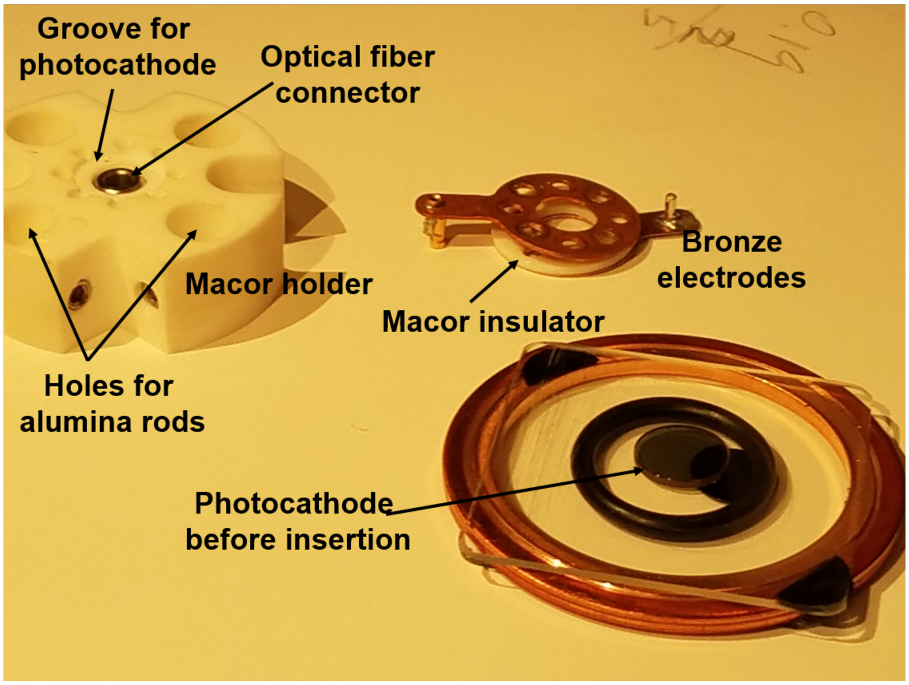

Figure 6.5: Photocathode assembly.

To perform quantum efficiency measurements as described in section 6.7, an identical 70 lines/inch grid was added at the cathode. The grid is mounted on another phosphor bronze plate (on the side nearest the cathode) and separated from the cathode by a 1 mm thick macor insulator (see figure 6.6). The macor thickness was chosen to cancel out microphonics noise which we observed when first adding the cathode mesh and using a kapton piece similar to the one at the anode. The extraction field between the photocathode surface and the cathode/upper grid is always half the drift field. This is done to ensure optimal transmission through the grid (discussed in a later section. See figure 6.7).

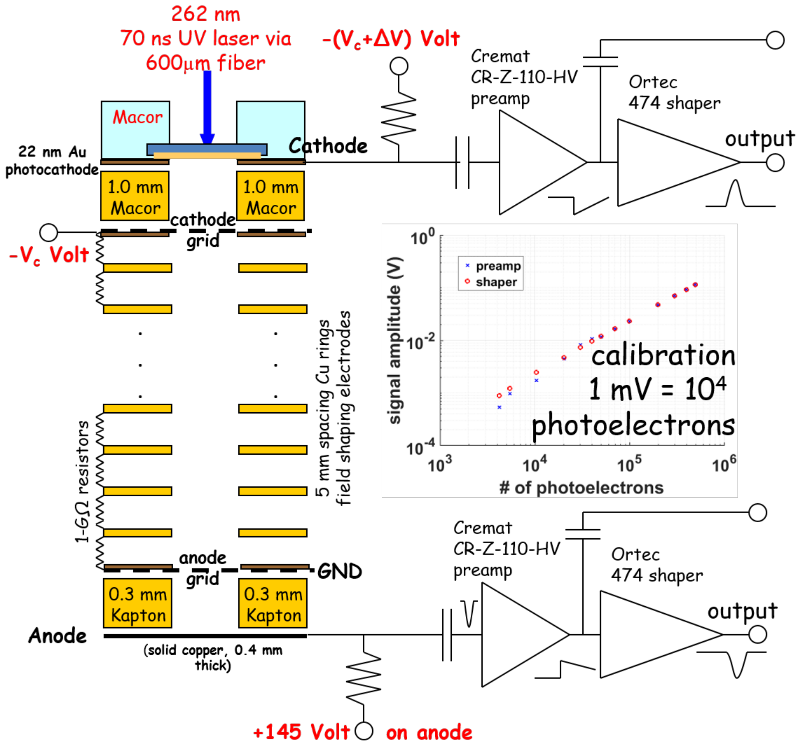

Figure 6.6: Schematic diagram of the drift stack. A uv laser back-illuminates a gold photocathode via a 600 micron fused silica fiber. An upper and a lower mesh define the drift region, where a uniform drift field is maintained with the help of copper field shaping rings. The electron signals are collected with the charge-sensitive preamplifier. The calibration for the preamplifiers is shown on the right.

The xenon is liquefied by immersing the cell in a cold ethanol bath at 155 K (discussed in detail in the next section). The K-type thermocouples are mounted one near the anode and the other near the cathode, to monitor the temperature of the liquid; they also serve as de facto level sensors during the initial fill-up; when the drift region is completely filled with LXe both thermocouples will read the same temperature. Figure 6.8 shows a picture of actual liquid xenon in the early stages of a run in December 2015.

The thermocouples used in the setup are k-type and were purchased from Accu-Glass. They

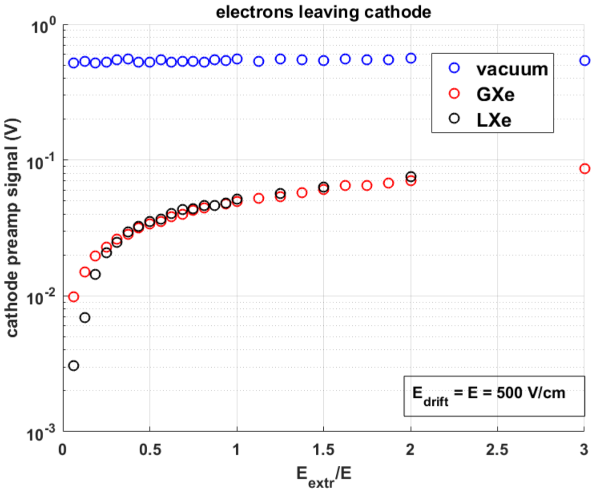

Figure 6.7: Cathode signal vs extraction field in a semilog plot.E_{extr} is the extraction field and E = E_{drift} is the drift field. The transmission does not saturate because the quantum efficiency steadily increases with the extraction field (see section 6.5). However we use a field ratio of 1:2 (see section 6.5)

Figure 6.8: A picture of LXe taken through the viewport. One can see the formation of solid on the surface.

are kapton-insulated. The thermocouples do not perform well at extremely low temperatures. We found that they read -77.9°C at dry ice temperature (actual value -78.0°C), -181.4°C at LAr temperature (actual value -185.3°C) and -190.1°C at LN_2 (actual -196°). The thermocouples are more reliable at higher temperature. Hence a correction is applied to our temperature readings based on these calibrated measurements.

6.2.2 Gas handling system

The xenon recovery line was built over a period of 9 months. Its main purpose is to ensure xenon is fully recovered after each run. The entire line is made of 1/4” stainless steel pipes and valves connected through VCR seals. All valves were acquired from Swagelock and are rated for ultra-pure gas handling. We cut and bent the pipes which were then welded by the BNL machine shop and ASME certified. The entire recovery line is attached to and supported by 80”-by-60” 5” thick aluminum plate. The aluminum plate’s surface was sanded and made rough to reduce the chance of straight laser beams reflecting off it and causing injury to people in the lab.

Figures 6.10-6.13 show the recovery system from conceptual design to implementation. It is composed of 2 stainless steel cylinders, 17 stainless steel valves, a cold trap, and a purifier. The cylinders are identical 3.8 L cylinders from Cryofab. The bottom openings were welded at BNL machine shop. The integrity of the welds was tested by repeatedly immersing the cylinders in LNe and then checking for leaks which a Helium leak detector. Both cylinders passed the required testing. The tops of the cylinders are mounted with cga valves and 2100 psi burst discs.

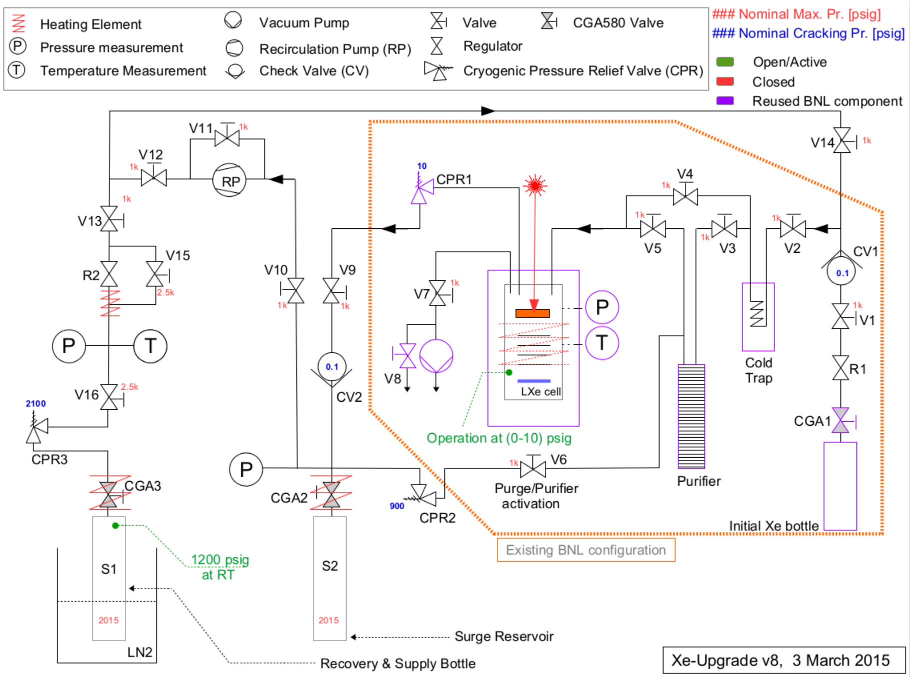

Figure 6.9: Xenon recovery diagram. Initial drawings from the planning stages.

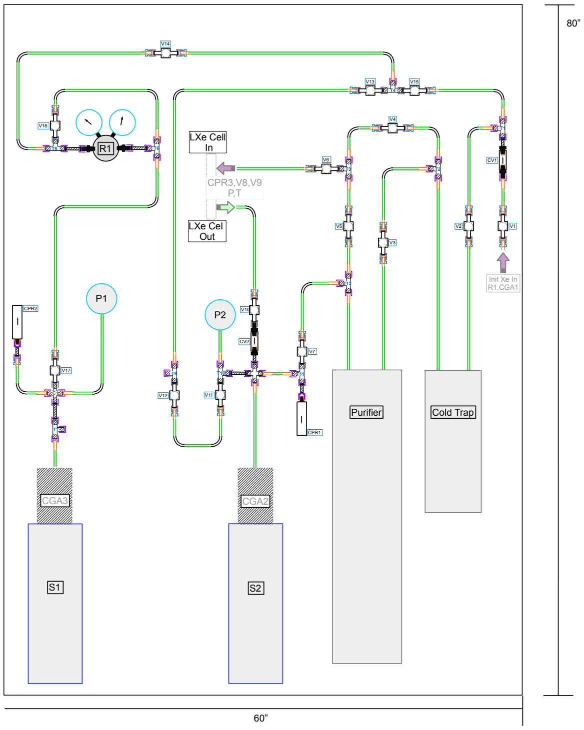

Figure 6.10: Xenon recovery line. CAD drawing.

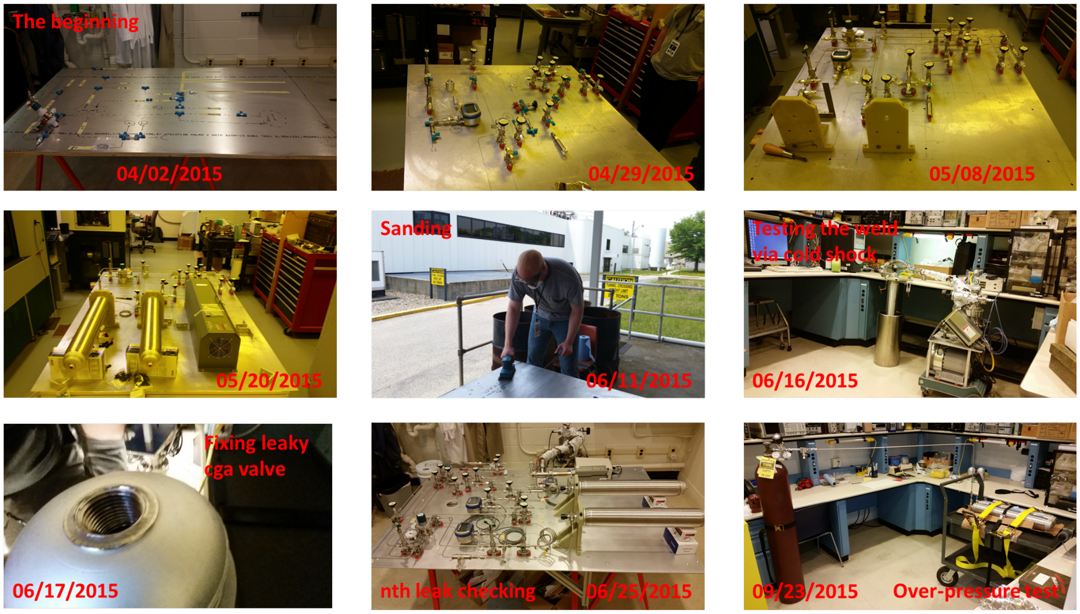

Figure 6.11: A brief history of the construction the recovery system.

The whole assembly was systematically tested for leaks using a Helium leak detector and was found to be leak tight to the level of 10^{-10} Torr. The system is also certified by BNL safety

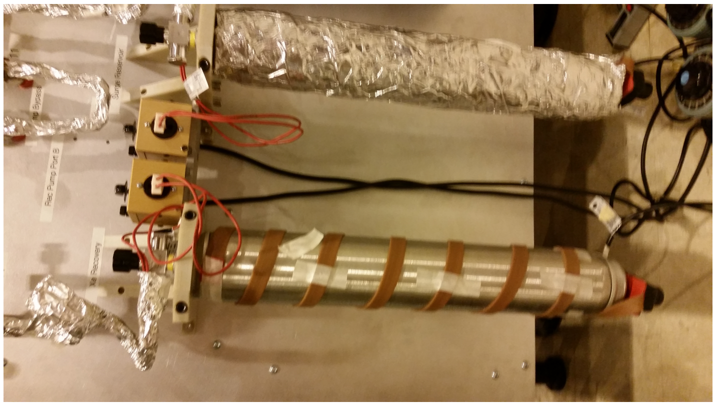

Figure 6.12: Baking the gas cylinders before initial use. These are the largest surface areas in the system and required longer initial bake-out.

Figure 6.13: Ready to go. September 28, 2015.

office as a high pressure gas system and is rated for pressures as high as 2100 psig. Before commissioning, an over-pressure test was conducted at 1800 psig and the assembly was found to maintain its integrity, i.e. a pressure 1800 psig was maintained for an hour and no leak was subsequently detected with a helium leak detector. Before the first xenon run the entire line was flushed with xenon and then baked at 100°C for a week while being continually pumped on with a turbomolecullar pump.

There are two separate turbo pumps, one for pumping the cell and the other for the recovery line; this is done to ensure the water and other residues caught by the cold trap can be pumped out directly without going through the LXe cell. The turbo pumps (TwisTorr 304 FS CFF6) were purchased from Agilent Technologies and assembled into compact pumping carts (see figure 6.14) including scroll pumps at BNL by our group.

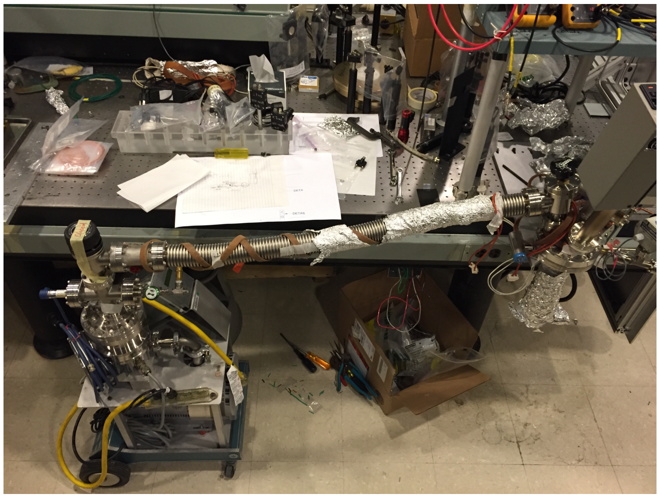

Figure 6.14: Pumping cart.

The recovery line also has a regulator for controlled feeding of gas into the cell, two pressure transducers for monitoring pressures in the cylinders, 2 pressure relief valves, two check valves to facilitate unidirectional flow of the gas in certain sections of the system, a dedicated port for a planned recirculation pump, and an open port for interfacing with other gas/vacuum system if ever needed.

6.2.3 Laser system

The photon source is a frequency-quadrupled, 4.73 eV, 71 ns pulsed Nd:YLF laser operating at 100 Hz repetition rate (figure 6.1). The pulsed UV photons are coupled into a 4 m long 600 μm diameter solarization-resistant UV fused silica multi-mode optical fiber with a numerical aperture (NA) of 0.22. This fiber is then coupled in the cell to a 0.35 m long fiber of identical characteristics via a vacuum optical fiber feed-through of similar characteristics. The 4 m long optical fiber was purchased from Thorlabs, and the vacuum portion was assembled by our group, i.e. a special connector was designed to screw into the macor and the fiber connector was glued and cleaned by us before use.

The in-vacuum fiber directly contacts the back surface of the sapphire disk (figure 6.5). The laser light can then back-illuminate the Au photocathode, releasing photoelectrons (photoelectric effect) into the LXe, where they drift along the lines of a uniform electric field. The maximum laser energy deposited on the surface of the photocathode is $\sim$0.64 μJ; this corresponds to an energy density of 0.8 μJ/cm^2, far below the measured 6 μJ/cm^2 damage threshold of the thin gold film. The overall fiber transmission in the UV is $\sim$30%. Therefore, after taking account of the $\sim$50% attenuation of the photocathode (sapphire plate), the optical throughput of the fiber to the (back) surface of the photocathode is $\sim$15% at UV wavelengths.

We also have at our disposal a 266 nm, 60 ps pulsed Nd:YAG laser operating at 1kHz and a 248nm 7ns pulsed (KrF) Excimer laser at 24Hz. Both of these lasers were used in our study of multiphoton ionization.

6.2.4 Electronics and DAQ

Charges arriving at the anode are fed to a BNL IO535 or a Cremat-CR-Z-110-HV charge sensitive preamplifier followed by an Ortec 474 timing filter amplifier with 100 ns peaking time. (Unless otherwise noted, all the data discussed from here on were acquired with the Cremat preamp). Preamplifier and amplified shaped signals are both recorded on a 5 GS/s Agilent digital oscilloscope. All trigger starts from the output of a $<$1 ns risetime fast photodiode that intercepts a small portion of the frequency doubled Nd:YLF green laser beam. The typical number of drifting photoelectrons ranges from 10^6 to 10^7 per pulse at bias fields of 70 to 1000 V/cm and depending on the laser energy.

Figures 6.15 and 6.16 show plots of the BNL and Cremat preamp calibrations, respectively. This measurement is done by injecting known charges from a function generator into the test input of the preamplifier and measuring the preamp and shaper amplifier responses. The takeaway here

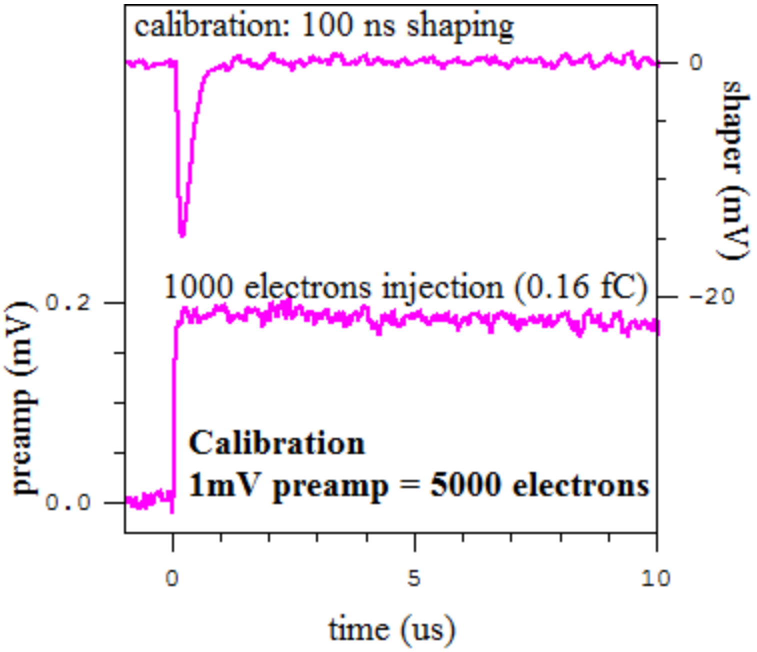

Figure 6.15: BNL IO535 preamp calibration. 1 mV ≈ 5000 electrons.

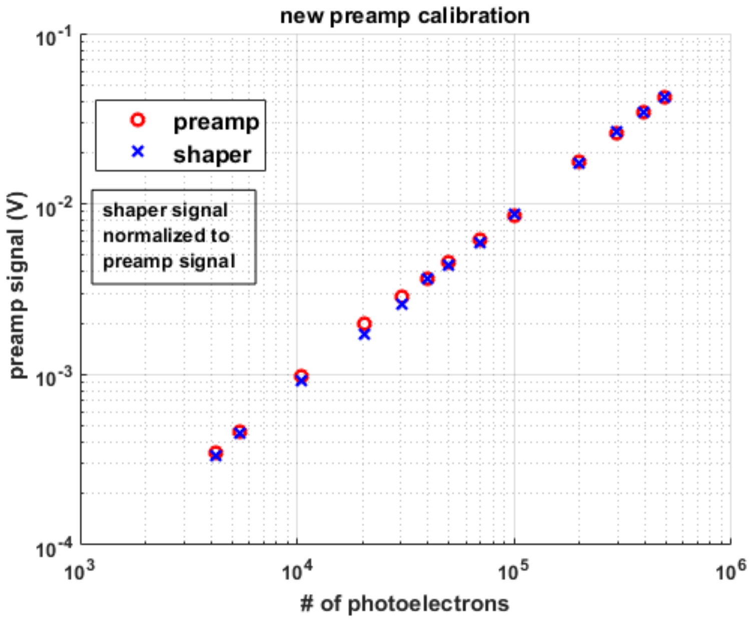

Figure 6.16: Cremat crz-110 preamp calibration. Unlike the BNL preamp 1 mV correspond to nearly 10^4 electrons. Both preamps have very good dynamic range.

is that our preamps have a linear response over three orders of magnitude. We also measured the rms noise to be 300 electrons/mV. The power supplies are from Bertan.

We also log the pressure readings from the transducers through an Omega daq unit (OMB-

DAQ-2408). The DAQ is interfaced with the computer through a Labview program. The temperatures are read and logged with a thermometer from BK precision (BK 715).

6.2.5 Operation

During the first LXe run after the gas handling system was commissioned, GXe was fed from 99.999% pure GXe supply tank. After this initial run Xenon was stored in S1 for future reuse and the supply tank was valved. On a typical run GXe is fed from S1 through a regulator to the dry ice cold trap to remove water vapor, followed by a SAES purifier (Oxisorb filter capable of achieving ppb impurity levels). At the end of each run the xenon is recovered via cryopumping to S1. While there is no active gas xenon recirculation during each run, there is clear evidence that the purity level improves with number of runs on the same batch of xenon gas (figure 6.17).

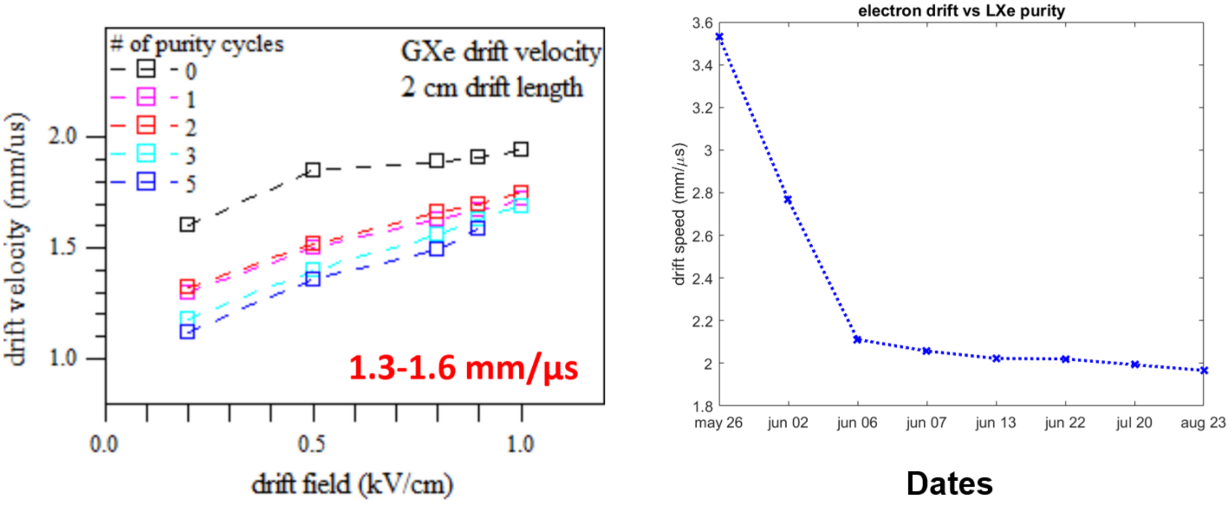

Figure 6.17: Purity as measured by the electron drift velocity improved significantly over the early runs as the xenon was being purified. On the left is the drift speed for GXe as a function of number of runs/purification cycle (12/2015). On the right is the same data for LXe (June 2016). Note that the data gas and liquid data are fom different time periods. The gas data shown were taken with the first iteration of the cell where the drift stack was made of G-10; these are among the first measurements we ever made and these suffered from a number of systematic and purity issues. The liquid data shown are the first taken with the upgraded cell where the drift stack is now made of macor and alumina as described above.

A typical run is as follows:

1. Bake and pump the cell the night before. Twelve hours prior to a run is typically enough to get to good UHV.

2. Turn on and warm up purifier; this takes an hour. Turn off baking. Prepare cold trap (dry ice, -78.5° C). Turn on and warm up laser. All lasers are very stable and beam realignment is rarely needed.

3. Flush cell with 1.5 bar GXe 3 times, 5 minutes each. Prepare ethanol bath.

4. Immerse cell in LN2 as GXe is filled into cell. Monitor temperature and pressure in cell as well as pressure in supply (S1) cylinder. Starting from a full (800 psig) We know that a change of 250 psig will make enough liquid to cover both anode and cathode. And since we don't have a flow meter we try to fill at about 10 psig/minute (experience).

5. Once temperature in cell reaches -30°C, replace LN2 with ethanol (at 150-155 K). 15-20 minutes after the start of filling we see the first sign of liquid, i.e pressure spike and anode temperature at 166 K. The cathode will typically reach LXe temperature 5-7 minutes after this.

6. Once the cathode and anode are at the same temperature, it will generally be another 10 minutes before the electron signal stabilizes and we can start taking physics data. A single bath can maintain constant temperature and pressure for about an hour before we need to replace. Also note GXe is continually fed into the cell to maintain equilibrium. Replacing baths as needed we are able to run 3-4 hours uninterrupted.

7. At the end we immersed S1 in LN2 and slowly cryopump the xenon back into S1.

8. We then pump and bake the cold trap.

One of the difficulties of working with LXe is that xenon is liquid in a very narrow temperature range if one wishes to operate in a pressure window close to atmosphere. In our case this was almost a must because of the glass window. Figure 6.18 shows the phase diagram of LXe. We calculated this diagram using the REFPROP software from NIST [87]. Operating in such a narrow window and one so close to the triple point made it difficult to run in stable conditions, i.e calm LXe surface (sign there are no bubbles that could capture electrons in the column). We eventually achieved stable operation by running in a pressure range of (-2 psig to 0 psig) and a temperature range of (-111°C to -109°C).

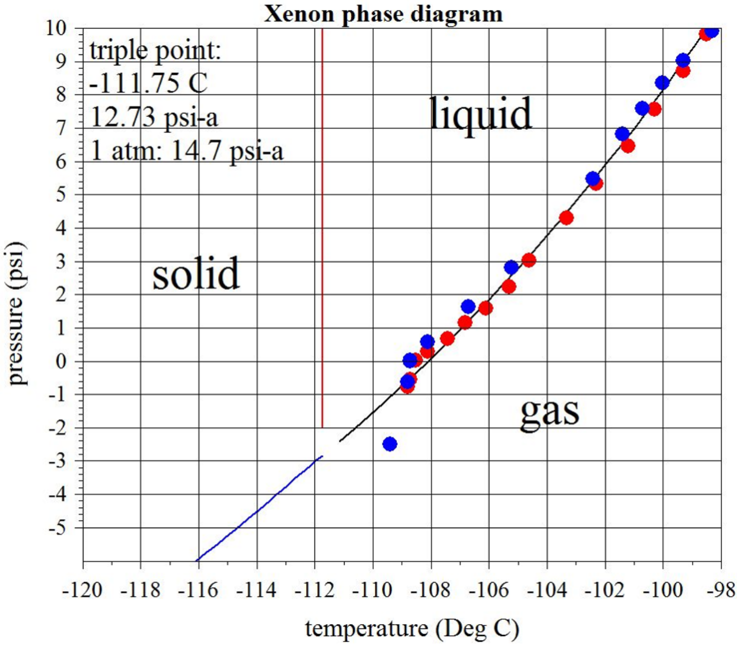

Figure 6.18: Xenon phase diagram calculated using the REFPROP software from NIST [87]. This plot shows representative datasets where the LXe is allowed to slowly warm up. As this happens we straddle the phase boundary between liquid and gas. The blue and red dots represent two separate datasets from two different days. Typical runs take place at -2 psig and -111○C. This is very close to the triple point but for us it is the most stable place to operate, i.e. calm LXe surface (no bubbles).

In the early stages of the experiment we noticed that drift times were much faster than expected. Furthermore we struggled to maintain a stable signal for even 45 minutes. These pointed to impurities in the LXe. To remedy this we redesigned the cell (as already alluded to) from G-10 parts to alumina and macor. We also removed teflon parts in favor of kapton. Furthermore the resistors originally had some unknown coating/painting the vacuum properties of which were unclear. This paint was removed using acetone. All these upgrades led to a improved and more stable electron signal.

We also had unambiguous signs of LXe ionization, i.e. instead of a single spike at a specific delay we saw a spike sitting on a gradually increasing background. This background was indicative of charges being created in a column along the laser direction of travel, resulting in charges at all drift times up to the delay of the true photoelectrons from the photocathode. This is discussed in details in section 6.6. To remedy this problem we moved from the original Nd:YAG laser to the Nd:YLF laser. Unless otherwise stated all the data shown in the remainder of this chapter were acquired with the Nd:YLF laser.

6.3 Waveform processing and analysis

Figure 6.19 shows a typical raw preamplifier trace. ’Time-zero’ is dictated by the laser pulse trigger. The small signal charge rise near t = 0 is due to some non-negligible photoelectrons being generated at the anode grid, a consequence of operating the photocathode in transmission mode as this inevitably results in $\sim$50% laser light penetrating through the photocathode to the drift region. Consequently this signal does not depend on the drift field and can be turned off by reducing the laser intensity see figure 6.20; it is a background to be subtracted, as is discussed in the next section (6.4).

The dominant step in the preamplifier signal occurs when the photoelectrons originating from the photocathode are collected by the anode. The time delay of the step and its risetime correspond to the drift time and the width of the electron bunch, respectively. In the absence of longitudinal diffusion, this step would have a fast risetime limited only by the response of the preamplifier convoluted with the initial electron bunch temporal width, which is dictated by the laser pulse width. The slow exponential decay ($>100\mu$s) is due to the RC time constant of the preamplifier (>150 μs).

The slowly rising signal on figure 6.19 between 0.1 μs and the arrival time of the electrons at the anode is an additional background signal. We believe this signal is induced charges on the anode due to the drifting photoelectrons; it is common in Frisch grid assemblies. Under ideal conditions

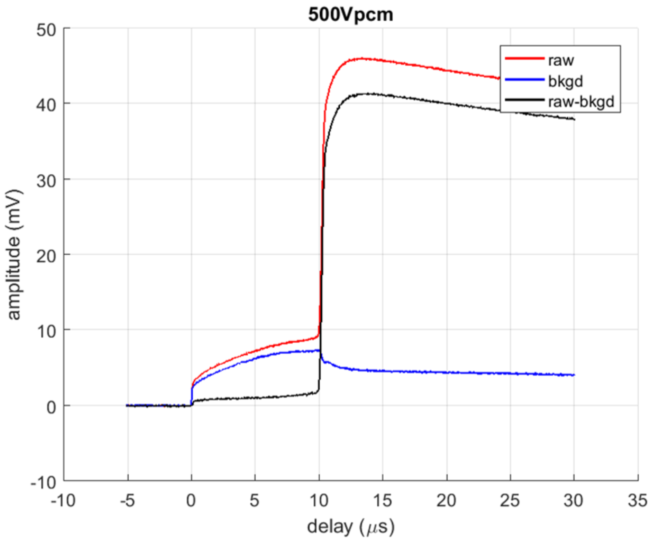

Figure 6.19: A representative preamplifier photoelectron charge signal trace. The drift field is 500 V/cm. The raw trace (red) is shown along with the background (blue) and the background-subtracted (black) signal used for analysis.

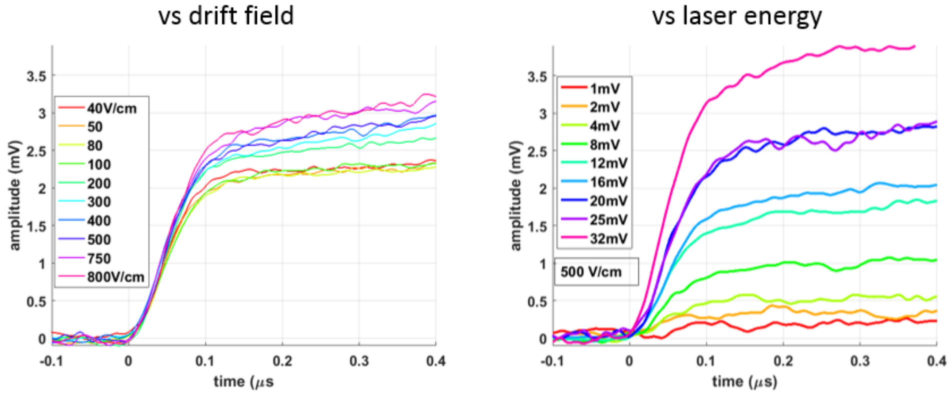

Figure 6.20: Anode grid background. On the left it is shown there's no dependence on drift field for the amplitude. It is however laser energy-dependent, as expected, and can be turned off by going to low laser energies.

the grounded anode grid should prevent the anode from seeing any drifting charges until the later cross the grid. However no grid is perfect and in fact our grid is mostly empty space and thus cannot be treated as an infinite plane at some constant potential. We discussed this background further in the next section (6.4) on systematic errors.

This background signal can be reliably reproduced by setting the anode bias to 0 V; when this is done no electron from the photocathode should drift past the grid into the collection area (figure

6.21 shows field lines for this configuration). We can thus subtract this background from the raw trace and obtain the true photoelectron signal. However some characteristics of this background are not intuitive and we carried a number of studies to decipher it (see section 6.4). This background is present in both gaseous and liquid signals and is not dependent on laser intensity which means it cannot be multi photon ionization of the xenon. Nevertheless, as we'll show in the next section (6.4), subtracting this will only add a small manageable uncertainty to our final measurements.

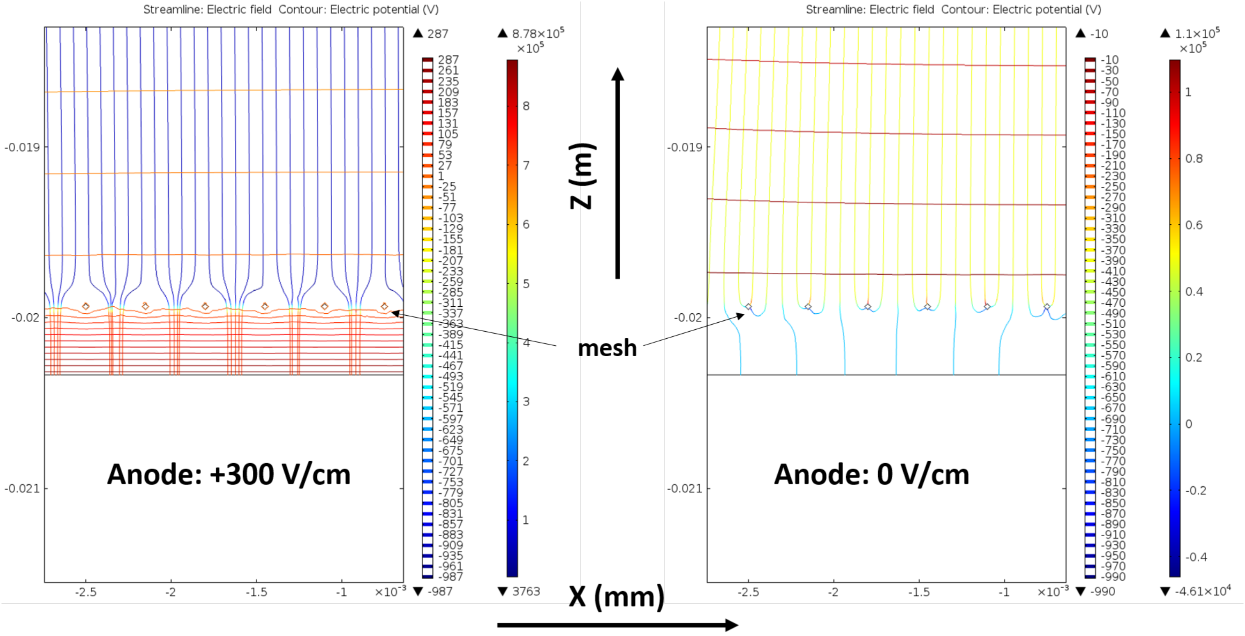

Figure 6.21: Simulated field lines in the drift and collection regions surrounding the anode grid when the anode is set to +300 V bias (right) and 0 V bias (left). In both cases he drift field is 500 V/cm. and the anode grid is grounded. Simulations were carried out using the Multiphysics package from COMSOL.

Figure 6.22 shows a set of background subtracted preamplifier signal traces and their corresponding shaping amplifier traces taken at various drift fields. It shows that decreasing drift fields are accompanied by increased drift times and slower risetimes. The reduction in signal height with lower drift field is the result of both decreased quantum efficiency (section 6.7) and drop in the electron lifetime in LXe at lower electric fields (section 6.5).

To simplify the analysis we differentiate the preamplifier traces before fitting them. Figure 6.23 shows a differentiated preamp trace. This is analogous to the operation the shaping amplifier

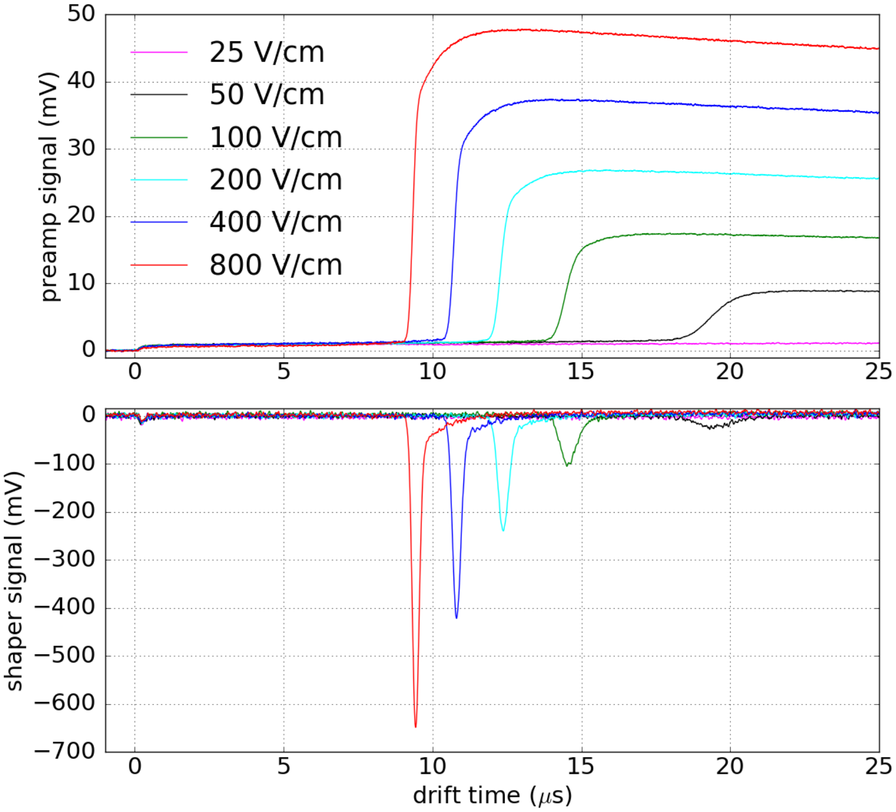

Figure 6.22: A representative set of background-subtracted traces taken at different drift fields. The top panel shows the the preamplifier traces. The bottom panel shows the shaping amplifier traces.

performs and we reproduce this step so that both the preamplifier signal and the shaped signal can be fitted with the same functional form and can be compared directly for consistency. The differentiated preamp signal and the shaped signal, whose peak and width correspond to the drift time and longitudinal diffusion, are fitted with

$$f(t, \sigma, \tau, A) = A \times \exp(\frac{-(t - t_0)}{\tau}) * \exp(\frac{-(t - t_0)^2}{2\sigma^2}). \tag{6.1}$$

It is a convolution of a Gaussian function approximating the temporal width of the electron cloud and a damped step function that represents the preamplifier response. Here A is a normalization factor, t_0 is the drift time, σ is the width of the Gaussian (from which the diffusion information will be extracted). The fits are set to minimize the reduced chi-squared (see figure 6.24). τ is kept constant for the gaseous and LXe signal fits and is calculated from fits to the vacuum signal.

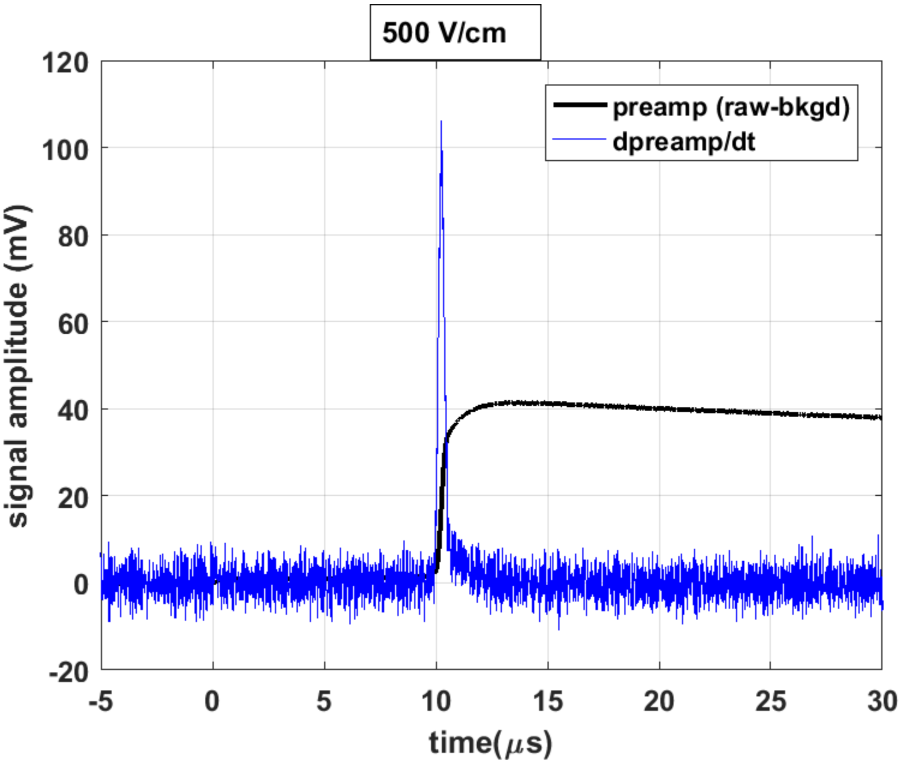

Figure 6.23: A differentiated preamp trace.

We use the vacuum data to calibrate the electronics response. This is motivated by the fact that there is no drift time in vacuum, i.e. the charges arrive at the anode instantaneously for all practical purposes. This means that the risetime of the vacuum signal is solely due to the electronics response and perhaps the laser time duration. Furthermore this is a more ideal way of calibrating the preamp since all the capacitances relating to wires and the cell are connected whereas they wouldn't necessarily be in a normal calibration with the function generator. We fit the vacuum signal with equation 6.1, where τ is also a free parameter. From these vacuum fits we calculate the vacuum risetime to be 30±2 ns, independent of the drift field. The error in the risetime is computed from statistical variations between numerous runs.

The signal time delays are calculated by subtracting the vacuum delay from the t_0 values obtained from fitting the gaseous and liquid signals. A comparison between the delays obtained

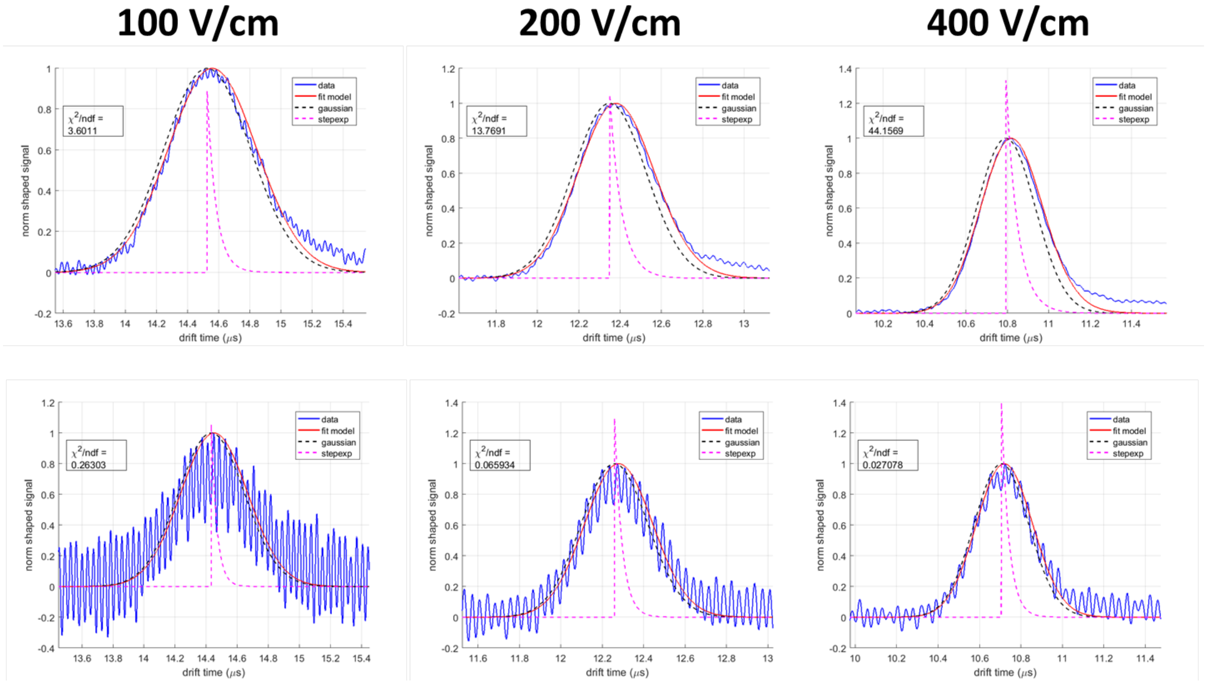

Figure 6.24: Some fits.The top row are shaping amplifier signals. The bottom row are differentiated preamplifier signals.

from fitting the preamplifier and shaper signals reveals they agree within 0.5% (see figure 6.25).

We obtain the signal widths by subtracting the vacuum risetime from σ in quadrature. Values obtained from preamplifier and shaper fits differ by only 3%. Figure 6.26 shows a plot of widths vs fields for the preamplifier and shaper signals. The discrepancy is likely due to the method of differentiation: the shaping amplifier is sensitive to a range of input frequencies. Our straightforward differentiation of the preamplifier signal suggest the presence of high frequency noise (which the shaping amplifier automatically filters); this high frequency noise can skew the fits toward producing narrower widths than the actual values.

We can deal with this high frequency noise by either smoothing the data or applying a Fourrier filter to the differentiated trace to cut out this noise. The first method has the effect of broadening the signal which can lead to an overestimate of the true width.

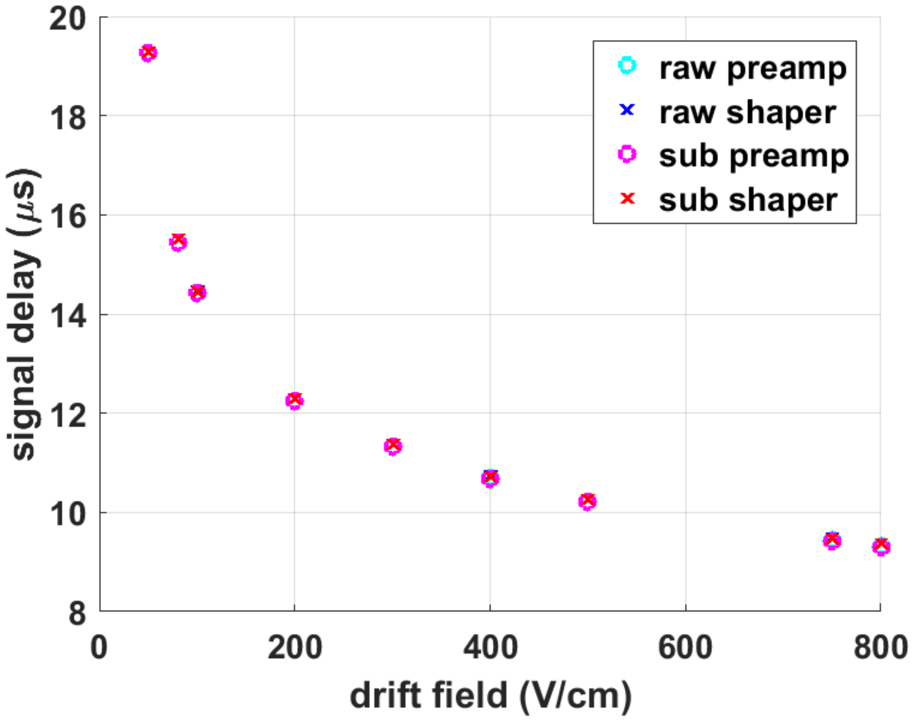

Figure 6.25: A comparison between signal delays obtained from fitting shaped signal to those obtained from fitting preamp signal. Both subtracted traces and raw traces are included. A discussion of the background subtraction follows in the next section.

6.4 Systematic errors

There are numerous sources of systematic errors, summarized in table 6.1. The largest systematic error contribution to the drift time comes from the the additional drift between the anode grid and the anode. The collection field is 10 kV/cm and at this field the drift speed can be as high as 3 mm/μs [88] resulting in an additional drift time of 0.1 μs. The error from this ranges from 0.4% to 1.2% depending on the drift field. In the case of the signal width, the largest systematic error contribution (5.9%) comes from the background subtraction. The raw traces (red in Figure **??**) and the background subtracted traces (black in Figure 6.19) are analyzed concurrently and the difference in results is quantified as a systematic error; this is done as a result of our incomplete understanding of the background and to ensure that its effect on the real signal is taken into account.

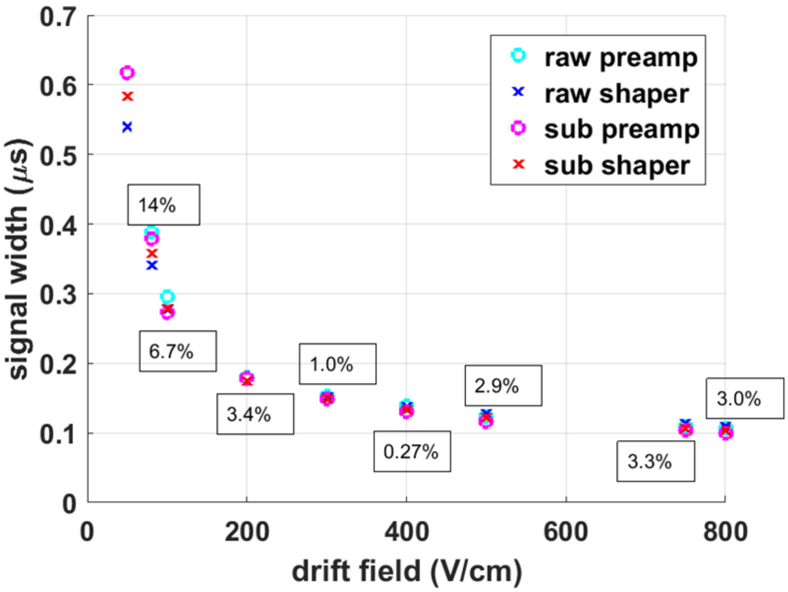

Figure 6.26: A comparison between signal widths obtained from fitting shaped signal to those obtained from fitting preamp signal. Both subtracted traces and raw traces are included. A discussion of the background subtraction follows in the next section. The percentage difference shown is for raw traces.

Error source	Delay (μs)	Width (μs)
Background subtraction	0.1%	5.9%
Laser energy	0.2%	0.3 ns/mV
Shot to shot	0.11%	2.8%
Temperature	35 ns/K	0.6 ns/K
Fit range	0%	0.5%
Anode grid to anode drift	0.4-1.2%	na
Total	**1.4%**	**7.28%**

Table 6.1: List of systematic uncertainties impacting the measured signal delay and width.

6.4.1 Understanding the background

We define background as the signal measured when the cathode is biased while the anode (and the mesh) is kept at ground. The motivation for this is that the electrons drifting in this scenario cannot cross the mesh since there is no applied collection field and any signal observed as a result of their presence must be some kind of induction (see figure 6.21). This induction would also be present when we are in collection mode (biased anode). As was shown in figure 6.19 this signal has a similar shape to the background in the raw amplifier trace suggesting they must have the same source and in principle it makes sense to subtract it. However simulating this signal proved challenging. We thus resorted to treating it as a systematic uncertainty and we quantified its effect on the two measured quantities, namely the signal delay and width. This error is then propagated to other derived quantities (drift speed, diffusion coefficient). To this end we performed a number of studies.

Effect of background subtraction

We performed analysis of the raw traces and compared that to the result obtained with that of the subtracted trace. This was briefly discussed in the previous section (6.3). The results are summarized in figure 6.27. To be conservative we select the largest deviation as the overall error for all drift fields; this is a value of 5.9%.

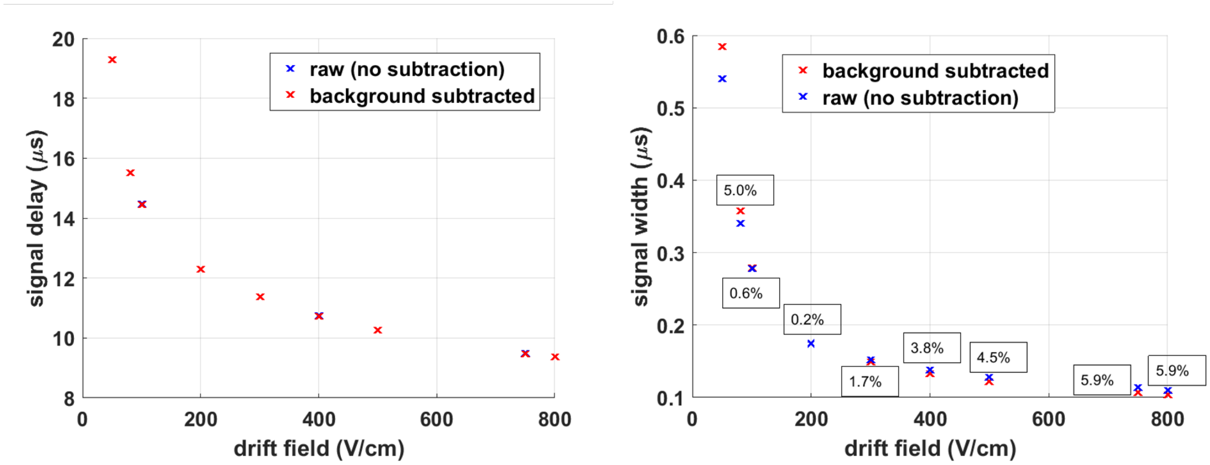

Figure 6.27: Signal delay (left) and width (right) for different background subtraction schemes. Drift field 500 V/cm. We use values obtained from fitting shaped traces. As we showed in figure 6.25 and 6.26 the shaper and preamp values only differ by $\sim 3\%$.

Field and laser energy dependences of the background

This background increases with drift field but the shape mostly remains the same. An exponential fit to this signal reveals that the small signal at t = 0 is constant with drift field and grows linearly with the laser energy, indicating that it is most likely due to the laser generating charges from the mesh or the cathode itself. The portion of the background that grows with delay also has a drift characteristic which remains unchanged with drift field or laser energy.

E (V/cm)	a	b	c	c+a
100	-1.55	0.22	3.86	2.31
200	-3.14	0.20	5.58	2.44
400	-4.90	0.21	7.37	2.47
500	-5.59	0.22	8.02	2.43
800	-7.56	0.22	10.1	2.54

Table 6.2: Background signal vs drift field at 25 mV laser energy (1 mV = 25.4 nJ). The background is fitted with $a \times exp(-b \times t) + c$. The parameter b is a drift characteristic which remains constant. $c + a$ is the amplitude of the step near t = 0 and is constant with drift field.

Laser energy (mV)	a	b	c	c+a
1	-0.38	0.20	0.49	0.11
2	-0.54	0.25	0.83	0.29
4	-1.05	0.22	1.52	0.47
8	-2.14	0.21	3.08	0.94
16	-4.06	0.21	5.83	1.74
32	-7.93	0.21	11.3	3.37

Table 6.3: Background signal vs laser energy (1 mV = 25.4 nJ) at 500 V/cm drift field. The background is fitted with $a \times exp(-b \times t) + c$. The parameter b is a drift characteristic which remains constant. $c + a$ is the amplitude of the step near t = 0 and is directly proportional to laser energy.

6.4.2 Systematic due to laser intensity and energy

The initial size of the electron cloud as it leaves the photocathode is dependent on the laser pulse duration used. We can see this when different lasers are used (figure 6.29). Figure 6.29 suggests there is no systematic effect due to the choice of laser.

We also observed a slight dependence on the laser energy with most of the effect being on width (figure 6.30). The fact that the signal width depends on the laser energy implies that the original size of the electron bunch matters. Specifically the more electrons we generate the greater the Coulomb repulsion between them is and must be accounted. This is done by using the zero energy intercept in figure 6.30.

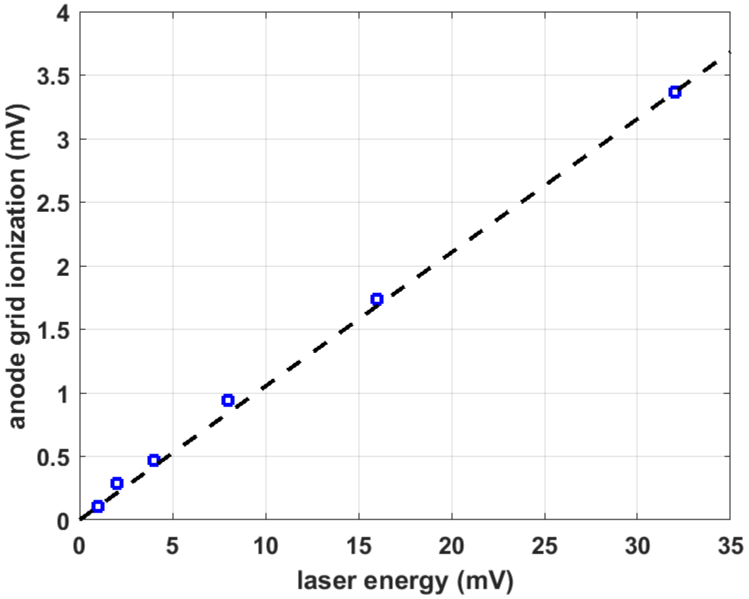

Figure 6.28: Grid signal vs laser energy.

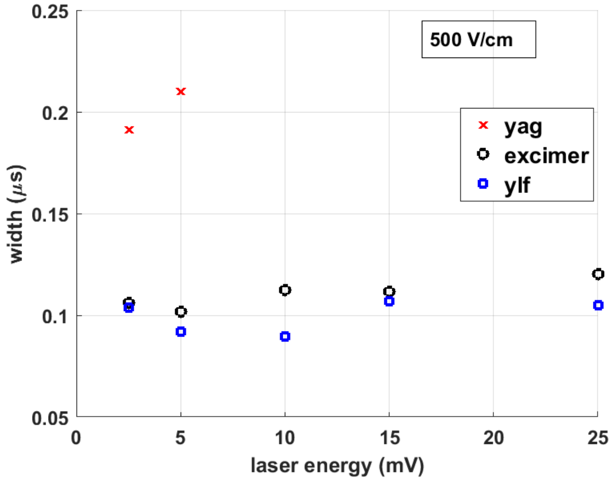

Figure 6.29: Width of the electron cloud derived from fitting the preamp risetime for different lasers. In the case of the YAG laser the multiphoton ionization dominates the signal and makes fitting difficult. The excimer (7ns pulse duration) consistently gives a higher width than the YLF(71ns).

The laser energy scan in figure 6.30 was performed at the drift field of 500 V/cm. For other drift fields a similar energy scan needs to be carried and the zero energy intercept determined. However we originally underestimated this effect and did not have energy scans at other fields. To remedy this we attempted to develop a model for the effect of the Coulomb repulsion at 500 V/cm which

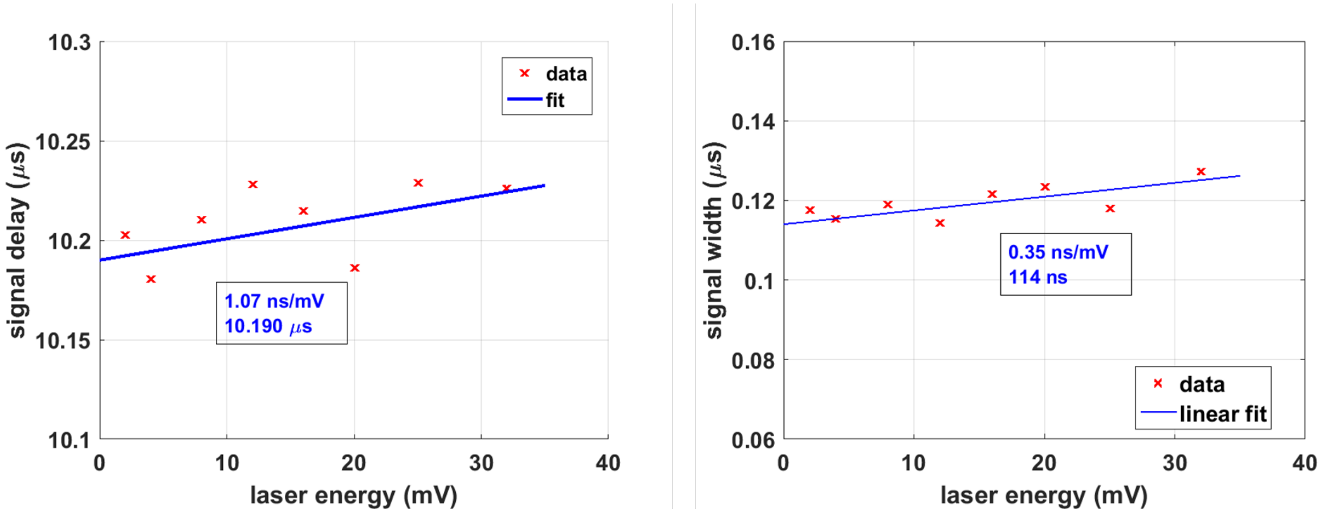

Figure 6.30: Signal delay (left) and width (right) as a function of laser energy for the YLF laser. 1 mV = 25.4 nJ. The drift field is 500 V/cm.

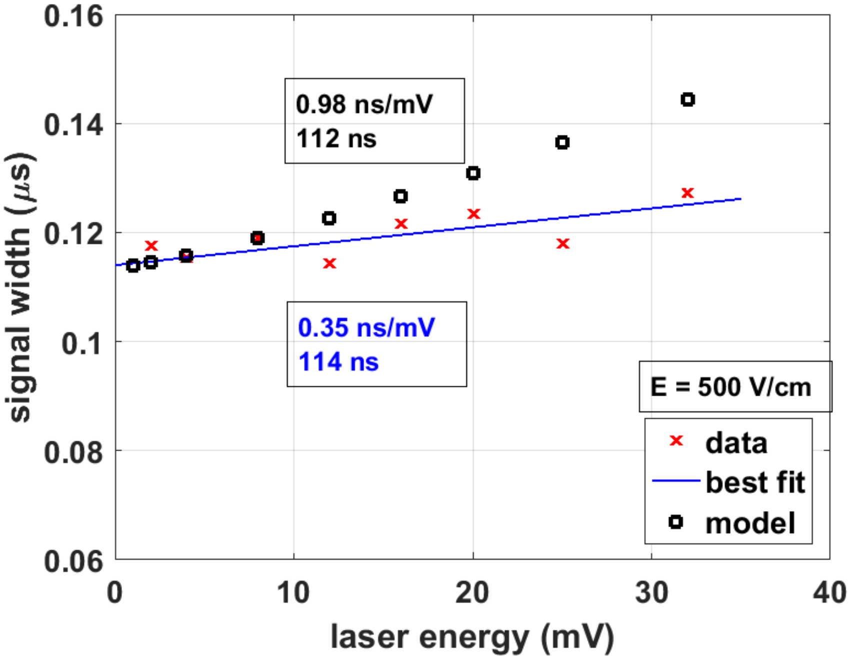

Figure 6.31: Signal width right as a function of laser energy for the YLF laser. 1 mV = 25.4 nJ. The drift field is 500 V/cm. Also shown in blue is a linear fit to the date. The zero-energy intercept is 114ns. The black dots show calculated widths using a model for Coulomb repulsion (section 6.5 and []). The model predicts a stronger dependence on laser energy (0.98 ns/mV) than what we observed (0.35 ns/mV).

would then be used to correct the measured widths at other drift fields. We discuss this in more details in the next section when the longitudinal diffusion coefficient is calculated.

Another source of errors (not systematic) related to the laser is the day-to-day and shot-to-shot laser variations. The laser shot noise was measured to be about 3.1%. However if we measure the width and drift time at the same drift field and temperature (and pressure) over a number of days we only get a variation of 0.11% for the drift time and 2.8% for the signal width.

6.4.3 Temperature

We discuss the effect temperature has on the signal in more details in section 6.5. The temperature gradient between cathode and anode is maintained to always be no worse than 1 K. This has a measurable impact on the signal delay of 35 ns/K and a negligible effect on the signal width as is shown on figure 6.32.

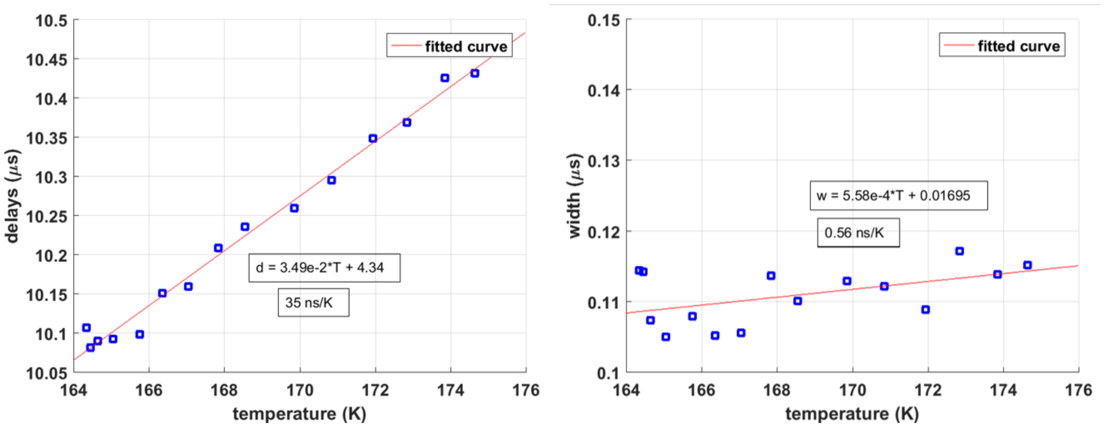

Figure 6.32: Signal delay (left) and width (right) as a function of temperature. Drift field 500 V/cm.

6.4.4 Preamp vs shaper

The uncharacteristic feature observed at the top of the preamp trace makes it difficult to perform a fit with the typical error function. However it is still necessary to analyze the preamp traces and make sure the results are consistent with the analysis of the shaped traces. To this end we first differentiate the the preamp trace to get a current. The shape of this current is nearly Gaussian, as expected. This current is then fitted with the same function as that used for the shaped signal and given by equation 6.1. Interestingly we find that better fits can be achieved if a bi-exponential is used instead of a single exponential but this is not shown in the current thesis. Once the fits are performed the signal delays and widths can be extracted. We find that analysis of the shaped traces and the preamplifier traces yield the same signal delays within 0.5% while the resulting widths vary by only 3.4% or less for drift fields $\geq$ 200 V/cm. At lower fields the difference between preamplifier and shaped traces is as high as 6%. We decided to use the shaper traces for our analysis, electing to add the percentage difference between results from the shaped and preamp traces as a systematic uncertainty. These results were summarized earlier in figures 6.25 and 6.26.

6.5 Transport properties of electrons in gaseous and liquid xenon

6.5.1 Drift speed

The drift velocity is given by

$$v = \frac{d}{t} \tag{6.2}$$

where d is the drift distance and t is the drift time. Here, the drift distance is fixed at d = 20.0 mm to an uncertainty of 0.1 mm between the cathode and the anode grid mesh. The drift distance is set by placing a spacer between the macor holders. The spacer was machined by the SBU machine shop and is 20.87 mm long. The additional 0.87 mm accounts for the combined thicknesses of the kapton insulator, the anode plate and the bronze plate holding the assembly against the macor as well the bronze plate keeping the cathode in place. The drift time is calculated by taking the difference between the arrival time at the anode grid and the starting time at the cathode as described in section 6.3. The starting time is taken as the ”drift time” in vacuum and the arrival time is obtained from the fit to the LXe signal.

Figure 6.33 shows the electron drift velocity as a function of drift field in LXe and GXe. The error bars include statistical (average of multiple runs) and systematic uncertainties. At the standard drift field of 0.5 kV/cm we measure a drift velocity of 1.97±0.04 mm/μs in LXe and

1.42±0.06 mm/μs in GXe. It is evident that the electrons drift faster in LXe than in GXe, in agreement with literature [16, 89, 90, 91, 92]. However, it is interesting to note that the opposite behavior is observed in argon [86]. Furthermore, the drift velocity increases with the drift field in both LXe and GXe.

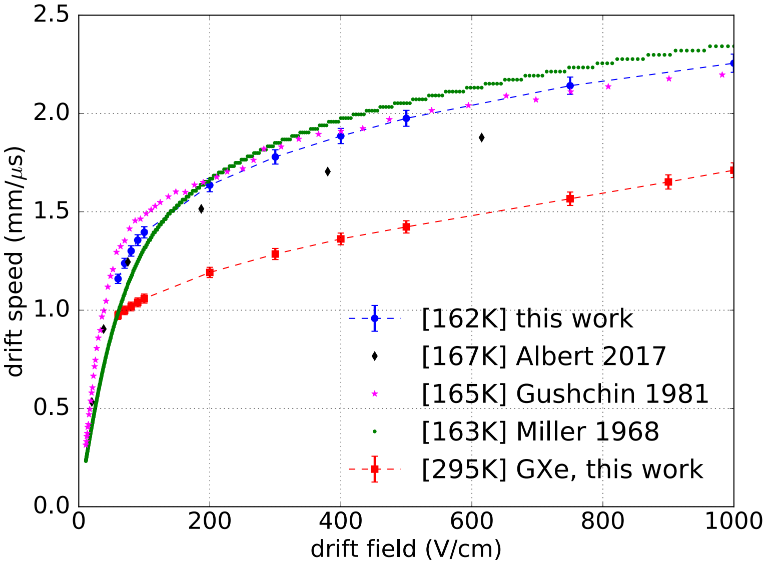

Figure 6.33: Field dependence of electron drift velocity in LXe. The present work is shown in full blue circles with error bars. Other literature values are also displayed. The temperature variation for each measurement is insufficient to account for the discrepancy between reported measurements. Our measurement of drift velocity in GXe is also shown for comparison (full black squares).

A comparison of our measured electron drift speed in LXe as a function of drift field to previously reported measurements [89, 93, 94, 95, 90, 96, 71] is also shown in figure 6.33. The variance in electron drift velocity values in LXe reported in the literature is not well understood. We note, and will show in a later subsection, that the weak temperature dependence of the LXe drift velocity is insufficient to account for the spread in literature values. The purity of the LXe may be the most important factor at play here. As mentioned earlier, we observed gradual improvements in drift velocity during our initial runs (figure 6.17), suggesting a correlation between drift velocity and purity level. In fact, Yoshino [97] and others established the correlation between higher drift velocity and impurities by injecting ∼ppb impurity gas such as butane and methane in LXe.

We also considered the fact that comparably smaller drift regions like ours can suffer from drift field non-uniformities which can lead to longitudinal distortions that effectively lengthen the drift distance. However these distortions would in principle result in slower speeds rather than faster ones. To rule this out in our setup we performed COMSOL simulations of the electric field lines and found that the non-uniformity remains below $\sim$1% at the center of the drift stack (800 μm diameter cylinder); this is shown on figure 6.34.

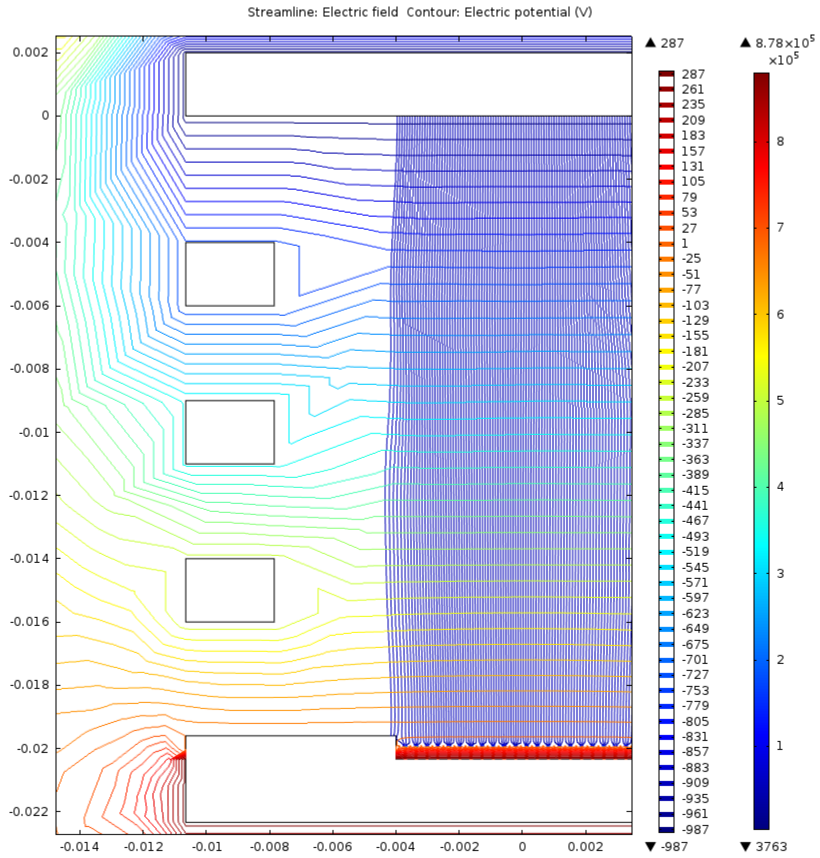

Figure 6.34: Simulated electric field lines inside the small drift cell. In this configuration the drift field is 500 V/cm and the collection field is 10 kV/cm. Both x- and y-axes are in meters.

We also measure drift speeds in GXe find good agreement with literature values. This is shown in figure 6.35, where our measured drift speeds are plotted as a function of reduced field E/N and compared to Pack [91]. Here, E is the drift field and N is the number density. The reduced field (in units of Townsend) ranges from 0.1 Td to 2 Td.

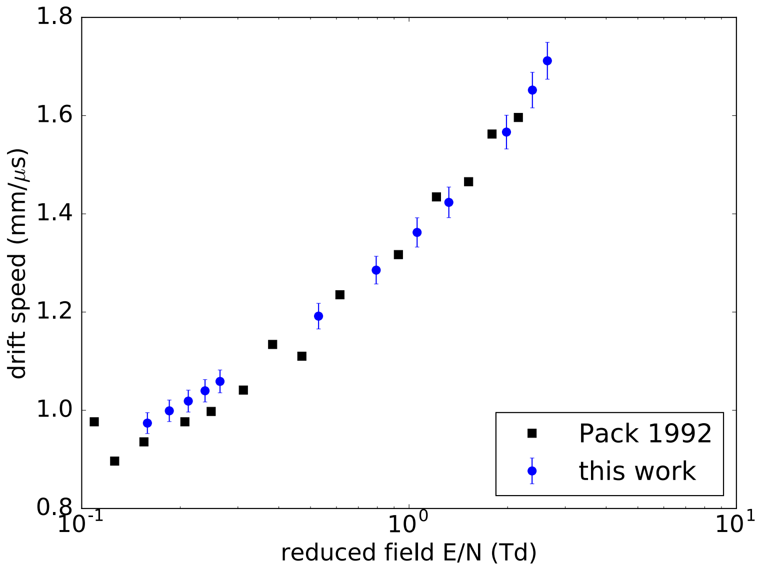

Figure 6.35: Electron drift velocity versus reduced field in GXe. The reduced field, given by E/N is in Townsend (Td) and N is the GXe number density in the cell. Our measurements (blue circles) are in good agreement with those reported by Pack (black squares) [91].

6.5.2 Longitudinal diffusion

A key feature of TPCs is the ability to accurately reconstruct events in 3D. Diffusion, the spread of the electron cloud as it propagates, can complicate the reconstruction accuracy thereby limiting the position resolution of a TPC. A derivation of this phenomenon is motivated in appendix A. While electron diffusion is a random process, it somewhat depends on the properties of the propagating medium and only one other measurement of electron longitudinal diffusion in LXe has been reported in the literature [98]. As the electron cloud propagates, its transverse and longitudinal growths are governed by Fick's law of diffusion (appendix A). One can reduce this effect by minimizing the propagation time, which can be done by (1) applying a high drift field or by (2) shortening drift length. Solution (1) can be problematic as breakdown may occur if the field is too high. Solution (2) on the other hand would limit the volume of the TPC (and hence the source mass) which would be detrimental to the achievable sensitivity. A careful balance must be struck. Transverse diffusion of electrons in LXe has been measured and reported, most recently by EXO-200 [71]. Here, we measured the longitudinal diffusion coefficient D_L which is obtained from solving Fick's equation and is given by:

$$D_L = \frac{d^2\sigma_L^2}{2t^3} \tag{6.3}$$

where d is the drift distance, t is the drift time, and σ_L is the temporal broadening in the longitudinal direction. For a full derivation of D_L see the appendix A. σ_L is defined by

$$\sigma_L^2 = \sigma^2 - \sigma_{vac}^2 \tag{6.4}$$

where σ_{vac} is the intrinsic preamplifier risetime and is determined from the instrument response function to be 32±1 ns. σ is the measured width obtained by fitting the anode preamplifier signal as described in section 6.3.

Figure 6.36 shows the plot of the longitudinal diffusion coefficient in LXe as a function of drift field. At 0.5 kV/cm we obtained D_L = 23.8±4.1 cm^2/s. The error bars include both statistical and systematic errors. The statistical error is computed by taking an average of five distinct runs on different days. Systematic errors were estimated as described earlier.

To the best of our knowledge this is the first reported measurement of the drift field dependence of D_L in LXe. Also shown in figure 6.36 are: a single D_L value from XENON10 at 780 V/cm and for comparison purposes the transverse diffusion coefficient D_T values from EXO-200 and Doke at various fields [98, 71, 88]. It is clear from figure 6.36 that at low fields the ratio D_L/D_T approaches 1, in agreement with prediction from theoretical models [16, 99].

Figure 6.36 contains some incomplete information. What we have measured in figure 6.36 is an upper bound to D_L, hence arrows pointing down. This is because the method by which we generate electrons (laser-driven photoemission) adds an additional systematic effect which we initially overlooked–that is, the Coulomb repulsion of the electrons making up the bunch (section 6.4). The most common way to generate electrons in TPCs is via radioactive sources or cosmic rays. Electrons generated in this fashion are generally sparse and uniformly distributed throughout the detector (or in some precise solid angle depending on the position of the radioactive source).

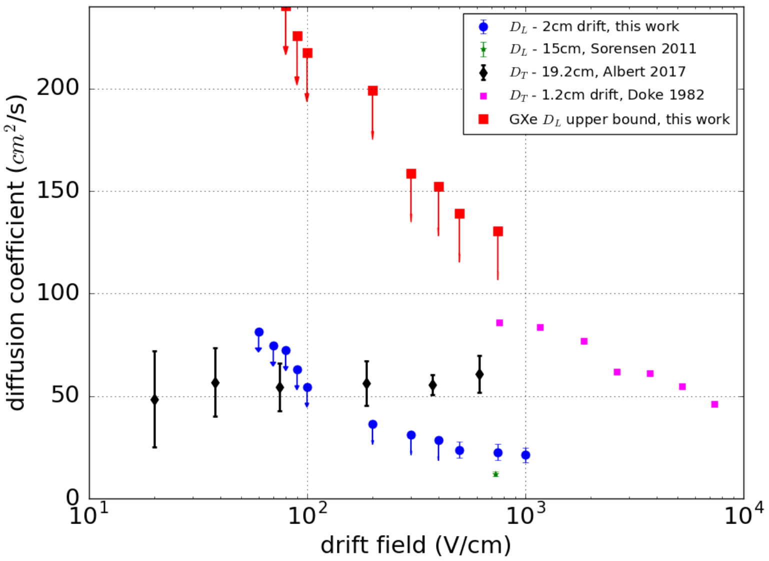

Figure 6.36: Electron longitudinal diffusion coefficient D_L vs drift field in LXe (solid blue circle). Overlaid is a measurement from Sorensen (green stars) [98]. We also show the transverse diffusion coefficient D_T from EXO-200 (cyan) [71], and Doke (black) [88]. At low fields D_T approaches D_L.

Their diffusion in that case is purely Brownian and described by Fick's equation which results in D_L as given by equation 6.3.

In our experiment we generate electrons in bunches of 10^5 or more at a time before they are allowed to drift. Furthermore because of the short laser pulses we use they are densely packed and the Coulomb repulsion may become a significant factor in the growth of the bunch from its initial size to its size at the time of the measurement [100]; this effect can be seen in the laser energy dependence of the signal width (figure 6.30) This suggests that a better estimate for σ (and D_L) is the zero laser energy intercept.

In our earlier measurements we checked for this effect and it appeared to be vanishingly small. However later measurements showed it to be non-negligible. To correct D_L appropriately we would need to perform a laser energy scan at each field for which we are reporting a value for D_L. However we only have energy scans at 500 V/cm (this was done because we erroneously initially determined laser energy to not be a factor). By the time of the most recent analysis (that which uncovered this effect and is reported in this thesis) the LXe cell at BNL had been decommissioned and was in use for a new different measurement. Consequently we were not able to repeat the measurements and can only confidently report the upper bound D$_L$ values in figure 6.36 and the single D$_L$ value for 500 V/cm.

We attempted to build a model for the Coulomb contribution to the measured width. The model is inspired from [100]. It assumes an initial shpheroidal charge distribution where the longitudinal width w$_{para}$(0) is given by the product of the drift speed (v) and the laser pulse duration (Δt) and the transverse width w$_{perp}$(0) is the laser spot size after propagation through the 1 mm thick sapphire plate (on which the photocathode gold is evaporated). The propagation of such spheroid in an electric field is described in [100] and subsequent w$_{para}$(t$_n$) are calculated according to:

$$w_{para}(t_{n+1}) = w_{para}(t_n) + \beta E_{perp} dt \tag{6.5}$$

where dt is the time step from t$_n$ to t$_{n+1}$, β = dv/dE, and E$_{perp}$ is the transverse field arising from the presence of the electrons. We have:

$$E_{perp} = \frac{3Q}{4\pi\epsilon w_{perp} w_{para}} \frac{0.5}{1 + 0.75887\alpha} \tag{6.6}$$

and

$$E_{para}(t_{n+1}) = \frac{3Q}{4\pi\epsilon w_{para}^2}(1 - \frac{1}{1 + 1.542\alpha^{0.35622}}) \tag{6.7}$$

with $\alpha = w_{perp}/w_{para}$. Q is the charge in Coulomb and $\epsilon = \kappa\epsilon_0$ is the permittivity. For LXe we use a value of κ=1.9. The temporal growth of the spheroid due to Coulomb interaction is then determined to be

$$2.355\delta t = \frac{2w_{para}}{v} \tag{6.8}$$

δt is then added in quadrature with the observed zero-intercept value (500 V/cm drift field) to determine the expected signal width. The model has a slope of XX which is always greater than our observed slope. We therefore decided not to use it for the results quoted in figure **??** as further study is warranted.

In the case of GXe, figure 6.37 shows the ratio D$_L$/μ as a function of reduced field E/N, where $\mu = v/E$ is the electron mobility, with v the drift speed and E the electric field. These like in the LXe are upper bound values. Here we measured D$_L$ = 120±18 cm^2/s at 0.5 kV/cm. The values from [91] are overlaid in figure 6.37 for comparison. The overall drift field dependence of D$_L$/μ of GXe are in good agreement with literature.

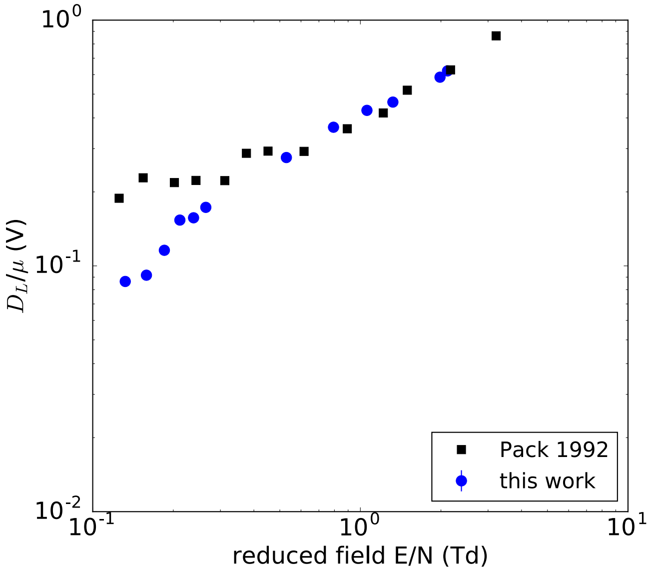

Figure 6.37: GXe D$_L$/μ vs reduced field at room temperature. The reduced field is given by E/N. Results from Pack [91] are shown in black.

6.5.3 Temperature dependence

To quantify the importance of the temperature uniformity inside a LXe TPC, we studied the temperature dependence of the drift speed and longitudinal diffusion coefficient in our small LXe cell. The temperature was varied by simply letting the xenon warm up and making measurements at ∼1 K increments. These results are summarized in figure 6.38. At the bias field of 0.5 kV/cm, we found that the electron drift speed in LXe decreases linearly with temperature at a rate of -0.4%/K in qualitative agreement with previous measurements at various drift fields [101, 88]. These literature values are shown in figure 6.38 for comparison. On the other hand, within our experimental uncertainty, the temperature dependence of D$_L$ in LXe appears to be negligible; this is also shown on figure 6.38.

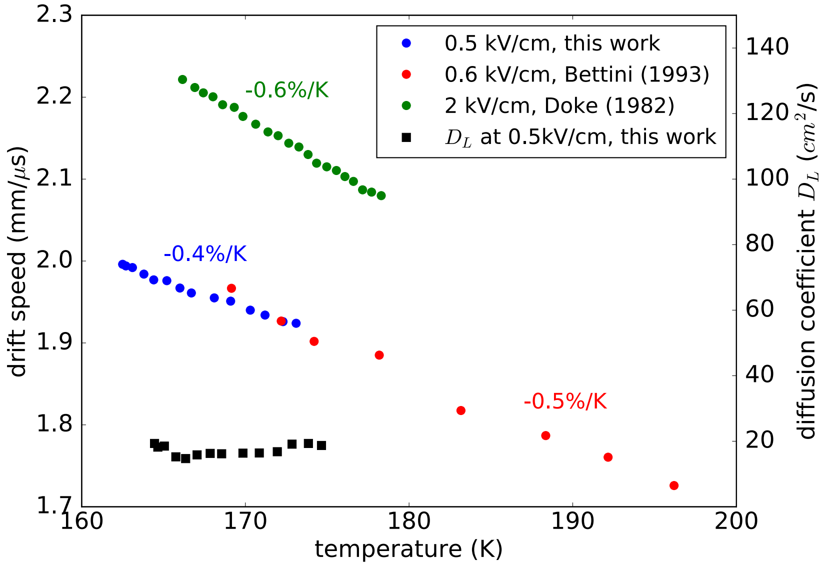

Figure 6.38: Temperature dependence of the electron drift velocity in LXe (solid blue circle). Also included are measurements from others: Doke (green) [88] and Benetti (red) [101]. No temperature dependence was observed for the longitudinal diffusion coefficient D_L (black squares), which corresponds to the right-hand y-axis.

However, in GXe both D_L and the drift velocity increase linearly with temperature; this is shown on figure 6.39. We note that the drift velocity in LXe decreases with temperature while in GXe it increases with temperature. The opposite behavior was reported in LAr and GAr [86]. For our experiment the accuracy on the temperature measurement is better than 0.2 K. The temperature gradient between anode and photocathode is finite and maintained to be $\leq$ 0.3 K.

6.5.4 Electron lifetime

It is well known that doping Ar or Xe with impurities (>1 ppb) increases the drift speed and reduces the electron lifetime [97, 88]. In the case of the electron lifetime this is because the electronegative impurities readily capture the drifting electrons. A common argument to explain the observation that purification techniques that are used to remove such impurities in Ar seem ineffective when applied to Xe is that in LXe (162 K) those impurities remain in solution [102] while they freeze out in LAr (87 K). This argument suggests that as the temperature increases the lifetime should

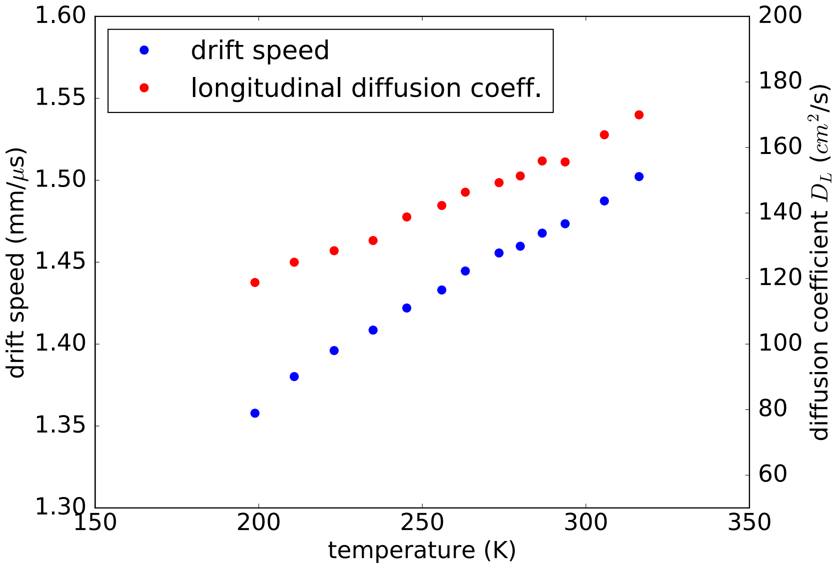

Figure 6.39: Temperature dependence of electron drift velocity and diffusion coefficient D$_L$ in GXe. The drift velocity (blue) corresponds to the left-hand y-axis, while D$_L$ (red) corresponds to the right-hand y-axis.

get worse, although it is not clear what temperature change will produce a measurable effect. This brings us back to the question of how exactly does drift speed correlate to purity. Does higher purity necessarily mean lower drift speed? If so, the speed should increase with higher temperature.

An intuitive way to think about the electron lifetime is as a ratio Q_c/Q_a. Q_c is the amount of charges leaving the cathode and Q_a that arriving at the anode. The electron lifetime is infinite if this ratio is 1, i.e. no charge is lost. Thus, the lifetime is

$$\tau = t_d/\ln(Q_c/Q_a), \tag{6.9}$$

where t_d is the drift time. To measure Q_c, we added in front of the cathode a wire grid identical to the one already in use at the anode (see figure 6.6). We also purchased two identical preamps (cremat cr-110) to record Q_c and Q_a. The modified electrode structure is shown in figure 6.6. First we optimized the electric fields arrangement to guarantee 100% transmission of electrons through the wire grids.

Our grids are identical x-y grids with pitch d = 350 μm and wire diameter 2r = 35 μm. Since the wire diameter is 10% of the pitch, the open space is 0.9 times the pitch and the unblocked area is $0.9^2 = 0.81$ of the area leading to the field ratio of 1/0.81 = 1.23. However it is more accurate to do the following: if one unrolls the wire circumference, the wire blocks π times the diameter or 0.314 of the pitch. This leaves 0.686 of the pitch open in each direction, so the area open is $0.686^2 = 0.472$ of the mesh's area. The requirement for good transparency [69] is

$$\frac{E_{i+1}}{E_i} > \frac{1+\rho}{1-\rho} \tag{6.10}$$

where ρ is the ratio $\frac{2\pi r}{d}$, and E_i and E_{i+1} are the fields on either side of the grid. So, for our grids a field ratio of 1.92 should be sufficient. This was verified empirically and is shown on figure-6.7. We decided to run with a field ratio of 2. In the case of the anode this ratio does not give the optimal transmission. As figure 6.40 showed we do not start to see saturation until about a ratio of 5. We suspect this was because the wire pitch d = 350 μm is comparable to the spacing between the grid and the anode (290 μm).

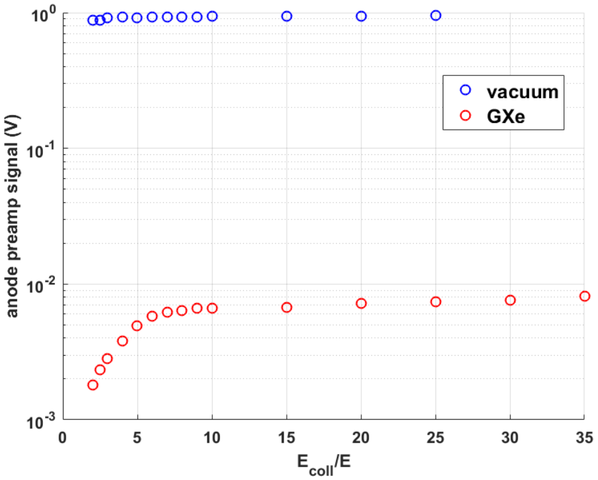

Figure 6.40: Anode signal vs collection field in a semilog plot. The transmission saturates once the collection field is >5 times the drift field.

Figure 6.42 shows our best measurement of Q_c/Q_a.

We ran a series of test to understand the source of our poor lifetimes but could not resolve this issue.

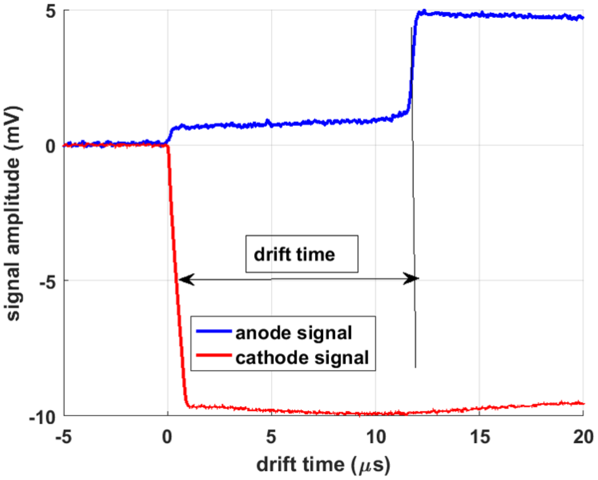

Figure 6.41: Typical anode (blue) and cathode (red) traces. The ratio of amplitudes is a measure of electron lifetime

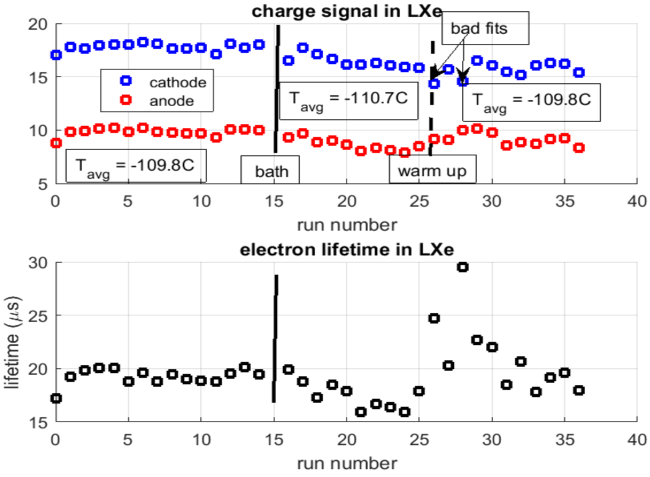

Figure 6.42: Data from a typical electron lifetime measurement. The top panel shows the raw amplitudes measured at the cathode (blue) and at the anode (red). The bottom panel is the calculated lifetime. Data points/run numbers are 5 minutes apart. After an hour of data taking the ethanol bath was changed, causing some temporary instability.

1. All plastics and other materials prone to out-gassing were removed in the 2nd/current iteration of the cell.

2. Longer bake out and pumping periods prior to data taking runs were implemented.

3. A series of extended (4-5 hours of data taking as opposed to the usual 2) runs were performed. We saw no significant improvements from these. Longer runs were not possible because of

our liquefaction mechanism, i.e. maintaining a cold ethanol bath for more than 5 hours was very resource-intensive and rather inefficient.

4. We purchased a new purifier when we started suspecting our purifier may be defective. After installation and careful leak checking a series of runs was performed and no improvement to the lifetime was observed.

5. We acquired ”pure” Xenon from the group of Aleksey Bolotnikov at BNL. This Xenon had been used 15-20 years earlier for detection of cosmic rays and lifetimes of 500 μs in the gas phase were reported with it [103]. Our own lifetime measurements with this xenon in both gas and liquid phases were not better than what we measured and are reporting in this thesis.

All these point to either a fundamental defect (materials used, welds, slow virtual leaks) in the construction of the cell which prevented us to ever reach desired purity levels or the crucial importance of having a recirculation loop so that the xenon can be continually purified even as it is being used for measurements. Table 6.4 summarizes electron lifetime measurements found in the literature.

Author	Drift length (mm)	Drift speed (mm/μs)	Electron lifetime (ms)	Recirculation
Aprile (1990) [102]	59 K	2.0, 500 V/cm	>0.220	no
Benetti (1993) [101]	50	1.97, 600 V/cm	> 1	no
Yoo (2015) [90]	80	1.77, 500 V/cm	0.039	no
Albert (2017) [71]	182.	1.71, 380 V/cm	>2	yes
This work (2018)	20.	1.96, 500 V/m	> 0.02	no

Table 6.4: Literature values for electron lifetimes in LXe.

6.6 Multi photon ionization of liquid xenon

Our first measurements (performed with the YAG laser) upon commissioning of the LXe cell exposed two issues: first the electron drift speed was much higher than those found in the literature (see section **??**). Second the photoelectron signal sat on a large background which we soon understood to be laser-induced LXe multiphoton ionization (MPI). The first problem could be resolved by improving the purity of the liquid as already addressed and the second could be mitigated by turning off the MPI process.

MPI occurs when, in response to exposure to radiation, two or more photons are simultaneously absorbed via virtual states in a medium. This process requires instantaneous high photon flux only achievable in pulsed laser. Hence MPI can be turned on and off by controlling the laser peak intensity, which is inversely proportional to the pulse duration. A nice introduction to this topic can be found in [104]. Before we could make any meaningful physics conclusions about our measurements we needed to decouple the MPI signal from the photoelectron signal. We relied on three lasers to simultaneously do this: Nd:YAG (4.66 eV, 60 ps), Excimer (5 eV, 7 ns), and Nd:YLF (4.73 eV, 71 ns).

The ionization potential for atomic xenon is $\sim$ 9 eV [105]. Two UV photons can thus be simultaneously absorbed to produce 2-photon ionization. Figure-6.43 shows sample preamp traces for each type of laser. The photoelectron signal from the photocoathade is proportional to the step near 10 μs, the electron's drift time from cathode to anode At 500 V/cm drift field. Any other electrons detected before that is due to laser-induced ionization of LXe. This effect is most significant with the 60-ps YAG, moderate with the 7-ns Excimer, and nearly zero when the 71-ns YLF laser is used. As the laser beam propagates and expands, the peak intensity diminishes. Therefore, MPI is larger near the photocathode (10 μs) than it is at the anode (0-0.5 μs).

To further understand this, we studied the beam propagation for each laser. Using a UV CCD camera, we measured each laser's spot size as a function of propagation distance in air, with a later correction to account for the difference in indexes of refraction between air and LXe. We also need to apply a small correction (1 mm to z position) due to the fact that z = 0 in our measurements is about 1 mm away from the fiber output. We found that the YLF diverges much faster than the Excimer and the YAG. The YAG diverged least, which meant the peak intensity remains high over a longer distance, causing more MPI. This agreed well with our LXe measurements.

If we crudely compare the amplitude of the MPI signal to that of the photoelectron signal as a function of laser energy, we can confirm that the latter is indeed a 1-photon process (photoelectric

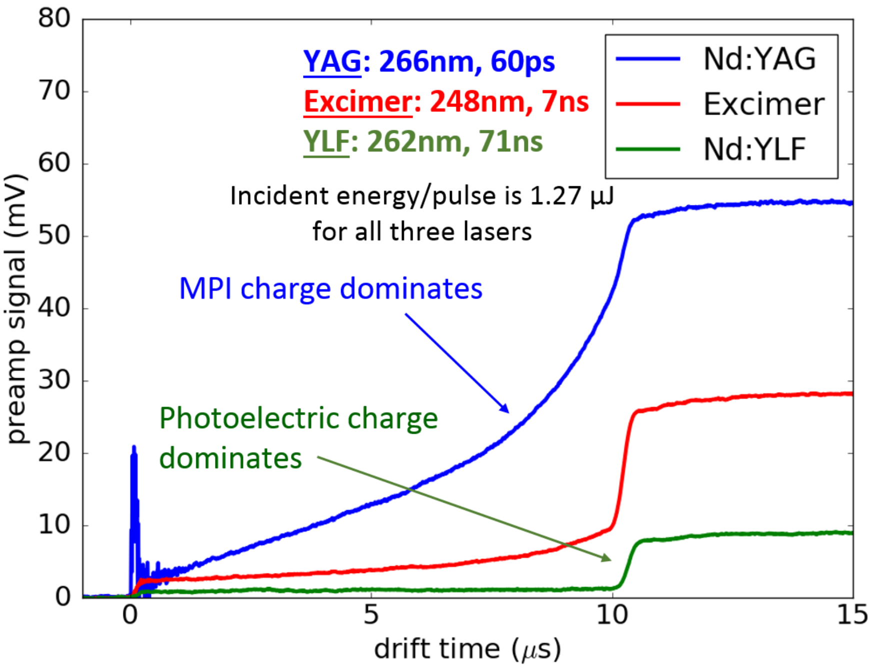

Figure 6.43: Electron charge signal pulse shapes when lasers of different peak powers (but same energy densities) are employed. Nd:YLF (green): 4.73 eV, 71 ns, kW/cm^2, (green). Excimer (red): 4.99 eV, 7 ns, 10 kW/cm^2. Nd:YAG (blue): 4.66 eV, 60 ps, MW/cm^2.

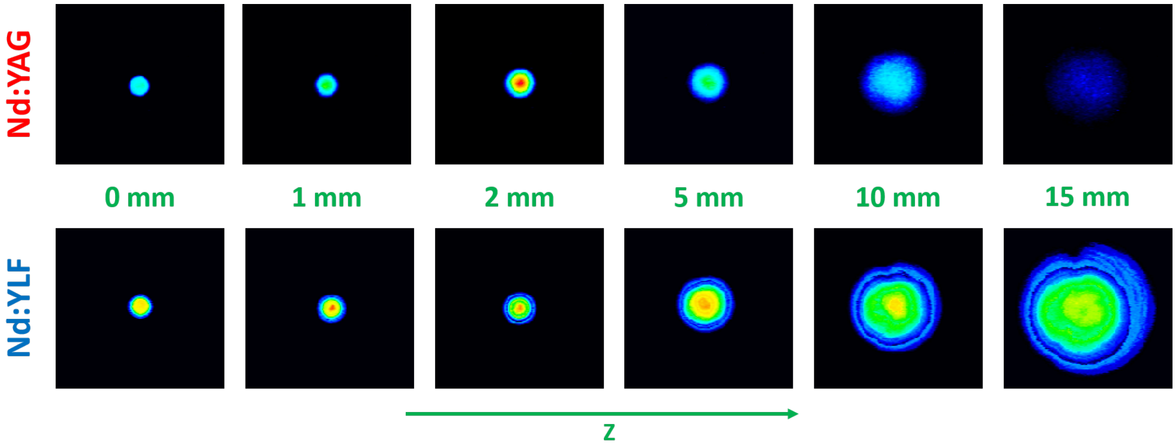

Figure 6.44: A comparison of the laser spot size for the YAG and YLF as a function of propagated distance. The YLF diffracts faster than the YAG. This means the intensity is lower and this translates in reduced ionization. Measurements were made in air. For extrapolation to LXe the index of reraction of LXe was used.

effect) while the former is a 2-photon process. This is shown in figure 6.43.

Using these MPI measurements it is possible to extract the 2-photon absorption cross-section of LXe. In fact this cross-section was already measured ($\sigma^2 = 1.26 \times 10^{-52}$ cm^2 at 266 nm) and

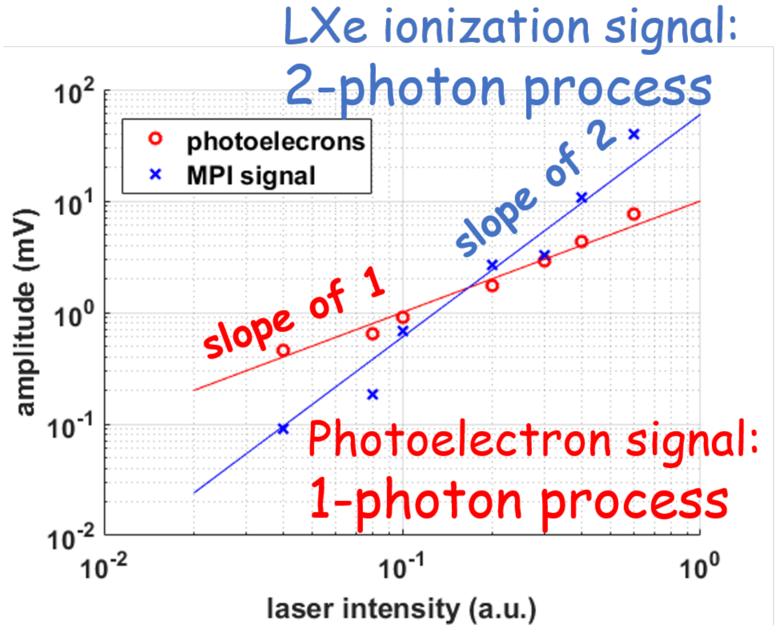

Figure 6.45: A log-log plot of ionization charge signal (blue) and photoelectron signal from the photocathode (green) against normalized laser energy density. Their slopes reveal the orders of the linear photoemission and the nonlinear multiphoton ionization process.

reported in Kendi Hall's thesis [106]. Using Hall's measurement we calculated the expected MPI shape for the YAG and found the two agree within a factor of 1.7. This is shown in figure 6.46.

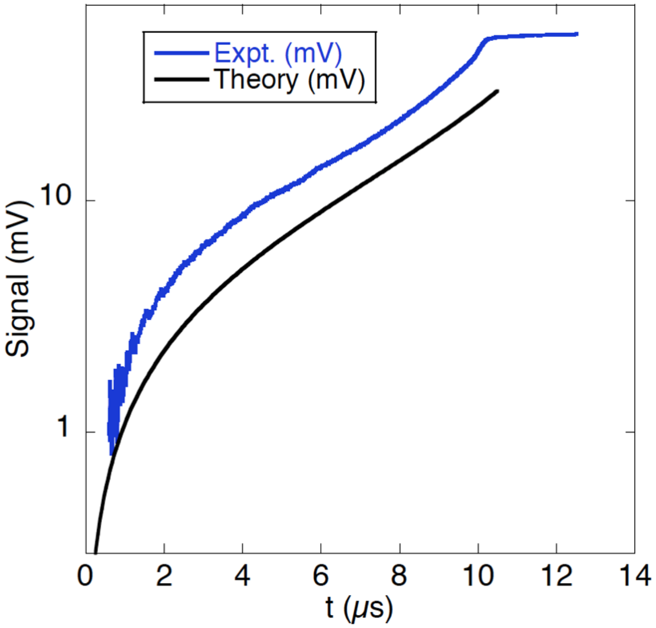

Figure 6.46: Agreement with laser pulse widths differing by two orders of magnitude.

6.7 Properties of the gold photocathode

6.7.1 Quantum efficiency

The quantum efficiency (QE) is defined as the number of electrons leaving the photocathode per number of UV photons incident on its surface. This is an important parameter if photocathodes are to be used for calibration. Our measurement of the charges leaving the photocathode is done using the double grid configuration and measuring Q_c. Since the mesh is 1.28 mm away from the photocathode, any electron loss in that volume is not reflected in the measurement and should be included as an error. To estimate this, we remember that the number of charge carriers that survive is given by:

$$N(t) = N_0 e^{-t/\tau} \tag{6.11}$$

where τ is the electron lifetime and N_0 is the true number of electrons generated at the photocathode. The drift time t is dependent on the applied field, as is τ. We can thus calculate the ratio $(N_0 - N(t))/N_0$ and include this as an error for our measurement. Note that in vacuum the lifetime is infinite so this effect is not relevant.

Another source of error for this measurement is the photoemission process itself: If too large/dense a charge leaves the cathode, it changes the electric field in the gap and some of the electrons go back to the cathode. This is known as the space charge effect. Consider the charge q concentrated in a sphere of radius r. The electric field at the surface of this sphere is: $E = \frac{q}{4\pi\epsilon r^2}$. When this field gets of the order of magnitude of the external field E$_{extract}$, it means that space charge limit is near.

Figure 6.47 shows our measurements of QE performed in vacuum, gaseous xenon, and liquid xenon. The laser energy per pulse is measured using a J3-02 Molectron pyroelectric energy detector fitted with a fiber-coupled adapter. At the extraction field of 0.5 kV/cm (applied field between the photocathode and the upper mesh) QEs of $\sim 5.21 \times 10^{-6}$, $\sim 5.0 \times 10^{-7}$, $\sim 5.1 \times 10^{-7}$ are obtained when the photocathode is operated in vacuum, 1.5 bar of GXe at room temperature, and in LXe, respectively. The decrease in GXe is likely due to Xe atoms attaching to the gold

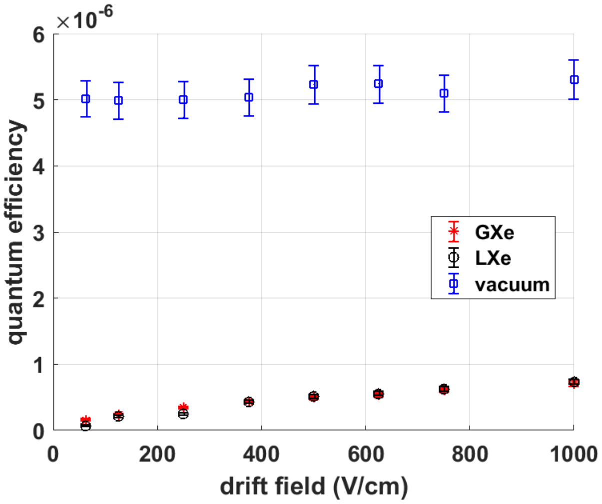

Figure 6.47: plot of the quantum efficiency as a function of extraction field in vacuum (blue), GXe (red), and LXe (black).

surface and changing the potential barrier to electron escape; the vacuum QE can be reliably recovered by pumping out the GXe. A similar effect may be responsible for the reduced QE in LXe but a careful investigation of this was not conducted.

To first order approximation the QE can be expressed as:

$$QE = A(h\nu - \phi)^2 \tag{6.12}$$

where A is a constant that depends on the photocathode material properties such as absorption coefficient, density of states, and the surrounding environment, ϕ is the work function of the material [107, 108]. The QE is known to increase slightly with the decrease of the work function but this effect tend to be limited by the presence of surface contaminants and the character of the density of states on the material surface [107, 108]. This work function can be lowered by increasing the energy of the electrons either thermally, electrically, or both. In the presence of an external field, the work function can be lowered [107]. A high external field will also narrow the potential barrier, so that the excited electron could tunnel through the barrier and into the continuum [109, 107]. In practice, these processes overlap because of the smearing of the electron energy distribution, and local enhancement of the applied field that results from non uniformities on the surface of the material. Based on the Schottky effect, the lowering of the work function and the quantum efficiency can be expressed as

$$\phi_0 - \phi = (\frac{eE}{4\pi\epsilon_0})^{1/2} \tag{6.13}$$

from which it follows

$$QE^{\frac{1}{2}} = A^{1/2}[h\nu - \phi_0 + (\frac{eE}{4\pi\epsilon})^{1/2}]. \tag{6.14}$$

ϕ_0 is the unchanged zero-field work function, e is the electron charge, $\epsilon = \kappa\epsilon_0$ is the G/LXe dielectric constant, E is the extraction field, and $h\nu$ is the photon energy. As shown in figure 6.47, the QE in vacuum is independent of extraction field. This is because electrons released from the surface instantaneously accelerate away from the cathode, as is reflected by the near zero drift times in vacuum. Space charge cannot build up under these conditions.

In GXe and LXe there is a slight deviation from the expected linear dependence. This is more visible in figure 6.48 where we have plotted $\sqrt{QE}$ vs $\sqrt{E}$. This behavior is not understood. In addition, two distinguishable regimes with two different slopes are noticeable when extraction fields are less than or greater than 150V/cm; this distinction is particularly discernible in the case of LXe.

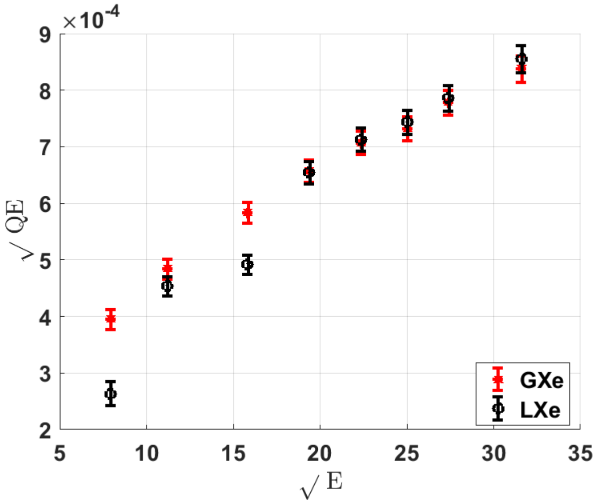

Figure 6.48: $\sqrt{QE}$ vs $\sqrt{E}$

We calculated the maximum static Coulomb field of the lingering electron cloud right after being photo-emitted from the surface of the photocathode to be 50 V/cm. Therefore, when extraction field is 50 V/cm or less, effects resulting from space charge limit may be significant. To examine this, we increase the Coulomb field by using an equal energy but much shorter Nd:YAG laser. Although the absolute QE was slightly different because of the difference in photon wavelengths (266 nm vs 262 nm), the magnitude of the slope at low fields remained similar ruling out space charge effect. We thus speculate that at low fields back diffusion of charge is the dominant mechanism limiting the number of electrons escaping the metal surface. Hence the collisional diffusion of photoelectrons off the densely packed atoms in LXe would yield less electrons ejected from the photocathode than in GXe. This qualitative argument is supported by the experimental observation shown at the low field in figure 6.48.

6.7.2 Work function measurement

We made a preliminary measurement of the work function of the gold. This measurement is relevant because our photocathode is a 22 nm gold layer and the work function for the bulk is known to differ slightly from that for thin films. Values in the literature vary from 3.89 eV [107] to 5.30 eV [110] depending on the measurement conditions.

To perform this measurement we utilized a picoammeter directly connected to the cathode. The picoammeter measures the current leaving the cathode. The light source was a xenon flash lamp generating white light source which was then fed through a grating so that different wavelength could be selected. We scanned the wavelength from 200 nm to 500 nm. Figure 6.49 shows a schematic diagram of the experimental setup.

Our results are shown on figure 6.50. We report a value of 4.1 eV for the work function in vacuum. This is in good agreement with measurements by Li [86] on similar photocathodes. We were not able to make measurements in GXe and LXe because the factor of 10 or greater drop in signal (see QE figure 6.47) meant that the gas and liquid signals fell below the sensitivity of our picoammeter.

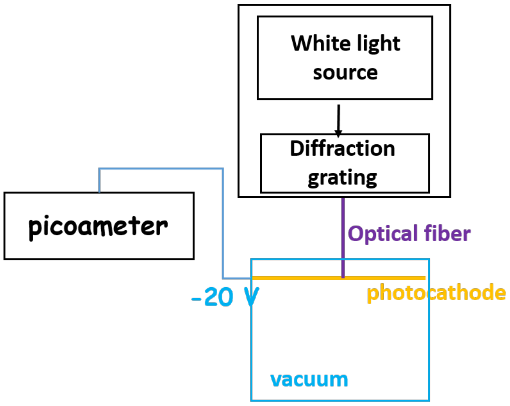

Figure 6.49: Schematic of workfunction measurement

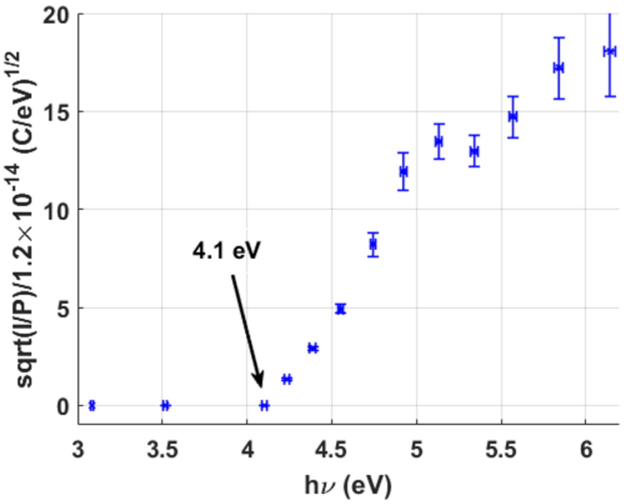

Figure 6.50: work function

6.8 Discussion

Our target electron lifetime for this cell was 100 μs. We were not able achieve this but nonetheless we made significant progress in demonstrating the feasibility of using laser-driven photocathodes for calibration purposes.

First our measurement of the longitudinal diffusion is significant. D_L is an important parameter in the design of a large detector such as nEXO. And to the best of our knowledge only one other measurement has been reported in LXe at a single field [98]. The fact that our measured D_L values also seem to approach D_T (the transverse diffusion coefficient) at low field, as theoretical models have suggested it should, is yet another validation that this very difficult measurement we performed is on solid ground and will benefit the LXe community.

The measurements of quantum efficiency and work function in vacuum are consistent with literature values. The measurements in gas and liquid xenon need to be independently validated. It should be stated that we observed rather significant drops (>25%) in vacuum signal over repeated use of the photocathode. However these were not systematically logged and numerous factors could have been at play. A careful study of the photocathode's stability should really be done. Based on our studies here we now have detailed laser specifications that would be appropriate for the photocathode while minimizing the LXe MPI.

With regard to the electron lifetime it is unclear what the weak link in our setup was. We suspect the out-gassing rate must be larger than what we estimated. Perhaps the fact that half of the inner wall surface is never covered in xenon played a role, i.e. out-gassing caused the LXe to become less pure as the run went on. Another issue is the window: it failed one time (i.e leaked) and we needed to replace it. The leak was small (but detectable) and it is unclear when or over what period of time it developed. A second iteration of the cell should not have a window; this would reduce the possibility of a leak and would allow operation at higher pressure and over a wider region of the phase transition space. We have already started designing a new cell for the lab at Stony Brook with the goal of having a future student study the stability of the gold photocathode. The cell will be large enough to hold 4 photocathodes which can be illuminated simultaneously. While the electron lifetime won't be a critical parameter it will still be desirable and so we've explored the possibility of purchasing a recirculation pump. Lastly the cooling will be more modern and reliable, with a cold finger assembly and automated control.

Chapter 7

Conclusions

Neutrinoless double beta decay is the most promising avenue for searching for Lepton Number Violation. The planned tonne scale experiments currently being considered are in many ways entering the golden age for the field. This is because they will be able to achieve incredible background rejections thereby evr approaching half-life sensitivities of 10^{28} years. nEXO will lead the way by building on the success of EXO-200 and taking advantage of other existing technologies as well as some still being developed such as Barium tagging [14], or laser-driven cathodes for in-situ lifetime monitoring.

In this thesis we built and operated a LXe TPC instrumented with a photocathode to demonstrate the feasibility of the method. While there is still a long way to go we made some significant measurements that demonstrate the far-reaching power and versatility of such a system. For example we placed an upper bound on the longitudinal growth of charge clusters in the LXe at a wide range of fields. We measured the temperature coefficient confirming the already known fact that a good handle on temperature is important for stable operation. Our measurement of the quantum efficiency over numerous months showed that the photocathodes can be operated reliably, although a more systematic study is required. Finally by being able to disentangle gold photoelectricity from xenon multiphoton ionization we demonstrated the discriminating power of the method. Since we can turn MPI on and off by careful choice of laser light it is not inconceivable to imagine a scenario where nEXO might want to create known ionization on purpose for calibration purposes.

Future work with this system will involve a systematic study of the gold photocathode stability. This might involve measurements of QE and workfunction at different temperatures. Another important aspect will be the study of induction signals. Unlike our cell nEXO will not employ a Frisch grid. Work with this cell could also be made more efficient by implementing a more modern cooling mechanism. While te ethanol bath worked, too often instabilities in the signal would appera during chang-over. Furthermore operation of the cell as currently designed always required two people for operation.

Regarding the ^{134}Xe, we showed that with just one year of phase 2 (and half the exposure reported in the Phase 1 result) we can already make improvements on the half-life limit. This is due to the combined effects of improved MC, somewhat lower ^{85}Kr content, and overall improved detector efficiency. A more complete analysis would

1. take a closer look at ^{85}Kr,
2. combine the the years of phase 1 with the 3 years of phase 2 once the data becomes available,
3. take advantage of the continually improving analysis tools and methods.

Appendix A

Longitudinal Diffusion

To adequately describe the time evolution of an electron bunch moving through a material under the influence of an electric field, three processes must be considered:

1. the drift speed of the center of mass;
2. the diffusional growth of the bunch;
3. electron losses through attachment to impurities or gins from ionization of the medium.

Let $n \equiv n(x, yx, z)$ be the electron charge density distribution at position (x,y,z) and time t. The electrons move in the z-direction with average velocity v. The time evolution of the bunch is described by Fick's equation:

$$\frac{\partial n}{\partial t} = D_L \frac{\partial^2 n}{\partial^2 z} + D_T(\frac{\partial^2 n}{\partial^2 x} + \frac{\partial^2 n}{\partial^2 y}) - v\frac{\partial n}{\partial z} - \lambda v n \tag{A.1}$$

where λ is a coefficient parameterizing the difference between attachment and ionization. If there is no ionization (YLF laser in our case) then $1/\lambda$ is just the mean free path.The solution to equation A.1 is:

$$n(\rho, z, t) = \frac{n_0}{4\pi D_T t\sqrt{4\pi D_L t}} \exp(-\frac{(z - vt)^2}{4D_L t} - \lambda v t) exp(-\frac{\rho^2}{4D_T t}) \tag{A.2}$$

where we've switched to cylindrical coordinate $\rho^2 = x^2 + y^2$. n is Gaussian in z and ρ at any time t but is not Gaussian in time t at any all fixed point in space. n will induce a current $j(t)$ on a perpendicular x-y plane a distance d. We can take this plane to be the anode and $j(t)$ is given by:

$$j(t) = 2\pi \int \rho \cdot n(\rho, d, t) \cdot d\rho = \frac{n_0}{\sqrt{4\pi D_L t}} exp(-\frac{(d-vt)^2}{4D_L t} - \lambda vt) \tag{A.3}$$

When dealing with electron diffusion it is more natural to discuss $\sigma_t = \sigma_z / v_d$ since we measure time signals. The ttotal electron width σ_e is actually a combination of σ_t and σ_0 where σ_0 is a free parameter encompassing other effects such as the electronics response and in our case the laser width. This is what we called σ_{vac} in chapter 6. We can thus write:

$$\sigma_e^2 = \sigma_t^2 + \sigma_0^2. \tag{A.4}$$

There is an underlying assumption that the function f_0 which describe the other phenomena not included in σ_t is Gaussian with standard deviation σ_0. The diffusion coefficient is then given by:

$$D_L = \frac{v_d^2(\sigma_e^2 - \sigma_0^2)}{2t}, \tag{A.5}$$

which is just equation 6.3.

Equation A.3 states that the longitudinal temporal growth of the electron bunch is proportional to the square root of the drift distance at a fixed electric field. As the applied electric field approaches zero, the electrons gain very little energy from the field. The elastic atomic collisions then cause them to come in thermal equilibrium with the material (Xenon). In this case the diffusion coefficients are given by the Einstein-Smoluchowski relation D = $\frac{kT}{e}\mu$ where μ is the electron mobility. As the field increases the electrons gain more energy from the field and their temperature exceeds the thermal limit so that the mobility decreases and the diffusion coefficient increases. The Einstein-Smoluchowski relation generalizes to:

$$D_T = \frac{kT}{e}\mu \tag{A.6}$$

$$D_L = \frac{kT}{e}(\mu + E\frac{\partial\mu}{\partial E}) \tag{A.7}$$

The ratio of D_L to D_T is an interesting parameter:

$$\frac{D_L}{D_T} = 1 + \frac{E}{\mu}\frac{\partial\mu}{\partial E}. \tag{A.8}$$

At low fields the mobility approaches a constant and we have $D_L/D_T \approx 1$.

Appendix B

Multiphoton ionization theory

The ionization rate per volume per atom W$_{ij}$ is:

$$W_{ij}(\vec{r},t) = \sigma_{ij}^{(n)}(\frac{I(\vec{r},t)}{h\nu})^n \tag{B.1}$$

where thw intensity I is given by:

$$I(\vec{r},t) = I_0 F(\vec{r}) T(t) \tag{B.2}$$

The number of electrons is

$$\frac{dN_e}{dz} = n_0 \int W_{ij}(\vec{r},t) dA dt, \tag{B.3}$$

here n$_0$ = Xe atom density. We can rewrite:

$$\begin{aligned} \frac{dN_e}{dz} &= \sigma_{ij}^{(n)} n_0 \Big(\frac{I_0}{h\nu}\Big)^n \int [T(t)]^n dt \int [F(\vec{r})]^n dA_0 \\ &= \sigma_{ij}^{(n)} n_0 \Big(\frac{I_o}{h\nu}\Big)^n \tau_n A_n. \end{aligned} \tag{B.4}$$

For a Gaussian time profile,

$$\tau_n = \int_{-\infty}^{\infty} [e^{-(t/\tau)}]^n dt = \sqrt{\frac{\pi}{n}}\tau = \frac{\tau_1}{\sqrt{n}} \tag{B.5}$$

and for the Gaussian spatial profile we have

$$A_n = \int_{-\infty}^{\infty} [e^{-(2r^2/w^2)}]^n 2\pi r dr = \frac{\pi w^2}{2n}. \tag{B.6}$$

The laser pulse energy is $E = i_)\tau_1 A_1$. thus:

$$\frac{dN_e}{d_z} = \sigma_{ij}^{(n)} n_0 \tau_n A_n \Big(\frac{E}{h\nu\tau_1 A_1}\Big)^n. \tag{B.7}$$

For n = 2,

$$\frac{dN_e}{dz} = \sigma_{ij}^{(2)} \frac{n_0}{2\sqrt{2}\tau_1 A_1}\Big(\frac{E}{h\nu}\Big)^2 \tag{B.8}$$

which in terms of the laser FWHM Δt, $\tau_1 = \sqrt{\frac{\pi}{4\ln 2}}\Delta t = 1.06\Delta t$.

For our expanding laser beam from multimode fiber:

$$w = w_0 + z\tan\theta \tag{B.9}$$

w_0 is the initial beam radius which we can take to be 420 μm for our 600 μm core diameter fiber. θ is the fiber acceptance angle: $\sin\theta = \frac{NA}{n} = \frac{numerical\ aperture\ of\ fiber}{index\ of\ refraction\ of\ LXe}$; we have tan$\theta$ = 0.154, so w(z = 2 cm) = 3500 μm. The expansion effect i significant and can't be ignored in the fit. So:

$$\frac{dN_e}{dz} = \sigma_{ij}^{(2)} \frac{n_0}{\pi\sqrt{2}\tau_1(w_0 + z\tan\theta)^2}\Big(\frac{E}{h\nu}\Big)^2. \tag{B.10}$$

With z = d-vt and electron loss factor e$^{-\mu t}$ (1/μ = electron lifetime).

Bibliography

[1] Laurie M Brown. The idea of the neutrino. *Physics Today*, 31(9):23, 1978.

[2] Nathalie Palanque-Delabrouille, Christophe Yèche, Julien Lesgourgues, Graziano Rossi, Arnaud Borde, Matteo Viel, Eric Aubourg, David Kirkby, Jean-Marc Legoff, James Rich, et al. Constraint on neutrino masses from sdss-iii/boss lyα forest and other cosmological probes. *Journal of Cosmology and Astroparticle Physics*, 2015(02):045, 2015.

[3] Stephane Plaszczynski. Neutrino matter with planck. *arXiv preprint arXiv:1012.2215*, 2010.

[4] Laurence F Abbott, Alvaro De Rújula, and TP Walker. Constraints on the electron-neutrino mass from the supernova data a systematic analysis. *Nuclear Physics B*, 299(4):734–756, 1988.

[5] G Drexlin, V Hannen, S Mertens, and C Weinheimer. Current direct neutrino mass experiments. *Advances in High Energy Physics*, 2013, 2013.

[6] André De Gouvêa. Neutrino physics. In *Physics In D 4 Tasi 2004: TASI 2004*, pages 197–258. World Scientific, 2006.

[7] JD Vergados. The neutrinoless double beta decay from a modern perspective. *Physics reports*, 361(1):1–56, 2002.

[8] Werner Rodejohann. Neutrinoless double-beta decay and neutrino physics. *Journal of Physics G: Nuclear and Particle Physics*, 39(12):124008, 2012.

[9] N Barros, J Thurn, and K Zuber. Double beta decay searches of 134xe, 126xe and 124xe with large scale xe detectors. *Journal of Physics G: Nuclear and Particle Physics*, 41(11):115105, 2014.

[10] SR Elliott, AA Hahn, and MK Moe. Direct evidence for two-neutrino double-beta decay in se 82. *Physical Review Letters*, 59(18):2020, 1987.

[11] JB Albert, M Auger, DJ Auty, PS Barbeau, E Beauchamp, D Beck, V Belov, C Benitez-Medina, J Bonatt, M Breidenbach, et al. Improved measurement of the 2 ν β β half-life of 136 xe with the exo-200 detector. *Physical Review C*, 89(1):015502, 2014.

[12] JB Albert, DJ Auty, PS Barbeau, E Beauchamp, D Beck, V Belov, C Benitez-Medina, J Bonatt, M Breidenbach, T Brunner, et al. Search for majorana neutrinos with the first two years of exo-200 data. *Nature*, 510(7504):229, 2014.

[13] JB Albert, G Anton, I Badhrees, PS Barbeau, R Bayerlein, D Beck, V Belov, M Breidenbach, T Brunner, GF Cao, et al. Searches for double beta decay of xe 134 with exo-200. *Physical Review D*, 96(9):092001, 2017.

[14] S Al Kharusi, JB Albert, M Alfaris, G Anton, IJ Arnquist, I Badhrees, PS Barbeau, D Beck, V Belov, T Bhatta, et al. nexo pre-conceptual design report. *arXiv preprint arXiv:1805.11142*, 2018.

[15] JB Albert, G Anton, IJ Arnquist, I Badhrees, P Barbeau, D Beck, V Belov, F Bourque, JP Brodsky, E Brown, et al. Sensitivity and discovery potential of nexo to neutrinoless double beta decay. *arXiv preprint arXiv:1710.05075*, 2017.

[16] E Aprile and T Doke. Liquid xenon detectors for particle physics and astrophysics. *Reviews of Modern Physics*, 82(3):2053, 2010.

[17] Fred L Wilson. Fermi's theory of beta decay. *American Journal of Physics*, 36(12):1150–1160, 1968.

[18] Frederick Reines, CL Cowan Jr, FB Harrison, AD McGuire, and HW Kruse. Detection of the free antineutrino. *Physical Review*, 117(1):159, 1960.

[19] Maurice Goldhaber, L Grodzins, and AW Sunyar. Helicity of neutrinos. *Physical Review*, 109(3):1015, 1958.

[20] Gaillard Danby, JM Gaillard, Konstantin Goulianos, LM Lederman, N Mistry, M Schwartz, and J Steinberger. Observation of high-energy neutrino reactions and the existence of two kinds of neutrinos. *Physical Review Letters*, 9(1):36, 1962.

[21] Martin L Perl, GS Abrams, AM Boyarski, Martin Breidenbach, DD Briggs, F Bulos, William Chinowsky, JT Dakin, GJ Feldman, CE Friedberg, et al. Evidence for anomalous lepton production in e+- e- annihilation. *Physical Review Letters*, 35(22):1489, 1975.

[22] L MARTIN. The discovery of the tau lepton. 1992.

[23] K Kodama, N Ushida, C Andreopoulos, N Saoulidou, G Tzanakos, P Yager, B Baller, D Boehnlein, W Freeman, B Lundberg, et al. Observation of tau neutrino interactions. *Physics Letters B*, 504(3):218–224, 2001.

[24] A de Gouvea, K Pitts, K Scholberg, GP Zeller, J Alonso, A Bernstein, M Bishai, S Elliott, K Heeger, K Hoffman, et al. Neutrinos. *arXiv preprint arXiv:1310.4340*, 2013.

[25] Rabindra N Mohapatra, Stefan Antusch, KS Babu, Gabriela Barenboim, Mu-Chun Chen, A De Gouvêa, P De Holanda, B Dutta, Y Grossman, A Joshipura, et al. Theory of neutrinos: a white paper. *Reports on Progress in Physics*, 70(11):1757, 2007.

[26] SNO collaboration et al. Measurement of the rate of nu_e+ d–¿ p+ p+ e^-interactions produced by 8b solar neutrinos at the sudbury neutrino observatory. *arXiv preprint nucl-ex/0106015*, 2001.

[27] Y Fukuda, T Hayakawa, E Ichihara, K Inoue, K Ishihara, H Ishino, Y Itow, T Kajita, J Kameda, S Kasuga, et al. Evidence for oscillation of atmospheric neutrinos. *Physical Review Letters*, 81(8):1562, 1998.

[28] Jose Bernabeu. On the history of the pmns matrix... with today's perspective. *arXiv preprint arXiv:1312.7451*, 2013.

[29] André De Gouvêa. Neutrino mass models. *Annual Review of Nuclear and Particle Science*, 66:197–217, 2016.

[30] Maria Concepción Gonzalez-Garcia and Michele Maltoni. Phenomenology with massive neutrinos. *Physics Reports*, 460(1-3):1–129, 2008.

[31] Heinrich Päs and Werner Rodejohann. Neutrinoless double beta decay. *New Journal of Physics*, 17(11):115010, 2015.

[32] Erasmo Recami. Ettore majorana: his work and his life. *arXiv preprint arXiv:1412.7485*, 2014.

[33] Maria Goeppert-Mayer. Double beta-disintegration. *Physical Review*, 48(6):512, 1935.

[34] C Patrignani, Particle Data Group, et al. Review of particle physics. *Chinese physics C*, 40(10):100001, 2016.

[35] SM Bilenky and Carlo Giunti. Neutrinoless double-beta decay: A brief review. *Modern Physics Letters A*, 27(13):1230015, 2012.

[36] E Kh Akhmedov. Neutrino physics. *arXiv preprint hep-ph/0001264*, 2000.

[37] Steven R Elliott and Jonathan Engel. Double-beta decay. *Journal of Physics G: Nuclear and Particle Physics*, 30(9):R183, 2004.

[38] Neutrino mass and direct measurements.

[39] Steven R Elliott, Craig E Aalseth, M Akashi-Ronquest, M Amman, John F Amsbaugh, FT Avignone Iii, Henning O Back, Cryus Baktash, Alexander S Barabash, P Barbeau, et al. The majorana project. In *Journal of Physics: Conference Series*, volume 173, page 012007. IOP Publishing, 2009.

[40] J Janicsko-Csathy, Gerda Collaboration, et al. Status of the gerda experiment. *Nuclear Physics B-Proceedings Supplements*, 188:68–70, 2009.

[41] M Agostini, M Allardt, E Andreotti, AM Bakalyarov, M Balata, I Barabanov, M Barnabé Heider, N Barros, L Baudis, C Bauer, et al. Results on neutrinoless double-β decay of ge 76 from phase i of the gerda experiment. *Physical Review Letters*, 111(12):122503, 2013.

[42] M Agostini, AM Bakalyarov, M Balata, I Barabanov, L Baudis, C Bauer, E Bellotti, S Belogurov, A Bettini, L Bezrukov, et al. Improved limit on neutrinoless double-β decay of ge 76 from gerda phase ii. *Physical review letters*, 120(13):132503, 2018.

[43] Paolo Gorla et al. The cuore experiment: Status and prospects. In *Journal of Physics: Conference Series*, volume 375, page 042013. IOP Publishing, 2012.

[44] C Alduino, F Alessandria, K Alfonso, E Andreotti, C Arnaboldi, FT Avignone III, O Azzolini, M Balata, I Bandac, TI Banks, et al. First results from cuore: A search for lepton number violation via 0 ν β β decay of te 130. *Physical review letters*, 120(13):132501, 2018.

[45] A Gando, Y Gando, T Hachiya, A Hayashi, S Hayashida, H Ikeda, K Inoue, K Ishidoshiro, Y Karino, M Koga, et al. Search for majorana neutrinos near the inverted mass hierarchy region with kamland-zen. *Physical review letters*, 117(8):082503, 2016.

[46] Carlo Rubbia. The liquid argon time projection chamber: a new concept for neutrino detectors. Technical report, 1977.

[47] H Drumm, R Eichler, B Granz, J Heintze, G Heinzelmann, RD Heuer, J Von Krogh, P Lennert, T Nozaki, H Rieseberg, et al. Experience with the jet-chamber of the jade detector at petra. *Nuclear Instruments and Methods*, 176(1-2):333–344, 1980.

[48] E Conti, R DeVoe, G Gratta, T Koffas, S Waldman, J Wodin, D Akimov, G Bower, M Breidenbach, R Conley, et al. Correlated fluctuations between luminescence and ionization in liquid xenon. *Physical Review B*, 68(5):054201, 2003.

[49] Robert L Platzman. Subexcitation electrons. *Radiation Research*, 2(1):1–7, 1955.

[50] Eido Shibamura, Akira Hitachi, Tadayoshi Doke, Tan Takahashi, Shinzou Kubota, and Mitsuhiro Miyajima. Drift velocities of electrons, saturation characteristics of ionization and w-values for conversion electrons in liquid argon, liquid argon-gas mixtures and liquid xenon. *Nuclear Instruments and Methods*, 131(2):249–258, 1975.

[51] Ugo Fano. Ionization yield of radiations. ii. the fluctuations of the number of ions. *Physical Review*, 72(1):26, 1947.

[52] Tadayoshi Doke, Akira Hitachi, Shinzou Kubota, A Nakamoto, and Tan Takahashi. Estimation of fano factors in liquid argon, krypton, xenon and xenon-doped liquid argon. *Nuclear Instruments and Methods*, 134(2):353–357, 1976.

[53] Tadayoshi Doke. Fundamental properties of liquid argon, krypton and xenon as radiation detector media. *Port. Phys.*, 12:9, 1981.

[54] Tan Takahashi, S Konno, T Hamada, Mitsuhiro Miyajima, Shinzou Kubota, A Nakamoto, Akira Hitachi, Eido Shibamura, and Tadayoshi Doke. Average energy expended per ion pair in liquid xenon. *Physical Review A*, 12(5):1771, 1975.

[55] DS Leonard, P Grinberg, P Weber, E Baussan, Z Djurcic, G Keefer, A Piepke, A Pocar, J-L Vuilleumier, J-M Vuilleumier, et al. Systematic study of trace radioactive impurities in candidate construction materials for exo-200. *Nuclear Instruments and Methods in Physics*

Research Section A: Accelerators, Spectrometers, Detectors and Associated Equipment, 591(3):490–509, 2008.

[56]

[57]

[58] M Auger, DJ Auty, PS Barbeau, L Bartoszek, E Baussan, E Beauchamp, C Benitez-Medina, M Breidenbach, D Chauhan, B Cleveland, et al. The exo-200 detector, part i: detector design and construction. *Journal of Instrumentation*, 7(05):P05010, 2012.

[59] National Research Council et al. *The Waste Isolation Pilot Plant: A Potential Solution for the Disposal of Transuranic Waste*. National Academies Press, 1996.

[60] E Aprile, KL Giboni, P Majewski, K Ni, and M Yamashita. Observation of anticorrelation between scintillation and ionization for mev gamma rays in liquid xenon. *Physical Review B*, 76(1):014115, 2007.

[61] JB Albert, DJ Auty, PS Barbeau, D Beck, V Belov, C Benitez-Medina, M Breidenbach, T Brunner, A Burenkov, GF Cao, et al. Investigation of radioactivity-induced backgrounds in exo-200. *Physical Review C*, 92(1):015503, 2015.

[62] Andreas Hoecker, Peter Speckmayer, Joerg Stelzer, Jan Therhaag, Eckhard von Toerne, Helge Voss, M Backes, T Carli, O Cohen, A Christov, et al. Tmva-toolkit for multivariate data analysis. *arXiv preprint physics/0703039*, 2007.

[63] JB Albert, G Anton, I Badhrees, PS Barbeau, R Bayerlein, D Beck, V Belov, M Breidenbach, T Brunner, GF Cao, et al. Search for neutrinoless double-beta decay with the upgraded exo-200 detector. *Physical review letters*, 120(7):072701, 2018.

[64] CE Aalseth, N Abgrall, E Aguayo, SI Alvis, M Amman, IJ Arnquist, FT Avignone III, HO Back, AS Barabash, PS Barbeau, et al. Search for zero-neutrino double beta decay in 76ge with the majorana demonstrator. *arXiv preprint arXiv:1710.11608*, 2017.

[65] JB Albert, DJ Auty, PS Barbeau, D Beck, V Belov, M Breidenbach, T Brunner, A Burenkov, GF Cao, C Chambers, et al. Search for 2 ν β β decay of xe 136 to the 0 1+ excited state of ba 136 with the exo-200 liquid xenon detector. *Physical Review C*, 93(3):035501, 2016.

[66] DR Bes and O Civitarese. Matrix elements for the ground-state to ground-state 2 ν β- β-decay of te isotopes in a hybrid model. *Physical Review C*, 81(1):014315, 2010.

[67] Meng Wang, G Audi, FG Kondev, WJ Huang, S Naimi, and Xing Xu. The ame2016 atomic mass evaluation (ii). tables, graphs and references. *Chinese Physics C*, 41(3):030003, 2017.

[68] D Oo North. An analysis of the factors which determine signal/noise discrimination in pulsed-carrier systems. *Proceedings of the IEEE*, 51(7):1016–1027, 1963.

[69] O Bunemann, TE Cranshaw, and JA Harvey. Design of grid ionization chambers. *Canadian journal of research*, 27(5):191–206, 1949.

[70] Zhong He. Review of the shockley–ramo theorem and its application in semiconductor gamma-ray detectors. *Nuclear Instruments and Methods in Physics Research Section A: Accelerators, Spectrometers, Detectors and Associated Equipment*, 463(1-2):250–267, 2001.

[71] JB Albert, PS Barbeau, D Beck, V Belov, M Breidenbach, T Brunner, A Burenkov, GF Cao, WR Cen, C Chambers, et al. Measurement of the drift velocity and transverse diffusion of electrons in liquid xenon with the exo-200 detector. *Physical Review C*, 95(2):025502, 2017.

[72] M. Redshaw, E. Wingfield, J. McDaniel, and E. G. Myers. Mass and double-beta-decay Q value of Xe-136. *Phys. Rev. Lett.*, 98:053003, 2007.

[73] Reaching for the Horizon: The 2015 Long Range Plan for Nuclear Science. Technical report.

[74] DV Forero, M Tortola, and JWF Valle. Neutrino oscillations refitted. *Physical Review D*, 90(9):093006, 2014.

[75] Nuria López Vaquero, Tomás R Rodríguez, and J Luis Egido. Shape and pairing fluctuation effects on neutrinoless double beta decay nuclear matrix elements. *Physical review letters*, 111(14):142501, 2013.

[76] MT Mustonen and J Engel. Large-scale calculations of the double-β decay of 76 ge, 130 te, 136 xe, and 150 nd in the deformed self-consistent skyrme quasiparticle random-phase approximation. *Physical Review C*, 87(6):064302, 2013.

[77] G. Gratta. Summary and conclusions of the nEXO workshop Stanford/SLAC on 18-19 Nov 2012. nEXO memo, November 2012.

[78] D. Sinclair. Charge Collection for nEXO. EXO memo, October 2012.

[79] R Neilson, F LePort, A Pocar, KS Kumar, A Odian, CY Prescott, V Tenev, N Ackerman, D Akimov, M Auger, et al. Characterization of large area apds for the exo-200 detector. *Nuclear Instruments and Methods in Physics Research Section A: Accelerators, Spectrometers, Detectors and Associated Equipment*, 608(1):68–75, 2009.

[80] Elena Aprile, K Arisaka, F Arneodo, A Askin, L Baudis, A Behrens, E Brown, JMR Cardoso, B Choi, D Cline, et al. The xenon100 dark matter experiment. *Astroparticle Physics*, 35(9):573–590, 2012.

[81] Elena Aprile, J Aalbers, F Agostini, M Alfonsi, FD Amaro, M Anthony, B Antunes, F Arneodo, M Balata, P Barrow, et al. The xenon1t dark matter experiment. *The European Physical Journal C*, 77(12):881, 2017.

[82] DS Akerib, X Bai, S Bedikian, E Bernard, A Bernstein, A Bolozdynya, A Bradley, D Byram, SB Cahn, C Camp, et al. The large underground xenon (lux) experiment. *Nuclear*

Instruments and Methods in Physics Research Section A: Accelerators, Spectrometers, Detectors and Associated Equipment, 704:111–126, 2013.

[83] BJ Mount, RM Preece, MD Hoff, TK Edberg, P Rossiter, A Kaboth, S Pierson, VV Bugaev, P Bauer, A Currie, et al. Lux-zeplin (lz) technical design report. Technical report, 2017.

[84] Jaret Heise. The sanford underground research facility. *arXiv preprint arXiv:1710.11584*, 2017.

[85] D-M Mei and A Hime. Muon-induced background study for underground laboratories. *Physical Review D*, 73(5):053004, 2006.

[86] Yichen Li, Thomas Tsang, Craig Thorn, Xin Qian, Milind Diwan, Jyoti Joshi, Steve Kettell, William Morse, Triveni Rao, James Stewart, et al. Measurement of longitudinal electron diffusion in liquid argon. *Nuclear Instruments and Methods in Physics Research Section A: Accelerators, Spectrometers, Detectors and Associated Equipment*, 816:160–170, 2016.

[87] Sherena G Johnson. Refprop. 2013.

[88] DOKE Tadayoshi. Recent developments of liquid xenon detectors. *Nuclear instruments and methods*, 196:87–96, 1982.

[89] LS Miller, S Howe, and WE Spear. Charge transport in solid and liquid ar, kr, and xe. *Physical Review*, 166(3):871, 1968.

[90] Jonghee Yoo and WF Jaskierny. Electron drift in a large scale solid xenon. *Journal of Instrumentation*, 10(08):P08011, 2015.

[91] JL Pack, RE Voshall, AV Phelps, and LE Kline. Longitudinal electron diffusion coefficients in gases: Noble gases. *Journal of applied physics*, 71(11):5363–5371, 1992.

[92] JL Pack. Jl pack, re voshall, and av phelps, phys. rev. 127, 2084 (1962). *Phys. Rev.*, 127:2084, 1962.

[93] EM Gushchin, AA Kruglov, and IM Obodovskii. Electron dynamics in condensed argon and xenon. *Zh, Eksp. Teor. Fiz*, 82:1114–1125, 1982.

[94] Peter F. Sorensen. A position-sensitive liquid xenon time-projection chamber for direct detection of dark matter: The xenon10 experiment.

[95] E Aprile, M Alfonsi, K Arisaka, F Arneodo, C Balan, L Baudis, A Behrens, P Beltrame, K Bokeloh, E Brown, et al. Analysis of the xenon100 dark matter search data. *Astroparticle Physics*, 54:11–24, 2014.

[96] DS Akerib, HM Araujo, X Bai, AJ Bailey, J Balajthy, S Bedikian, E Bernard, A Bernstein, A Bolozdynya, A Bradley, et al. First results from the lux dark matter experiment at the sanford underground research facility. *Physical review letters*, 112(9):091303, 2014.

[97] K Yoshino. K. yoshino et al., phys. rev. a 14, 438 (1976). *Phys. Rev. A*, 14:438, 1976.

[98] Peter Sorensen. Anisotropic diffusion of electrons in liquid xenon with application to improving the sensitivity of direct dark matter searches. *Nuclear Instruments and Methods in Physics Research Section A: Accelerators, Spectrometers, Detectors and Associated Equipment*, 635(1):41–43, 2011.

[99] Robert Edward Robson. A thermodynamic treatment of anisotropic diffusion in an electric field. *Australian Journal of Physics*, 25(6):685–694, 1972.

[100] M Grech, R Nuter, A Mikaberidze, P Di Cintio, L Gremillet, E Lefebvre, U Saalmann, JM Rost, and S Skupin. Coulomb explosion of uniformly charged spheroids. *Physical Review E*, 84(5):056404, 2011.

[101] P Benetti, A Bettini, E Calligarich, F Casagrande, P Casoli, C Castagnoli, P Cennini, S Centro, S Cittolin, D Cline, et al. A simple and effective purifier for liquid xenon. *Nuclear Instruments and Methods in Physics Research Section A: Accelerators, Spectrometers, Detectors and Associated Equipment*, 329(1-2):361–364, 1993.

[102] E Aprile, R Mukherjee, and M Suzuki. Measurements of the lifetime of conduction electrons in liquid xenon. *Nuclear Instruments and Methods in Physics Research Section A: Accelerators, Spectrometers, Detectors and Associated Equipment*, 300(2):343–350, 1991.

[103] Aleksey Bolotnikov and Brian Ramsey. Purification techniques and purity and density measurements of high-pressure xe. *Nuclear Instruments and Methods in Physics Research Section A: Accelerators, Spectrometers, Detectors and Associated Equipment*, 383(2-3):619–623, 1996.

[104] G Mainfray and G Manus. Multiphoton ionization of atoms. *Reports on progress in physics*, 54(10):1333, 1991.

[105]

[106] Kendy Hall. In-situ laser tagging of barium ions in liquid xenon for the exo experiment.

[107] T Srinivasan-Rao, J Fischer, and T Tsang. Photoemission studies on metals using picosecond ultraviolet laser pulses. *Journal of applied physics*, 69(5):3291–3296, 1991.

[108] DT Palmer. A review of metallic photocathode-research. *SLAC Publications and Report No. SLAC-TN-05-080*, 2005.

[109] Huamu Xie, Ilan Ben-Zvi, Triveni Rao, Tianmu Xin, and Erdong Wang. Experimental measurements and theoretical model of the cryogenic performance of bialkali photocathode and characterization with monte carlo simulation. *Physical Review Accelerators and Beams*, 19(10):103401, 2016.

[110] R Bouwman and WMH Sachtler. Photoelectric determination of the work function of gold-platinum alloys. *Journal of Catalysis*, 19(2):127–139, 1970.